P-TYPE TRANSPARENT CONDUCTING OXIDES SYNTHESIZED BY ELECTROHYDRODYNAMIC PROCESS

BY

YIN LIU

A THESIS

SUBMITTED TO THE FACULTY OF

ALFRED UNIVERSITY

IN PARTIAL FULFILLMENT OF THE REQUIREMENTS
FOR THE DEGREE OF

DOCTOR OF PHILOSOPHY

IN

CERAMICS

ALFRED, NEW YORK

MAY, 2017

P-TYPE TRANSPARENT CONDUCTING OXIDES SYNTHESIZED BY

ELECTROHYDRODYNAMIC PROCESS

BY

YIN LIU

B.S. UNIVERSITY OF SCIENCE AND TECHNOLOGY BEIJING (2011)

SIGNATURE OF AUTHOR _____

APPROVED BY _____
YIQUAN WU, ADVISOR

_____
SCOTT T. MISTURE, ADVISORY COMMITTEE

_____
DOREEN D. EDWARDS, ADVISORY COMMITTEE

_____
STEVEN C. TIDROW, ADVISORY COMMITTEE

_____
CHAIR, ORAL THESIS DEFENSE

ACCEPTED BY _____
ALASTAIR CORMACK, DEAN
KAZUO INAMORI SCHOOL OF ENGINEERING

ACCEPTED BY _____
NANCY J. EVANGELISTA, ASSOCIATE PROVOST
FOR GRADUATE AND PROFESSIONAL PROGRAMS
ALFRED UNIVERSITY

[This blank page is necessary for submittal of your final copies. There should be nothing on it]

ACKNOWLEDGMENTS

I would like to express my thanks to my advisor, Dr. Yiquan Wu for his guidance and generous support through the course of my Ph.D. study at Alfred University. It is also him whose kindness, professionalism, and insightful knowledge influence me into who I am today. I feel very fortunate to have a close interaction and relationship with Dr. Yiquan Wu and his research group. I would also like to thank Dr. Scott Misture, Dr. Doreen Edwards, Dr. S.K. Sundaram for serving as my proposal and defense committee members. I would like to thank Dr. Nathan Mellott and Dr. Dawei Liu as well, for their kindness as being in my proposal committee.

I received countless, sincere and timely assistance during my stay at Alfred. I want to take this opportunity to acknowledge my colleagues, Yiyu Li, Yan Yang, Dr. Shi Chen, Dr. Bo Zhang, Dr. Wei Zhang, Dr. Yuxuan Gong, Dr. Tim Keenan, Michael Alberga, Daniel Steere, Gerald Wynick, James Thiebaud, Williams Francis and many other friends in the school of engineering.

This thesis concludes my journey at Alfred as a both a student and a researcher. Foremost, I want to express my supreme gratitude to Tonghan Wang and my parents for sacrificing all they have to support my study at United States. This thesis is dedicated to them.

TABLE OF CONTENTS

Page

LIST OF TABLES

Page

LIST OF FIGURES

Page

ABSTRACT

The aim of this work is to fabricate a p-type $CuAlO_2$ conducting oxide via electrospinning process and to develop a new photoluminescence (PL) functionality by introducing trivalent dopants, especially rare earth ions. The proposed trivalent doping method is also inspired by the current poor electrical enhancement of divalent doping and the reported simulation predicting the possible electrical enhancement by substitutional trivalent doping.

This work starts with preparing solution-based precursor, electrohydrodynamic processing and post calcination. Particularly, the increase of the polymer concentration in the solution will cause the transition from electrospray to electrospinning in the regime of electrohydrodynamic processing. The effect of deposition and treatment conditions on microstructure evolution and phase transformation was investigated for both $CuAlO_2$ thinfilms and fibers. Meanwhile, a mathematical model was constructed based on Newton's second law to model the jet behavior during electrospinning. The simulation result indicates that the stabilized jet could only travel for a relative short distance before whipping occurs, and the stabilized travel distance is dependent on solutions viscosity. The volume charge density in the jet also follows a logarithmic linear relationship with terminal fiber diameter, which further shows an equilibrium between surface tension and electrostatic force at the end of electrospinning process.

The photoluminescence property introduced by lanthanide species and the effect of trivalent dopant on electrical properties are investigated. An optical-oriented probing method is proposed to examine the effect of trivalent substitutions on Cu-O hybridizations, which is also essential for predicting electrical properties. The $CuAlO_2$ in the form of nanofibers also exhibits strong quantum size effect based on the energy shift from near-band-edge emission.

INTRODUCTION

$CuAlO_2$ is the first reported p-type conducting oxide (TCO)[1] and has attracted much attention in recent years due to the highly-demanded active p-n functional window in optoelectronic devices. The p-type TCOs appear almost 100 years later than n-type TCOs and by far it seems very difficult to use classic semiconductor rules to fabricate degenerate p-type TCOs by introducing extrinsic holes. Previous first principle study on $CuAlO_2$ electronic structure[2,3] has shed new light on trivalent ion substitution on Al site with increased DOS at VBM. To date, there have been only a few experimental reports on Cr trivalent doping[2,4] while inconsistency between electrical conductivity and band-gap is observed, mainly because the role of trivalent ion within the delafossite structure still remains unclear. Therefore, it would be necessary to perform systematic experimental study on trivalent ion doped $CuAlO_2$.

Another striking fact about $CuAlO_2$ research is that this p-type oxide could be applied in areas other than optoelectronics, such as water splitting,[5,6] thermoelectrics[7] and gas sensors.[8] Therefore $CuAlO_2$ has been regarded as a promising multifunctional building blocks for emerging technologies. This inspired us to introduce more functionalities during the course of trivalent doping, especially for the UV-IR light emission introduced by various trivalent RE^{3+} ions. As a transparent conducting oxide, $CuAlO_2$ is usually fabricated in the form of thin films or coatings. We herein propose the fabrication of $CuAlO_2$ non-woven nanofibers via a cost-effective electrohydrodynamic process. The nanofibrous coatings with high surface area and self-supported structure are being synthesized and their related optical and electrical properties will be compared with both bulk and nanoparticles.

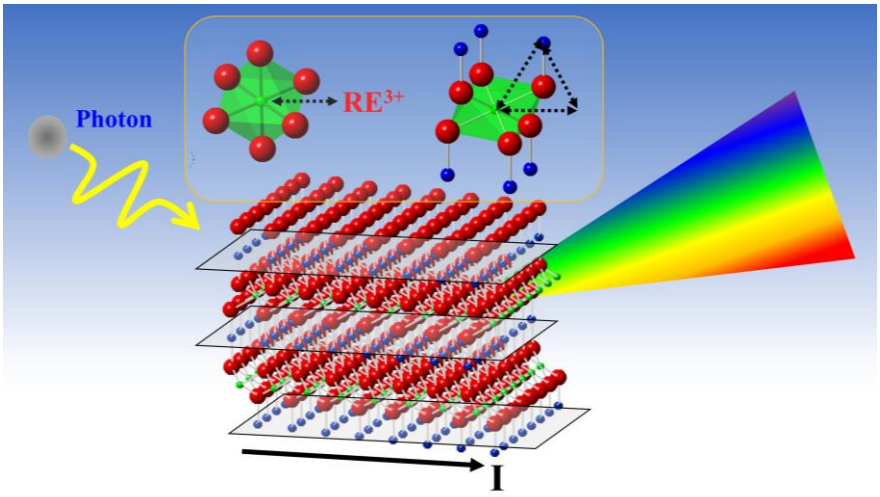

Figure 1. Cartoon drawing of delafossite structured $CuAlO_2$ used in photoluminescence applications, with AlO6 octahedra and [O-Cu-O]-[AlO_6] unit.

Figure 1 shows a cartoon drawing of delafossite structured $CuAlO_2$, in which O-Cu-O aligns vertically and edge-shared AlO6 octahedras spread out forming the basal layers. $CuAlO_2$ has long been regarded more as electrical materials but the lackluster of electrical performance has reduced the research enthusiasm in recent years. However, the unique crystal structure and its potential in optoelectronic applications give rise to new thoughts on optical characterization of $CuAlO_2$, which might open up a new door for optical engineering and optical-electrical correlative study in delafossite materials.

A. Background on p-type transparent conducting oxides (TCOs)

1. Delafossite and its anisotropic properties

Transparent conducting oxides (TCOs) comprise a class of materials that conductivity and optical transmittance could be achieved synergistically. In this regard, metallic materials that possess high conductivity cannot transmit visible light, while some highly transparent glass materials are insulators, since conductivity is strongly coupled to the lossy part of the refractive index.[9,10] TCOs, on the other hand, usually have an intermediate band-gap of over 3.1eV(corresponding to the energy of a 400 nm blue photon),[11] which provides a transmission window between wavelengths of about 0.4μm

and 1.5μm. At wavelengths shorter than 0.4 m, absorption occurs due to the fundamental band gap, and thus light cannot be transmitted. At longer wavelengths, reflection occurs because of the plasma edge, and light cannot be transmitted neither. These materials' conductivity ($>10^3\Omega^{-1}cm^{-1}$) can be enhanced by degenerate doping through native or substitutional dopants.[12] Due to these unique properties, TCO has been widely used as building blocks in architectural applications,[13] flat-panel displays including OLEDs, liquid crystal displays and plasma displays,[14] light emitting diodes,[15] biosensors,[16] and other emerging optoelectronic devices, in its form of coatings, thin films or wires. The first report on transparent conducting thin films of cadmium oxide (CdO) was published in 1907 by Badekar[17] who synthesized the films by thermal oxidation of sputtered films of cadmium. Since then, a lot of efforts have concentrated on materials selection, screening criteria and synthesizing techniques of TCOs, such as In_2O_3, ZnO, SnO_2, Ga_2O_3, [14,18-21] and ternary compounds derived from the binary oxides such as Zn_2SnO_4, $MgIn_2O_4$, $GaInO_3$, and $In_4Sn_3O_{12}$.[22-26] with room-temperature resistivity in the order of magnitude from 10^{-4}-10^{-2} Ω·cm, with carrier density in the order of ~10^{20} cm^{-3}. All of these materials exhibit unintentional n-type conductivity, with the carrier density and mobility comparable to those in conventional semiconductors. The conduction-band states are derived from the metal atoms, leading to electron-related properties that vary from compound to compound. The valence-band states, on the other hand, are derived mainly from the O 2p orbitals and are characterized by small dispersion, large effective masses, and high density of states.[27] Even though the TCOs have a vast range of applications as mentioned above, unfortunately there is no active device fabrication using TCOs as far as we know, mainly due to the monopolarity of the n-type TCOs.[28,29] Notwithstanding the lack of research in p-type TCOs compared to n-type ones, the p-type TCOs are essential for constructing the p-n functional window in which UV portion of the solar radiation could be absorbed by the electronics while visible light can be transmitted.[30] $CuAlO_2$ is the first reported p-type TCO without intentional doping by Kawazoe et al.[1] in 1997. It belongs to the delafossite $CuMO_2$ structure where M is a trivalent ion (Al, In, Cr, Y, Fe, Co, etc.). These oxides crystallize in the 3R rhombohedral (space group $R\bar{3}m$) or the isomorphic 2H hexagonal (space group P63/mmc) structures. The crystal structure shown in Figure 2 could be viewed as a stacking of Cu (d^{10} ions)

and MO_2 layers parallel to the ab plane. The Cu atom is linearly coordinated by two oxygen atoms along the c axis forming the O-Cu-O dumbbell structure, while M atom is octahedrally coordinated with six oxygen atoms. Each oxygen atom is coordinated tetrahedrally by one Cu and three M atoms. The linear arrayed d^{10} ions provide the semiconductivity[31,32] and are stabilized by a non-spherical electron configuration if the energy separation between s and d orbitals is sufficiently small.[33] In this regime, there is a prominent hybridization between s and d_z^2 orbitals (z direction is parallel to the c-axis in the lattice coordinate) which lead to the splitting of a filled nonbonding $(1/\sqrt{2})(s-d_z^2)$ and an empty antibonding $(1/\sqrt{2})(s+d_z^2)$ orbital. The bonding orbital has charges concentrated mainly in the basal plane, which significantly lowers the energy of the Cu ion in linear coordination, and gives rise to larger conductivity in the basal plane due to electron hopping between neighboring Cu ion orbitals. On the other hand, the antibonding orbital is used for mixing with neighboring O sp3 orbitals, making a bonding complex that lies deep below the Fermi energy and forms a valance band. This gives rise to the anisotropic electrical conductivity in delafossite materials.

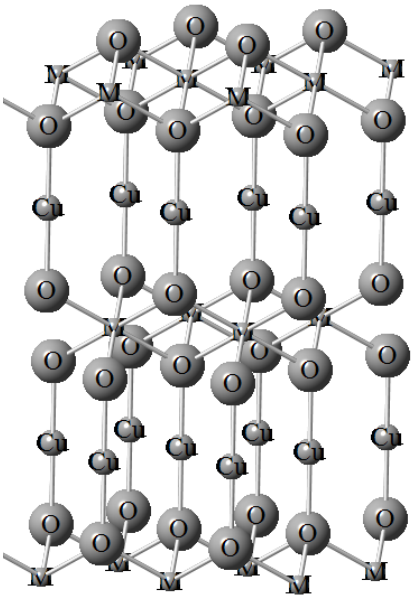

Figure 2. The $CuMO_2$ delafossite crystal structure.

As a p-type TCO, $CuAlO_2$ exhibits many merits such as high visible transmittance (~80%) due to its wide direct band gap of 3.5eV and good chemical stability for practical application. However its conductivity is only 3–4 orders of magnitude than the n-type TCOs.[34] The intrinsic conductivity could be explained by the following defect chemistry: $O_2(g) = 2O_O^x + V_{Cu}^- + V_{Al}^{3-} + 4h^+$, which stems from the nonstoichiometric defect reaction for a metal deficient oxide $CuAlO_x$. Therefore preparation conditions of these materials can be critical to enhance the conductivity. In addition, there have been many efforts to use dopants of various valence states to further improve the p-type conductivity. A common idea is to use divalent dopant such as Mg, Ca[35-37] to increase the hole concentration. Even though some great enhancements of 2-3 magnitude higher conductivity were reported, the traditional p-type doping approaches might not be suitable for $CuAlO_2$ and other delafossite-type semiconductors. The reason is that in wide-band-gap oxides the top of the valence band is predominately composed of O2p states and extrinsic holes introduced to the valence-band edge are trapped on oxygen atoms and cannot migrate.[2] Trivalent dopant in substitution of the Al site, has become a new experimental interest in recent years. Based on some calculation results,[2] the substitution doping is predicted to increase the density of states at the top of the valence band. Additionally, the change of M-O covalency could lead to a decrease of O valance charge in the Cu-O-Al unit, which finally mediates the Cu d states and an improved conductivity would be expected.

2. Optical properties of $CuAlO_2$

Despite numerous research and initiatives on enhancing electrical conductivity in $CuAlO_2$ and other delaffosites, the conflicts in reported and calculated band-gaps, optical-electrical correlation and mystery in doping mechanisms puzzled researchers from utilizing this class of material to a broader range of applications, such as transparent conducting oxides (TCOs) applications, luminescent materials, catalysts, batteries, ferroelectrics and so on[36,38-42]. In this regards, the optical properties, mainly the photoluminescence property of $CuAlO_2$ have scarcely been investigated. Recent efforts on low-temperature and room temperature photoluminescence measurements[43,44] have

unraveled the intrinsic luminescence properties of $CuAlO_2$ and pointed out the plausible Cu-Cu interaction or near-band-edge transitions to a higher energy level. Additionally, first-principle calculation results from Scanlon et al. [2,45,46] recently showed that the 3d states of trivalent Al site and the involvement of trivalent ions in the formation of valence band is important for the delocalisation of the hole states of $CuAlO_2$. The octahedral unit containing the covalent M-O bonding and its local relaxation effects on the O-Cu-O dumbbell structure synergically influence the electrical and optical properties. Therefore, revisiting and tuning the optical properties may not only develop new functionalities of p-type delaffosites, but also enhance the electrical performance.

The photoluminescence of CMO_2 delafossite was firstly observed by Jacob et al.[47] A two-band transition mechanism was proposed as shown Figure 3. Cu^+ luminescence was originally observed in Cu^+ doped alkali or alkali-earth halides[48,49], where copper pairs or isolated copper ions give off green and blue emissions[50]. In the CMO_2 delafossites with a typical linear coordination of monovalent copper ions, although the Cu-O distance is short and confined at a single site, two fluorescence bands were observed. Band I is room-temperature activated and band II transition is only permitted at low temperatures. The origin of the two bands stems from the hybridization of Cu 3d-4s, in which the 3d level was split up into two sub-bands. The degree of the hybridization is dependent of trivalent cations even though the confined Cu-O bound can be hardly affected by the size and nature of M^{3+} cation. In the comparative case of $CuYO_2$ and $CuLaO_2$, the La-O bond is less covalent than the Y-O bond, the antagonist Cu-O bond is expected to be more covalent in $CuLaO_2$. The antibonding $3d_z^2$+4s states thus lift towards z-direction, causing a change in transition energy in the two fluoresce bands. Another empirical analysis postulates that the Stokes shift (energy difference between emission and excitation) decreases with the size of the M element for both band I and II.

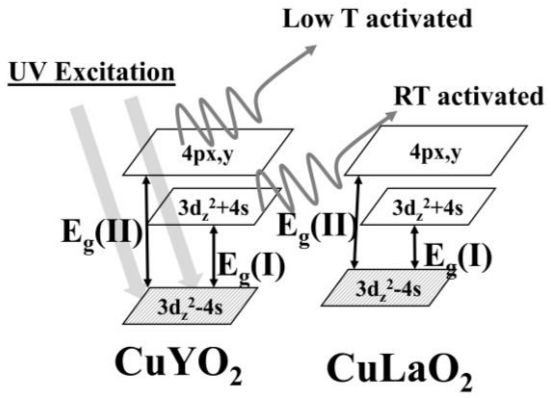

Figure 3 Energy transition in delafossite-type CuYO2 and CuLaO2 at low temperature (10K) and room temperature. (Reprint from Jacob[47])

The early work on luminescence properties of different types of delafossite materials sheds light on investigating the role of trivalent ion in fluoresce shift. Since then there have been only a few reports on the luminescence properties of $CuAlO_2$, or other delafossites. The reported room-temperature photoluminescence has a large variation in emission wavelength, ranging from 300 to 500nm. The origin of the room-temperature luminescence is also puzzled. Besides the energy transition bands resulting from the 3d-4p hybridization, the emission is sometimes ascribed to copper vacancies and interstitial oxygen[51,52]. On the other hand, processing methods and the presence of secondary phase could strongly influence the PL emissions. A broad peak emission between 353 and 366nm was recently identified by Byrne et al.[44] at room temperature. At the low temperature (14.5K), as shown in Figure 4, the PL spectra consist of several emission bands. The 355 nm band (corresponding to 3.49eV bandgap) results from the direct bandgap transition, which is in good agreement with room temperature PL spectra. The blue emission of 430nm at low temperature, however, is metal stable with temperature and may indicate possible Cu-Cu interactions and other unknown photochemistry mechanism.

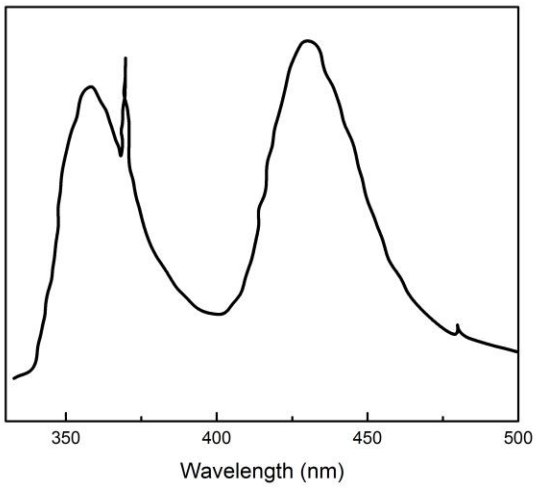

Figure 4. High resolution PL spectra of $CuAlO_2$ at 14.5K, under 325nm illumination. (Reprint from Byrne[44])

In comparing the early work from Jacob with the Byrne's most recent work, both the UV and blue emissions are closely related to trivalent ions in the delafossites. In addition, the electron-phonon comping is independent of temperature. Typically, at low temperatures phonon contribution to peak broadening as well as the kinetic energy of the free particle reduces. However, at both room and low temperatures, the FWHM of the UV emission was ~34nm. The relation between trivalent cation and luminescence properties need further assessments and elaborations.

3. Constructing a multifunctional nanomaterial

Originally as an attempt to study the trivalent doping mechanisms the in p-type $CuAlO_2$ transparent conducting oxide as well as to enhance its conductivity, the introduction of trivalent ions, particularly REs, could also bring in new photoluminescence functionality, yet their electrical properties are waiting to be examined. Nowadays the synthesis of multifunctional nanomaterials is a ubiquitous theme in nanoscience aimed at integrating multiple functionalities into individual building blocks to enable the fabrication of novel devices. This proposed electrohydrodynamic process and functionality (Figure 5) are also considered to be

beneficial to some current applications. The fibrous form could be integrated in many devices such as solar cells, transistors and catalyst due to their low dimensionality and large surface area. Through the up- and down-conversion of the IR and UV light, the p-type TCOs could convert the non-visible light into visible region, which could be secondarily utilized or collected by other devices. For example, in the conventionally used low-e architectural coatings, this TCOs will enable more colors for different applications. The up-conversion nanofibers converting UV light into visible light would expect to improve the solar radiation harvesting in some coupled water-splitting photoelectrodes such as hematite.

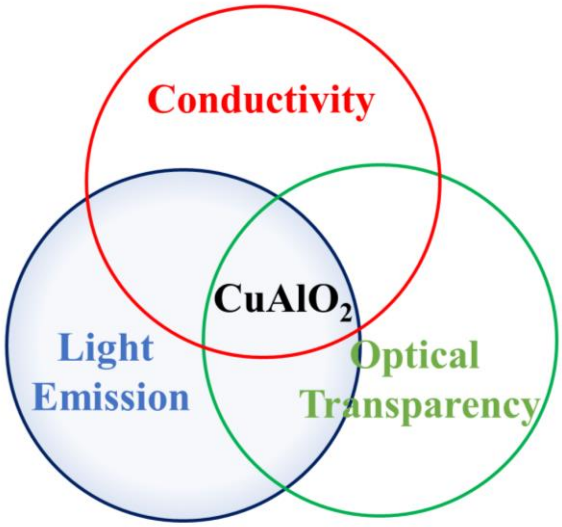

Figure 5. Proposed $CuAlO_2$ nanostructured materials integrating three important functionalities.

B. Electrohydrodynamic fabrication of novel ceramics

1. Basic instrumentation

The electrohydrodynamic phenomenon, which describes the interaction between liquid and electrical field, has been discovered for over one hundred years. However, the incorporation of this phenomenon into practical material processing approaches has just become available in recent decades[53-56]. The basic concept lies in the fact that the liquid

meniscus escaping the capillary tip under electrical field would deform into a conical shape (Taylor core), from where the submicrometric liquid jet is formed. The jet could either go through physical disruption after propulsion to form mono-charged nanodroplets, or maintain its single wire shape, mainly depending on the viscoelasticity and dielectric properties. The former is called electrospray while the latter is electrospinning. These two techniques have been widely utilized in synthesizing a large variety of materials ranging from polymers, ceramics and metals to composites[57-60], with the forms of thin films, nanofibers, and nanobelts. The electrohydrodynamic derived technique could also rival other nano-scale fabrication techniques due to its simple setup and versatile capabilities in tailoring the nanostructure and properties. On the other hand, since there has been growing research interest in nano building blocks for some emerging technologies such as photo catalyst, thermoelectrics, batteries and nanophosphors, this recalls the demand to employ electrohydrodynamic processing to fabricate classic and new materials in both low dimensions and various morphologies. Even though the electrohydrodynamic processing was originally designed for polymeric products, it is also capable of fabricating ceramics from either chemical solutions or suspensions. Table I lists some low dimensional oxide materials fabricated by electrohydrodynamic processing from previous reports. The main idea of fabricating the n- and p- type oxides through electrohydrodynamic processing is to firstly prepare and deposit the precursor solutions containing the desired ion species on substrates, and then calcine the precursors to initiate crystallization. Besides the merits of simple setup and cost-efficiency, the electrohydrodynamic processing involves fewer preparation steps and exhibits a good repeatability and potential in large-scale production, which is favorable for thin film technology and other emerging optoelectronic devices.

Table I Recent Advances in Oxide Materials Synthesized by Electrohydrodynamic Processing.

Materials	Morphology	Applications	Ref.
AZO/ITO	Thin film	TCO	61
TiO_2	core-shell spheres	DSSC	62
TiO_2	nanofibers	Photocatalyst/Batteries	63
TiO_2/SnO_2	nanofibers	Photocatalyst	64
TiO_2/ZnO	nanofibers	Photocatalyst	65
NiO-CdO	nanofibers	Sensors	66
YSZ	thin film	SOFCs	67
YSZ	nanofibers	-	68
SnO_2	thin film	Gas sensor	69
ZnO	thin film	TCO	70
CdO	nanofibers	TCO	71
CeO_2	nanofibers	Capacitors, catalyst	72
Al_2O_3	nanofibers	-	73
Ga_2O_3	nanofibers	TCO	19
$LiCoO_2$	wires	Cathode	74
MgO	nanofibers	Luminescence	75

The basic set up for electrohydrodynamic processing is shown in Fig. 1.4. The aforementioned two approaches, namely, electrospray and electrospinning, generate droplets and fibers respectively. For example, electrospinning is a typical electrohydrodynamic process in which viscous liquid droplet is fed into an electrical field ($\sim 2\times10^5 V\cdot m^{-1}$) by a pumped syringe. Under the driving force of the electrical field, the

droplet at the needle tip will overcome the liquid surface tension and become conical shape, also known as the Taylor Cone[54]. In the electrospinning process, since the viscosity of the liquid precursor is tuned by high molecular weight organic agent to yield high viscoelasticity, a single and continuous fiber[55,76] with dimensions that range from micrometers to nanometers will be propelled from the Taylor Cone and electrospun to a grounded collector. Practically, we use a home-built electrohydrodynamic setup to perform the fiber and thinfilms synthesizing as shown in Figure 6. The precursor is fed at a rate of 0.1mL/hr. The needle of the syringe is connected to an 18kV voltage generator, while the stainless steel collector is grounded. A non-woven polymeric fiber mat is formed and later exfoliated for further heat treatment to burn out the organics and initiate crystallization of ceramic fibers.

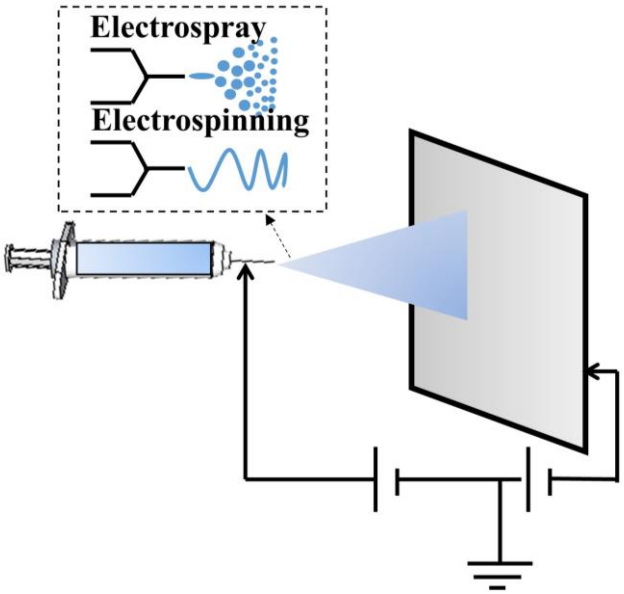

Figure 6. A general setup of electrohydrodynamic processing with droplets or a single fiber exiting the capillary under the forward bias electrical field.

2. Electrohydrodynamic processing on tuning the microstructures

Electrohydrodynamic processing is versatile in fabricating polymeric objects with different microstructures. Figure 7 summarizes several typical microstructures. Within the regime of electrohydrodynamic processing (EHD), the switchover point between

electrospray and electrospinning depends on the viscosity of the solvent. During the EHD process, the interaction of surface tension of the solvent and electrostatic force generated within the solvent leads to the cone-jet mode. Depending on the viscosity, conductivity and permittivity of the solvent, different theories and scaling laws have been developed to describe the jet formation during EHD processing.

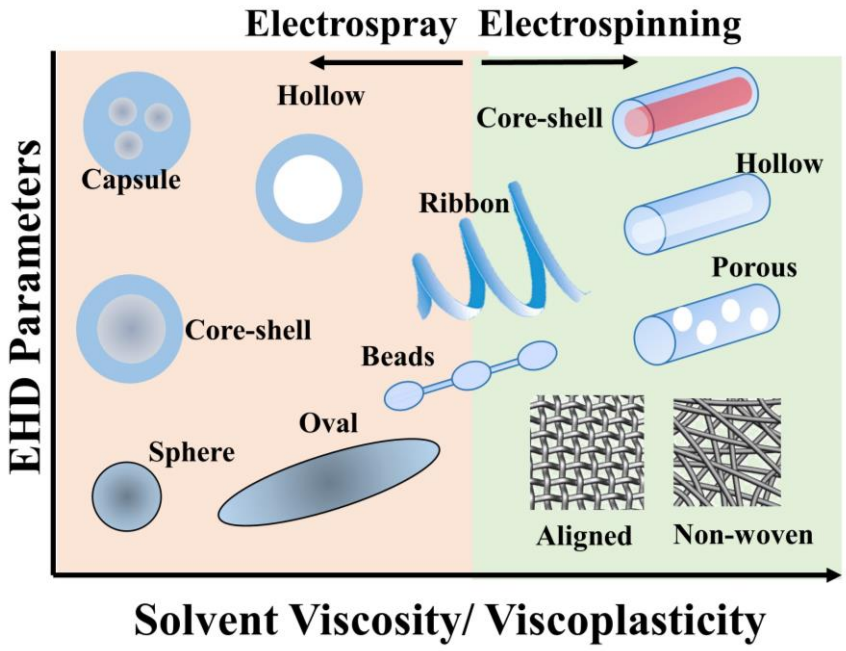

Figure 7. Schematic diagram showing various microstructures produced by electrohydrodynamic (EHD) processing. EHD parameters may include voltage, nozzle setup, collector, etc.

For electrospray, where the droplet of the liquid is formed at the apex of the nozzle, the size of the droplet could be estimated from a theoretical model of the charge transport. In this regard, the scaling law of mean droplet size d could be expressed as a function of electrical conductivity of the liquid fluid, K, and the flow rate Q[77].

$$d = G(\varepsilon)(\varepsilon\varepsilon_0 Q / K)^{1/3} \quad (1)$$

where $G(\varepsilon)$ is a dimensionless function of the liquid dielectric constant ε. This equation is valid for liquid with high conductivity (K>1E-5 S/m) and low viscosity larger than 0.1-1[78,79]. Hartman et al.[80] proposed a universal scaling law of droplet size and

testified with experimental observation, in which the droplet size d follows different exponential relation with conductivity K.

$$d = (\frac{\rho\varepsilon_0 Q^3}{\gamma K})^{1/6} \quad (2)$$

where ρ is the density, γ is the surface tension. Modelling of electrospinning process, on the other hand, has always been challenging. One major reason is solving the instability at the initial stage of electrospinning, where the jet undergoes whipping and thinning. Hohman[81,82] and Feng et al.[83] proposed different solutions for modelling Newtonian flow during electrospinning jetting. Fridrikh et al.[84] presented a simple model for stretching of a viscous charged fluid in an electric field. The model is based on total charge conservation between the nozzle and the collector. The terminal jet radius r is described as follow:

$$r = \left\{ \gamma\varepsilon \frac{Q^2}{I^2} \frac{2}{\pi[2\ln(\mathrm{R}/\mathrm{h}) - 3]} \right\}^{1/3} \quad (3)$$

The fiber dimension at the terminal is a function of surface tension γ, dielectric constant ε, flow rate Q, electric current I, radius of whipping curvature R, and radius of the initial jet. The ratio of Q to I denotes the volume charge density. One interesting fact is that the Q/I value sees an exponential decay with the increase of flow rate, eventually collapses to a value of 2/3.This is because of the termination of jet thinning away from the nozzle apex: when the jet streaming reaches the saturation of the whipping instability, the fiber dimension ceases and the surface charge repulsion equals to the surface tension.

Besides tuning the liquid physical properties to acquire either droplets, oval, ribbons or fibers, the sub-microstructural morphology could be also modified by changing the EHD parameters. The core-shell[85] and hollow[86] structures could be obtained by using a co-axial electrohydrodynamic set up, where the inner and outer nozzles are fed with different precursors. The aligned fibrous structure or other patterned microstructure require the modification of the electric field distribution between the two electrodes.

3. One-dimensional phosphors derived from electrospinning

Photoluminescence functionality has been used in a vast of areas and recent research has focused on nanostructured materials. The luminescence properties from a nanostructured material are not only suitable for some emerging technologies, but also crucial to help researchers better understand the nanostructure and other dimensionality-induced properties. In fact, size and shape of the phosphors have an important influence on the emission intensity and the efficiency of the device. One-dimensional (1D) structures, such as fibers, tubes, wires, rods and belts, have attracted great research interests because of their potential to test fundamental quantum mechanical concepts and the vital role in various applications such as photonics,[87] nanoelectronics,[88] and data storage.[89] Some repots already show a great improvement of quantum efficiency in rare earth (RE) doped inorganic nanowires comparing to bulk materials.[90] Processing 1D phosphors via conventional hydrothermal synthesis usually lacks controllability. In contrast, electrospinning could be a cost-effective and effective approach in fabricating 1D materials. It is easy to control the morphology and fiber dimension through adjusting the electrospinning parameters. In addition, since most electrospinning process is combined with a sol-gel process, basically there is no thermodynamic different between synthesizing nanofibers through electrospinning process and synthesizing particles through a sol-gel or combustion process.

The rare earth (RE) elements often refer to the lanthanide (Ln) series plus yttrium and scandium. Ln^{3+} ions are the most frequently used activator ions in luminescent materials, including inorganic/inorganic, inorganic/polymer and complex/polymer materials. They usually exhibit a strong fluorescent emission via intra-4f or 4f–5d transitions. To date, there have been many 1D inorganic materials doped with RE ions synthesized from electrospinning,[90-93] including some n-type TCOs. However, regarding to $CuAlO_2$, there is almost no report on its luminescence properties in the form of nanofibers. To date, we are probably one of the earliest groups who fabricated CuAlO2 thinfilms and nanofibers via electrohydrodynamic processing [See reference [94,95]].

ELECTROHYDRODYNAMIC PROCESSING OF $CuAlO_2$

A. Introduction

Due to the unique optoelectronic properties of p-type $CuAlO_2$ and related interesting physical properties, various methods have been employed to fabricate $CuAlO_2$, such as solid-state method[96,97], sol-gel method[98], hydrothermal[42,99], DC-sputtering[34,100], pulsed laser deposition (PLD)[101], atomic layer deposition (ALD)[102], etc. Thin-films, nanopowders and bulk $CuAlO_2$ have been successfully synthesized through the above approaches. As mentioned in the introductory chapter, the optical bandgap, optical and electrical properties can significantly vary with synthesis methods. The synthesis atmosphere and phase configuration are usually reckoned as the main causes for the reported variations. Synthesis in air or oxygen reduced environment could change the copper and oxygen vacancies, or copper on aluminum antisites, which results in a change in transition energies between VBM and CBM[45]. Phase configuration is another commonly discussed issue from literatures. Since the phase transformation towards $CuAlO_2$ involves a meta-stable phase formation of spinel $CuAl_2O_4$, and possibly unreacted alumina, it is critical to obtain phase-pure delafossite $CuAlO_2$. In this regard, many literatures have discussed the Al/Cu ratio[103], precursors[104] and annealing effects[105,106].

Commonly used techniques to fabricate the $CuAlO_2$ compound often involve high temperature solid-state reaction, reduced atmosphere or repeated heat treatment. Based on the thermodynamic rule, the $CuAlO_2$ is metastable below 1000ºC in ambient atmosphere whereas a stable spinel $CuAl_2O_4$ could be formed at the temperature range of 625 to 1000ºC. Practical techniques often reduce the oxygen partial pressure to reduce the reaction temperature, yet still requires long processing time to form stable delafossite phase. Wet-chemistry methods such as sol-gel and hydrothermal could significantly reduce the synthesis temperature. Up to now, there is only one report by Zhao et al.[107] on fabricating $CuAlO_2$ nanofibers via electrospinning at 1100°C. However, the detailed

microstructure evolution and electrohydrodynamic process parameters are not found in any articles. In this study, the aim is to investigate the electrohydrodynamic and annealing effects on $CuAlO_2$ thin-film or nanofibers, which serves as a unified synthesis method for further characterization in order to rule out possible disturbance from fabrication variations.

B. Experimental

1. Acrylamide gelling route

The copper source was from copper (II) nitrate trihydrate (99-104%, Sigma-Aldrich) and aluminum source from aluminum nitrate nonahydrate (98.0-102.0%, Sigma-Aldrich). The acrylamide route consists of two steps. The first step is to solve all the salt nitrates in their stoichiometric ratio, namely Cu:Al=1 (0.01mol for each). The solvent used is 100 ml mixture of 1:1 ethylene glycol/ethanol (0.5M solution). The solution was stirred and the temperature was raised to 70°C. The second step is the gelation process, in which polymeric network is formed to chelate the cation species in the solution. The water-soluble monomers 0.5g acrylamide (ACS reagent grade, Sigma-Aldrich) and 0.2g N,N'-methylene-bis-acrylamide (ACS reagent grade, Sigma-Aldrich) were used. Then, 50mg ammonium persulfate was added to initiate the polymerization. The gel was later used for electrospray experiment.

2. Sol-gel route

Considering the toxicity of acrylamide, an alternative sol-gel route was adopted. In this method, 0.01mol $Cu(NO_3)_2 \cdot 3H_2O$ (Sigma-Aldrich, puriss. p.a.) and $Al(NO_3)_3 \cdot 9H_2O$ (Sigma-Aldrich, ACS reagent) were dissolved in 30mL ethanol. After that 0.04mol citric acid (Sigma-Aldirch, ACS reagent) was dissolved in 20mL ethanol solvent and then this solution was added into the nitrate solution. In the nitrate-citrate system, the nitrate serves as the oxidant reagent, while the carbonyl group serves as reducing agent to reduce Cu(II) to Cu(I). Then the whole mixed solution was stirred at 70ºC for 1hr to facilitate the jellification. Most of the electrospinning experiments in the present study used the sol-gel route. However, since the viscoplasticity of the as-prepared solution is not sufficient for electrospinning, polymeric agent Polyvinylpyrrolidone (PVP) (Sigma-Aldrich, average

mol. wt. 40,000) was further added to the gel to tune the viscosity. For the following chapters on trivalent ion doped $CuAlO_2$, the nitrate salt of rare earth elements and other cations (ACS reagent grade, Sigma Aldrich) were added into the original solution. Due to the small amount of dopant involved in this study, the dopant effect on EHD behavior and thermal treatment will not be discussed here.

3. Electrohydrodynamic setup

A high power DC supply (ES-series, 5-100kV, Gamma High Voltage Research, Ormond, FL) was used to generate the electric field between two electrodes (nozzle and collector). The syringe used was from NORM-JECT (5ml, Henke Sass Wolf) and the dimension of the nozzle apex was 0.5mm. The feed process of the syringe was controlled by an automatic pump (Single-syringe infusion pump, Cole-Parmer, Vernon Hills, IL). 10x10mm Quartz substrate (MTI, Richmond, CA) was used as the substrate for electrospray and electrospinning. Otherwise the as-spun fiber mat was directly peeled off the collector for successive calcination. Figure 8 presents the actual EHD setup in the lab. During the whole course of this study, the voltage of the power supply varied between 10kV and 20kV, while the working distance was maintained at ~15cm, generating equivalent electric field of 667V/cm to 133V/cm. The flow rate of the automatic syringe pump was tuned from 0.1mL/h to 1mL/h. Jet currents were determined by measuring the voltage drop across a 10kΩ resistor. The resistor was connected to the collector, with another end connected to the ground. When the electrified jet reached the current continuously, the voltage on the resistor was measured by a portable multimeter (Sinometer DT9205B). Then the jet currents could be calculated using Ohm's law.

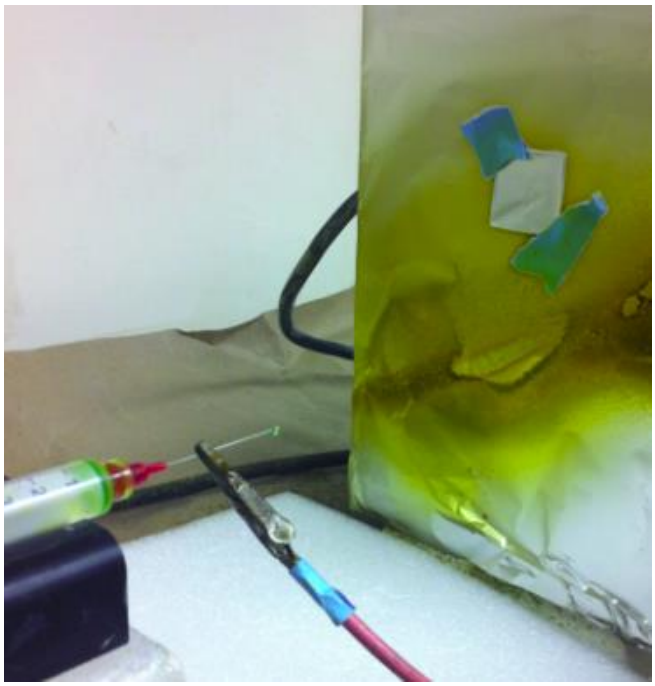

Figure 8. Digital image of the electrohydrodynamic processing setup. A plastic syringe loaded with precursors is connected to the power supply. Stainless steel plate is used as the collector and connected to the ground. The quartz substrate is fixed by the tape on the collector.

4. Calcination and anneling equipments.

After the EHD process, the polymeric thinfilms or fibers require further heat treatment. Several types of the furnaces were used. For heat treatment in air, a muffle furnace (RWF-1100, Carbolite, UK) is used. The heat treatment in flowing argon was conducted in a tube furnace (MTI, Richmond, CA). In addition to the EHD processing, spark plasma sintering technique (FCT Systeme GmbH) was employed in an attempt to study the reaction between Al_2O_3, CuO and Cu_2O during the formation of $CuAlO_2$.

5. Materials Charaterizations

The morphology and elemental analysis was performed on an FEI Quanta 200F ESEM (Hillsboro, OR) equipped with EDAX. During the study of EHD process, polymer solution viscosity was measured by Discovery HR-2 rheometer (TA instruments, New Castle, DE). The thermal history of precursor decomposition and reaction was recorded by TG/DTA (TA instruments, New Castle, DE) in flowing air and nitrogen separately. After the calcination and crystallization, the surface area of the fibers (BET, BJH) was

analyzed by Tristar II system (Micromeritics, Norcross, GA). Phase identification was detected by the Bruker D2 Phaser (Bruker-AXS, Madison, WI). The TOPAS (Bruker-AXS, Madison, WI) software package was employed to extract the lattice parameter constants from the experimental XRD patterns. The steady-state photoluminescence spectrum measurements were performed on a Spex FluoroLog Tau-3 (HORIBA Jobin Yvon Inc., Edison, NJ) at 300 K. The UV excitation source used is a Xeon lamp and 980nm laser was used for IR excitation. A Fourier-transform Raman spectrometer (Thermo Nicolet 6700) was used to record room-temperature Raman spectra of the delafossite samples.

For electrical properties, the room temperature sheet resistivity was measured by a four-probe set up (Bridge Technology, Chandler Heights AZ). The temperature-dependent resistivity was measured in a dental furnace (Cerampres Qex; Ney Dental Inc, Bloomfield, CT). The multimeters used in this study were Keithley 2000 and Keithley 6400 picoammeter (Keithley Instruments Inc., Cleveland, OH). The data was acquired by a National Instruments LabVIEW program. For the measure of sheet resistivity, the films deposited on quartz substrate were measured. For the temperature-variant DC measurement, a two-electrode setup was used. The ceramic fibrous mat was compacted into a pellet for all the electrical measurements.

The chemical composition as well as local chemical environment was analyzed with a PHI Quantera Scanning X-ray photoelectron Microprobe (XPS). The XPS data sets were collected with Al Kα X-rays (monochromatic, beam size=100 μm) at an output power of 25.5 watts, with a photon energy of 1486.6 eV and a step size of ~0.025 eV. Survey scans were performed with a pass energy of 140 eV to gain qualitative information such as peak identification and peak position. Peaks identified in all survey scans were used to adjust high resolution scan binding energy range, pass energy (26 eV) and beam dwelling time (~ 100ms). The beam sweeps for each high resolution scan was adjusted (3 sweeps:Al_{2p}/Cu_{2p}, 1 sweep: O_{1s}/C_{1s}) to yield a signal-to-noise ratio of >100:1 with exception of doping agents Eu_{4d} (3 sweeps), which were adjusted to yield a signal-to-noise ratio of >50:1. Upon acquisition analysis chamber vacuum was maintain below $1.3x10^{-9}$ torr. The analyzed area was ~1-2 mm in diameter. Standard deviation in terms of

peak position and full-width-half-maximum (FWHM) was measured by probing 3 different spots on an identical sample.

C. Electrospray synthesis of $CuAlO_2$ thin films by acrylamide gelling route

The bluish gel-like solution was loaded into the syringe. The voltage applied on the nozzle set as 5 and 10kV, respectively. Since the droplet will accumulate on the substrate forming liquid stream, the collector was heated to ~135°C in order to evaporate the droplet during electrospray. The droplets of micrometer size were projected towards the substrate under the electric field. The spray time was set as 2hr. Figure 10 shows the morphology of the as-spray film. A polymeric feature could be discerned, due to the formation of organic gel network of acrylamide formation. The electrospray processing could be viewed as droplet deposition and overlapping onto the substrate. Since the droplet is positively charged whereas collector is grounded, the electrostatic force will attach the droplet firmly on the substrate. The effect of electrospray parameters on film morphology was investigated. Figure 9 includes the SEM images of as-spray films under different EHD conditions. The controlled parameters in this study are flow rate, voltage and spray time. The work distance was kept at 15cm. Figure 9 (a)-(c) show poor coverage of the gel on the substrate. The coverage increases with the increase of flow rate and spray time. In addition, at low voltage, the droplet size (b) is slightly larger than that at high voltage (c), which is obvious because the larger electrostatic repulsive force will decrease the droplet dimension during travelling to the collector. A fully-covered film was obtained by using parameters in Figure 9 (d).

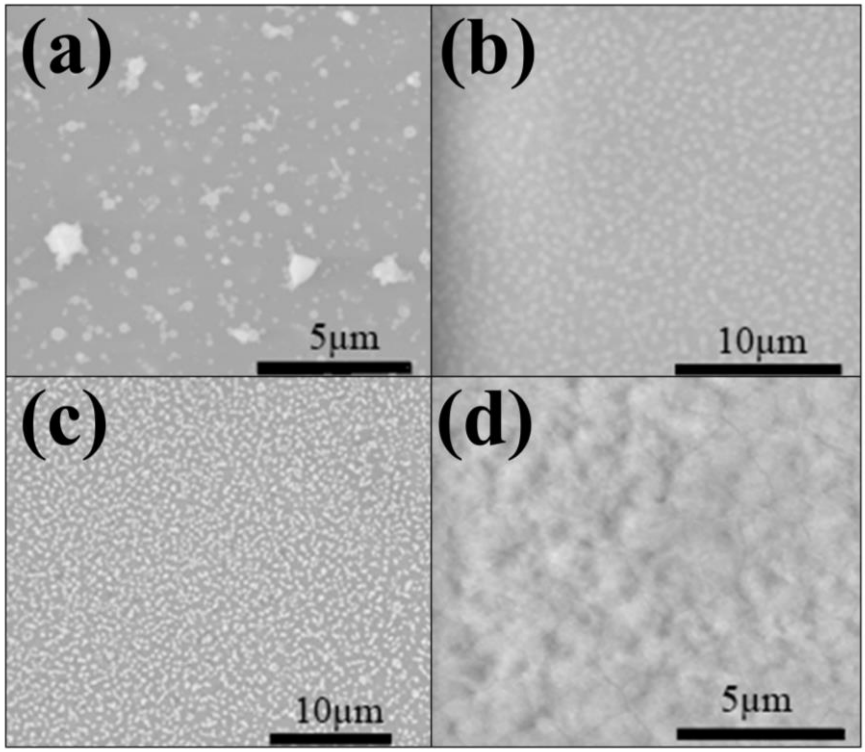

Figure 9. SEM micrographs of as-spray polymeric film using different electrospray parameters: (a) 0.1 mL/h flow rate, 5kV voltage, 5min spray time; (b) 0.5 mL/h flow rate, 5kV voltage, 10min spray time; (c) 0.5 mL/h flow rate, 10kV voltage, 15min spray time; (d) 0.5 mL/h, 10kV, 30min.

Since the polymeric film will undergo heat treatment, the polymeric reagents will be burned off resulting in a large shrinkage and film thinning. Therefore the spray time was expanded to 2h. The microstructure is shown in Figure 10(a). The tilted view in Figure 10(b) reveals some roughness on the as-spray film, which indicates the merge and overlap of the droplet.

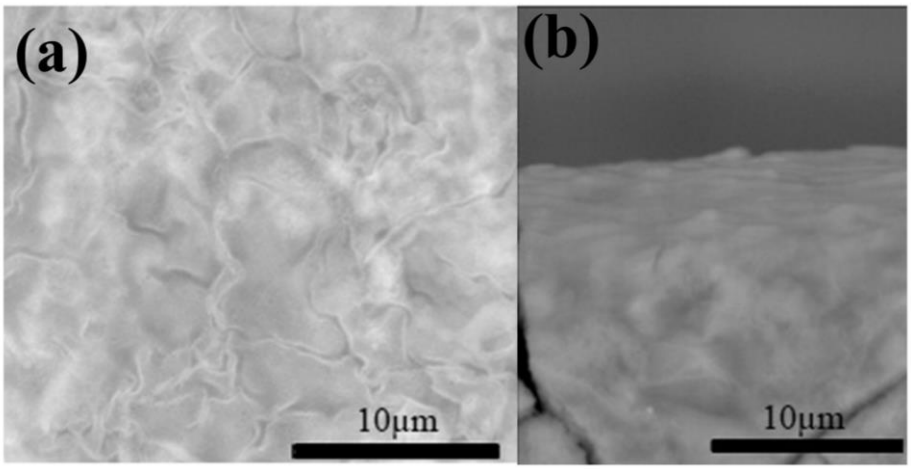

Figure 10. SEM micrographs of as-spray polymeric film: (a) top view; (b) 70° tilted view.

The as-spray thin film exhibited amorphous feature, as shown in Figure 11. The precursor without gelling reagents (acrylamide, etc.) was prepared for comparison. When the thin film was calcined in air at 500°C in air, only CuO occurred due to a simple oxidation process. The first calcination at 500°C in air is usually necessary according to previous reports on delafossites synthesis, in order to burn out the organics and initiate decomposition of copper nitrate. Moreover, the final formation of $CuAlO_2$, may require the precursor of CuO to provide extra oxygen. The second-step calcination was performed in flowing argon at higher temperatures. The delafossite structure could be formed at only 800°C, without other phases presented. In contrast, the one without acrylamide gelling calcined at even higher temperature of 1000°C only exhibited a single weak diffraction peak at ~36°.

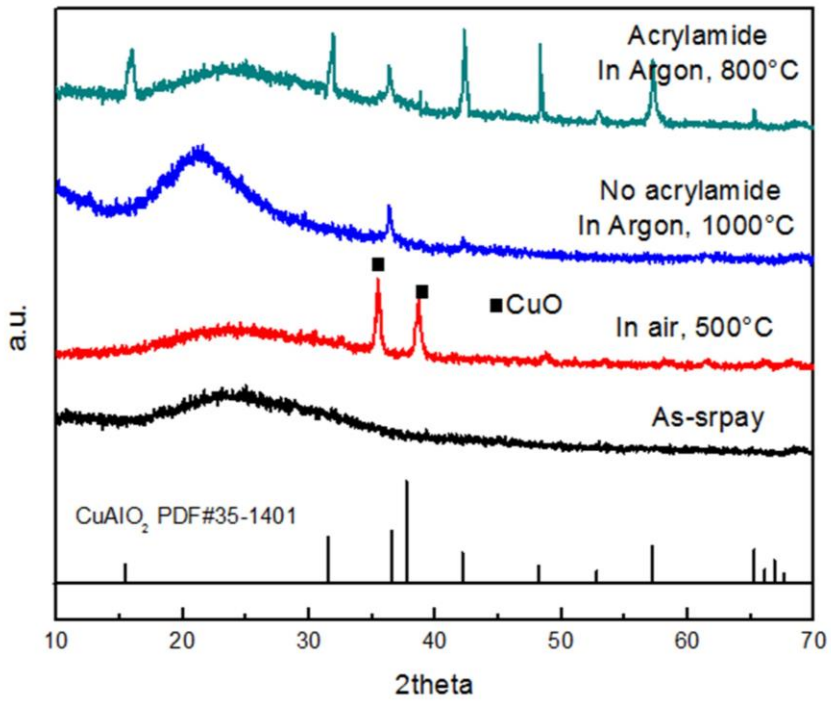

Figure 11. XRD patterns of electrosprayed thinfilms via different thermal history.

The crystallized thinfilms exhibited dense surface, as shown in Figure 12. The film with original spray time of 15min and 2h were compared after calcination. The thickness of the calcined film increased significantly with the increase of spray time, while the surface microstructures looks similar. The cross-section images also show quite uniform coating on the quartz substrate.

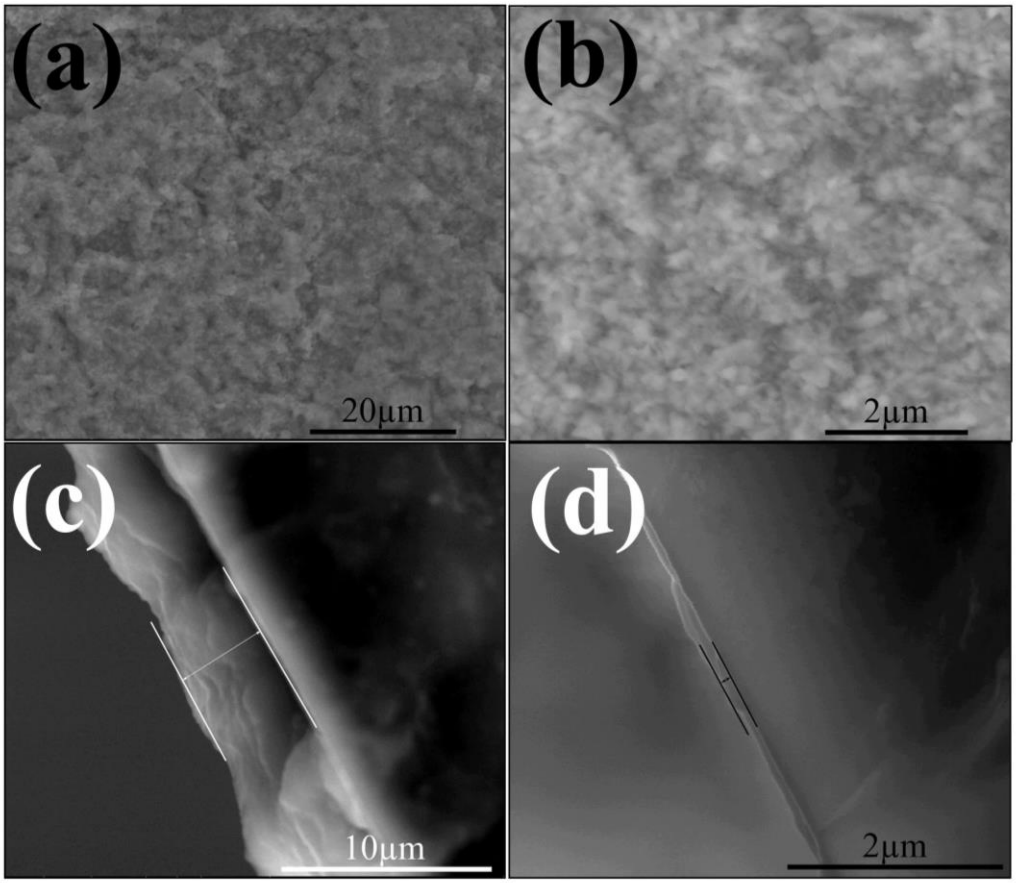

Figure 12. The film microstructure after calcination at 800°C for 5hr. Top(a) and cross-section(c) view of the 2h sprayed thin film; top(a) and cross-section(c) view of the 15min sprayed thin film.

In this study, other calcination conditions were tested. Figure 13 shows some cross-section micrographs under different calcination conditions. It could be seen that calcination at 800°C for 2hr is not sufficient for crystallization and the morphology still looks at amorphous. At elevated temperatures, occurrence of warping was observed, as shown in Figure 13 (b) and (c). In the case where acrylamide gelling was not used, needle-like microstructure was observed. The needle-like microstructure of undoped $CuAlO_2$ has been reported elsewhere[108] and it seems that the formation of need-like microstructure is quite random. Even though this microstructure might be interesting for further study, especially for surface applications, this is not within the scope of this study and will not be discussed in more details.

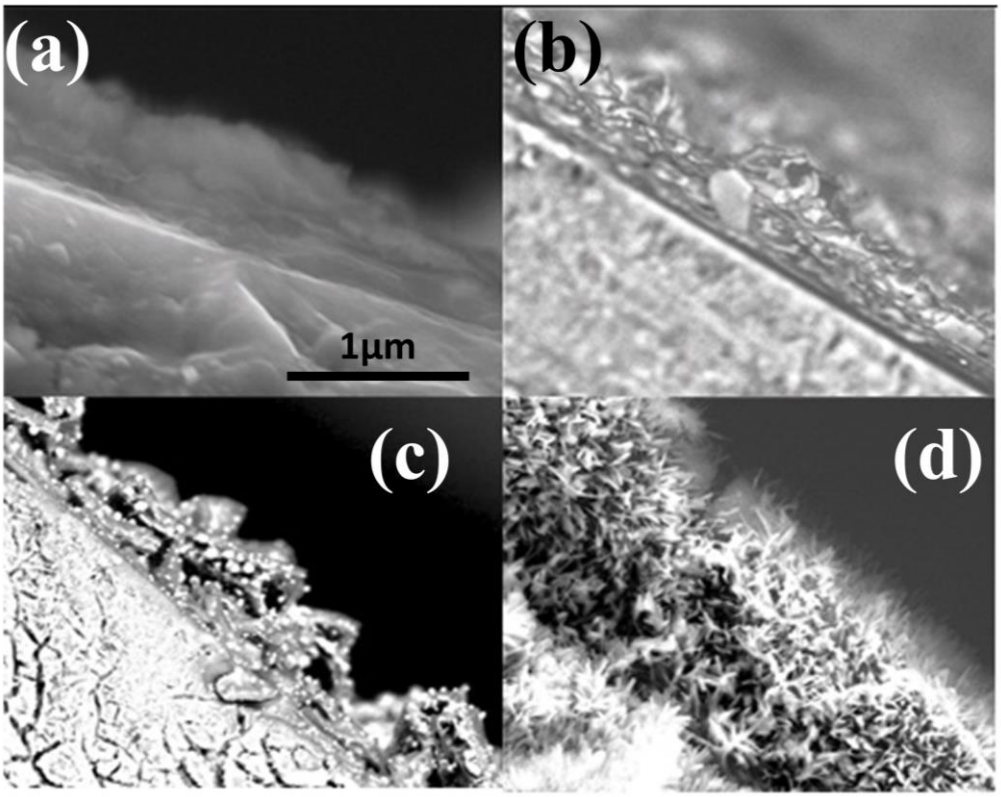

Figure 13. Cross-section microstructure of the film after calcination. (a) 800°C, 2hr; (b) 1000°C, 2hr; (c) 1000°C, 5hr; (d) without acrylamide, 1000°C.

Figure 14 and Figure 15 show the EDS and visible transmittance spectra of the $CuAlO_2$ thinfilm. In the EDS spectra, no carbon-related peak was detected, which implies that all the organics have been removed. The atomic ratio of Cu/Al is ~0.98(3). The strong Si peak is due to the quartz substrate. The resistivity measured at room temperature is 689 Ω·cm, which is larger than some of the reported resistivities. After calcination, the color of the film appeared to be dark brown and showed transmittance of ~45% at 700nm.

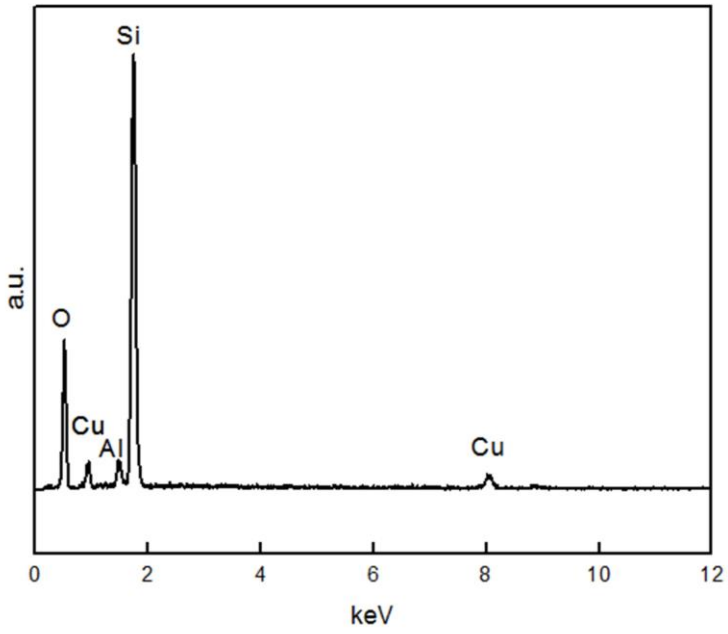

Figure 14. EDS spectra of $CuAlO_2$ thinfilm.

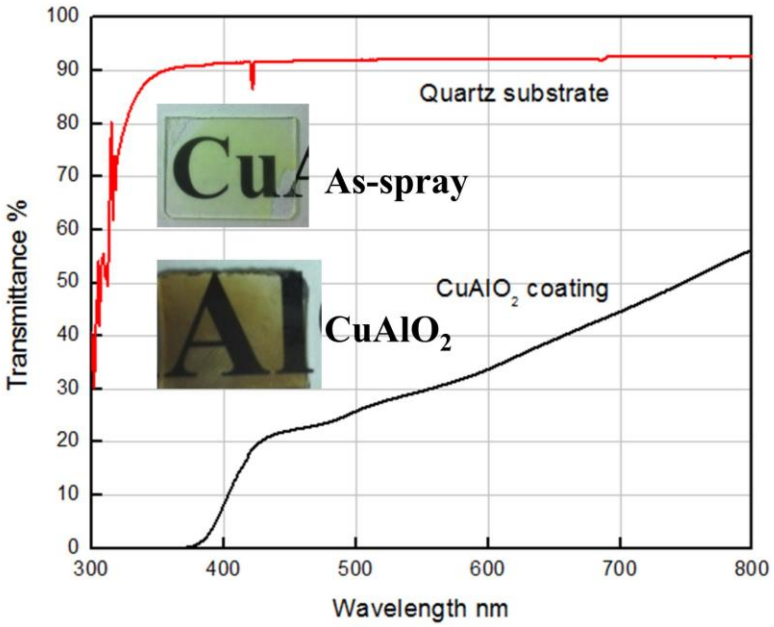

Figure 15. Visible transmittance of electrosprayed $CuAlO_2$ thinfilm. Digital images show the polymeric film and the crystallized $CuAlO_2$ film after calcination.

D. Electrospinning of $CuAlO_2$ fibers by a modified sol-gel method

The precursor for electrospinning utilized a sol-gel method, mainly due to two reasons. Firstly, the acrylamide route involves toxic reagent and is not suitable for large-scale production. Secondly, the electrospinning process, which involves the addition of high molecular-weight polymers, may confront difficulties by using acrylamide gelling solution. Therefore, a nitrate-citrate sol-gel system was used with addition of PVP to increase the viscosity of the precursor. As the viscosity of the precursor increases, the product from EHD process ranges from droplet to fibers, as shown previously in Figure 7. Prior to synthesizing the $CuAlO_2$ fibers, the viscosity of the solution was studied in an attempt to achieve uniform and non-woven fibers. Figure 16 shows the viscosity of solutions with different PVP content. All the viscosity curves in Figure 16 (a) exhibit linear shape, indicative of Newtonian fluid in all solutions. There is a drastic increase of viscosity when 60 wt.% PVP was added. The solution looks little yellowish and becomes viscous at room temperature. This trend can be seen more clearly in Figure 16 (b), in which the viscosity at a shear rate of 10 s^{-1} is compared among 5 solutions.

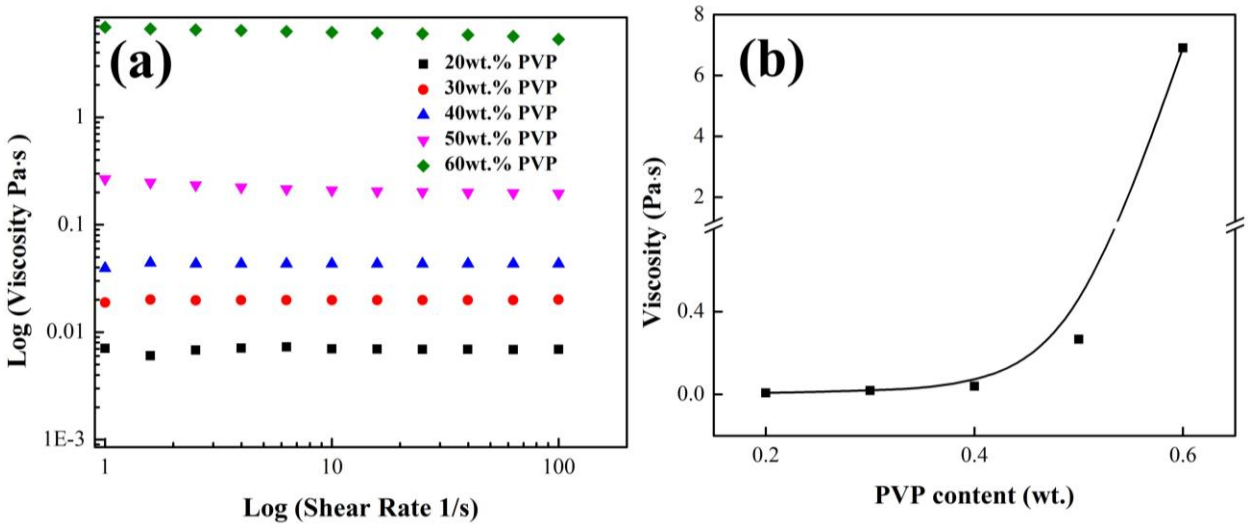

Figure 16. Precursor viscosity of different PVP loading: (a) Viscosity as a function of shear rate, in log scale; (b) PVP solutions viscosity at shear rate 10 s^{-1}.

The electrospun microstructures corresponding to solutions with 30, 40, 50, 60 wt.% PVP are illustrated in Figure 17. At the PVP loading of 30%, spherical droplets were

formed with various dimensions. When compared to the amorphous and smooth thinfilm in the case of electrospray, the electrospun droplet jet maintains spherical shape onto the collector, mainly due to the increased viscoplasticity. In the former case, the droplet bursts when reaching the collector. When the surface tension increases with the increase of viscoplasticity, the surface tension could withstand the deposition process. In addition, the size of the as-spun polymeric droplet is significantly larger than that of electrospray, which further implies that the droplet size increased due to introduction of PVP. As the PVP loading increased to 40%, some ribbon-like structure occurred. Because of the increased viscosity, the droplet along the longitude direction was elongated in the electric field. However, the viscosity is not sufficient to withstand the electrohydrodynamic force and the elongation is interrupted. With a further increase in PVP concentration, the elongated polymeric feature is more evident. When the viscosity reached ~8 Pa·s, uniform and continuous fiber structure was obtained.

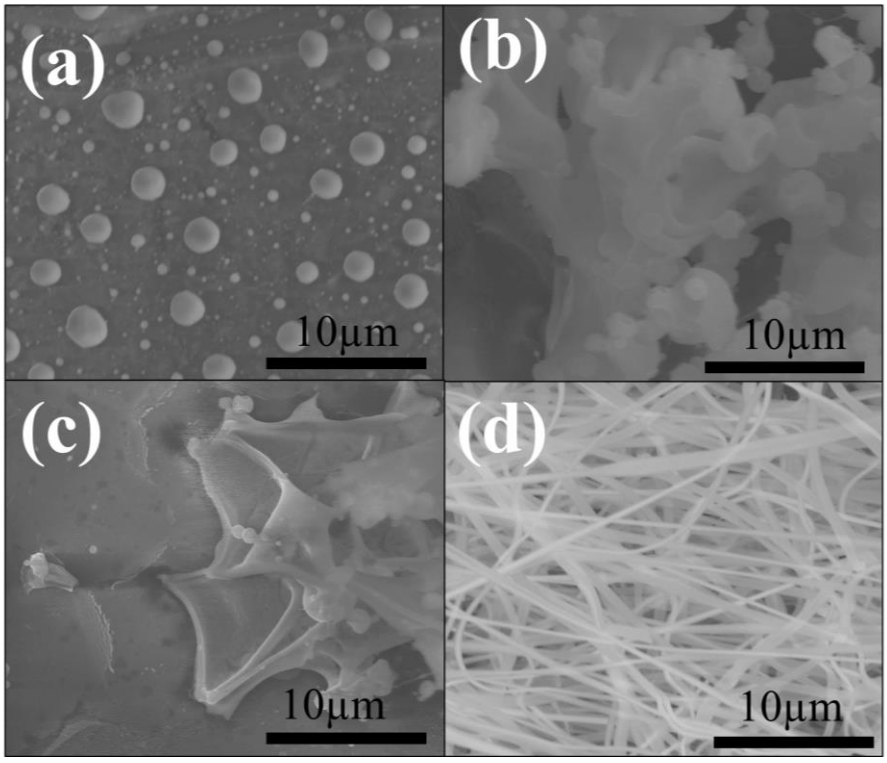

Figure 17. Electrospun polymeric fibers from solutions with different PVP loading: (a) 30 wt.% PVP; (b) 40 wt.% PVP; (c) 50 wt.% PVP; (d) 60 wt.% PVP.

Other parameters are identical: voltage 18 kV, working distance 15cm, flow rate 1mL/h.

During the electrospinning, the spinning voltage is also critical in determining the final microstructure. Figure 18 shows the microstructure evolution with the increase of spinning voltage. it could be seen from Figure 18 (a)-(c) that the fibers are connected with some beads, which is caused by insufficient elongation from the feed droplet. The dimension of the beads also decreased at increased voltages.

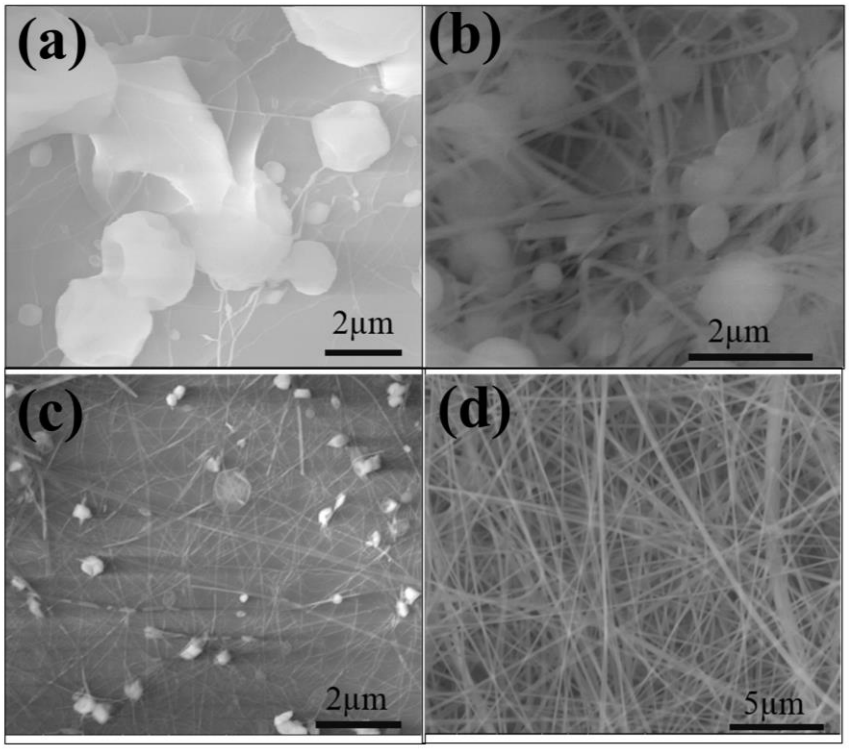

Figure 18. Electrospun polymeric fibers at different voltages: (a) 5 kV; (b) 10 kV; (c) 15 kV; (d) 20 kV, with other identical electrospinning parameters: 60wt% PVP solution, 15cm working distance, 1mL/h flow rate.

The fibers were then calcined in a muffle furnace in air, during which course the organics were removed and the polymeric fibers eventually turned into ceramic fibers. The thermogravimetric curve (Figure 19) shows The TG curve consists of three stages of weight loss. The first weight loss event occurred at ~100 °C, which could be attributed to the volatilization of adsorbed water and surface organics. The second event, at ~225 °C, is accompanied by a strong thermopositve peak in the DTA signal. This is due to the

decomposition of PVP lateral chains and the nitrate salts. The third stage of weight loss begins at 400°C, with a small thermal positive peak, which could correspond to the further burnout of PVP fundamental chains [109,110]. At above 800°C, the TG curve exhibits a broad endothermic peak in the DTA curve. The TG plateau indicates that the thermal decomposition process was complete and the decomposed copper and aluminum nitrate undertook a combination reaction to finally form $CuAlO_2$. The overall weight loss is nearly 80%, given the large amount of PVP addition into the precursors required to yield ideal elasticity for electrospinning.

The TG plateau indicates that the thermal decomposition process beyond 800°C in flowing air was complete and the decomposed copper and aluminum nitrate undertook a combination reaction to finally form $CuAlO_2$. The thermodynamic window for $CuAlO_2$ synthesis should therefore set beyond 800°C. In this regard, different annealing temperatures were tested as shown in the XRD (Figure 20). The as-spun polymeric fiber shows amorphous and upon annealing at 500°C, only CuO is present. Annealing at 900C, the spinel $CuAl_2O_4$ is formed, because the $CuAl_2O_4$ and CuO phases containing Cu(II) are stable at the temperature range of 625 to 1000ºC whereas the delafossite $CuAlO_2$ is a metastable phase below 1000ºC.

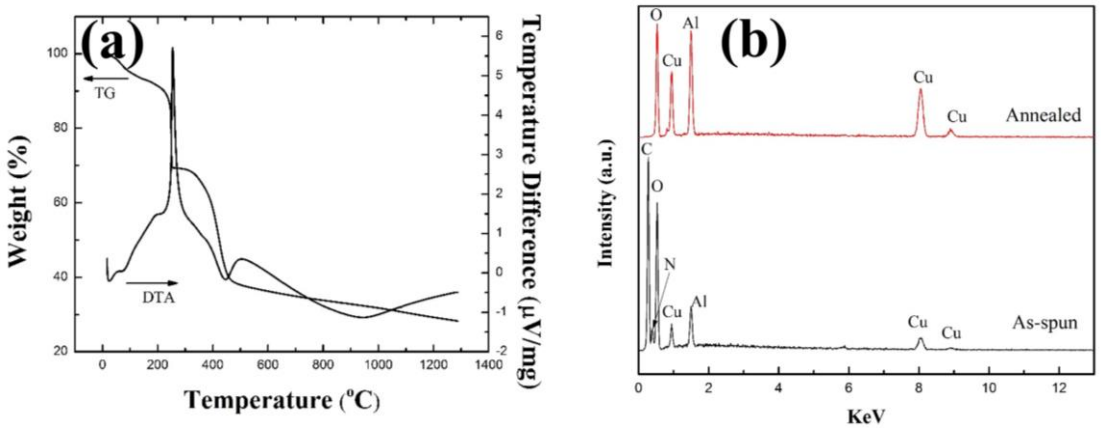

Figure 19. (a) TG/DTA curves of the as-spun fiber heated up to 1300°C in air; (b) EDS spectra of as-spun and annealed fibers.

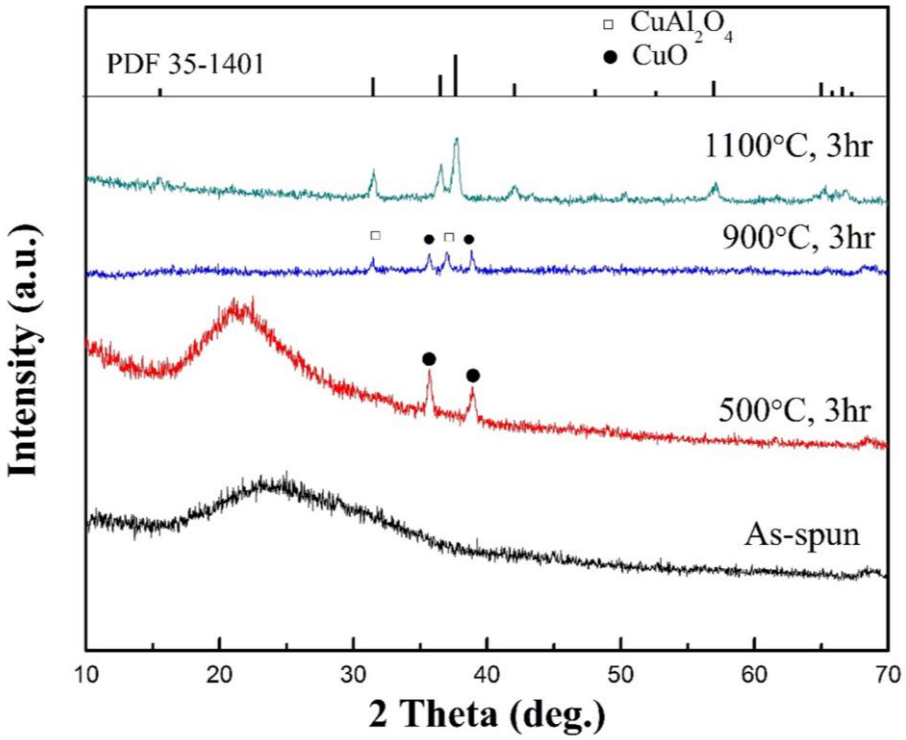

Figure 20. XRD patterns of polymeric fibers calcined at different temperatures.

The microstructure of the annealed fibers is shown in Figure 21. The fibrous structure was maintained after the calcination. Very fine grains could be observed on the fibers. The dimension of the fiber was measured by Nanomeasure software and is presented in Figure 21(c). It could be seen that the average fiber diameter is ~160nm and most of the fibers dimension fall into a narrow range, which indicates that the fibers prepared through electrospinning is quite uniform.

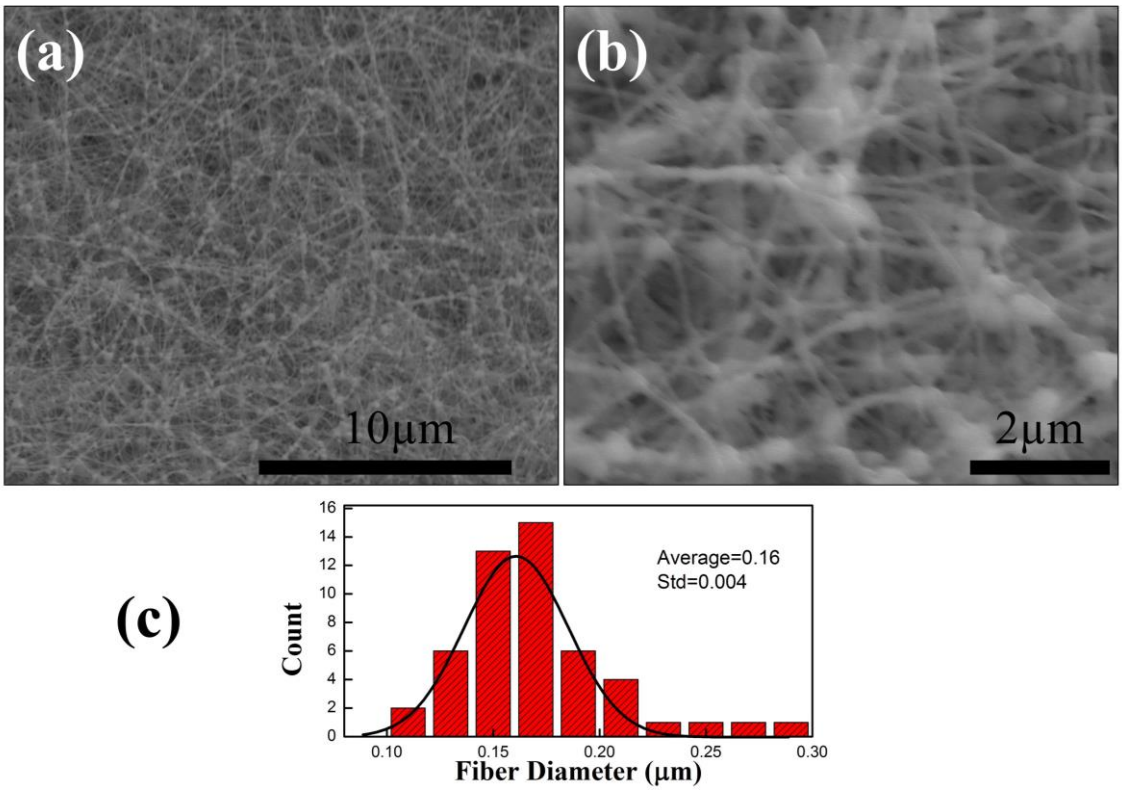

Figure 21. SEM images of the $CuAlO_2$ ceramic fibers calcined at 1100°C for 3h, with low (a) and high (b) magnifications: (c) Fiber diameter distribution with Gaussian fitting.

Figure 21 depicts the fine fiber structure under 1100°C treatment. However, as mentioned before, during the heat treatment the transformation of polymeric fiber to ceramic fiber undergoes several stages. In order to reveal the fiber evolution during heat treatment, the fiber diameter is measured as a function of treatment temperature (with 3h dwelling in all cases). Figure 22 clearly demonstrates that the fiber diameter decreases at first and increases later with the increase of treatment temperature. Recalling Figure 19 (a), the initial organics burn off occurs at ~500°C, followed by partial crystallization of CuO. Since the organics have not been completed removed, the fiber dimeson continues to decrease. Beyond 800°C, at which point $CuAlO_2$ begins to form, the pure ceramic fibers are formed and begin to grow at elevated temperatures.

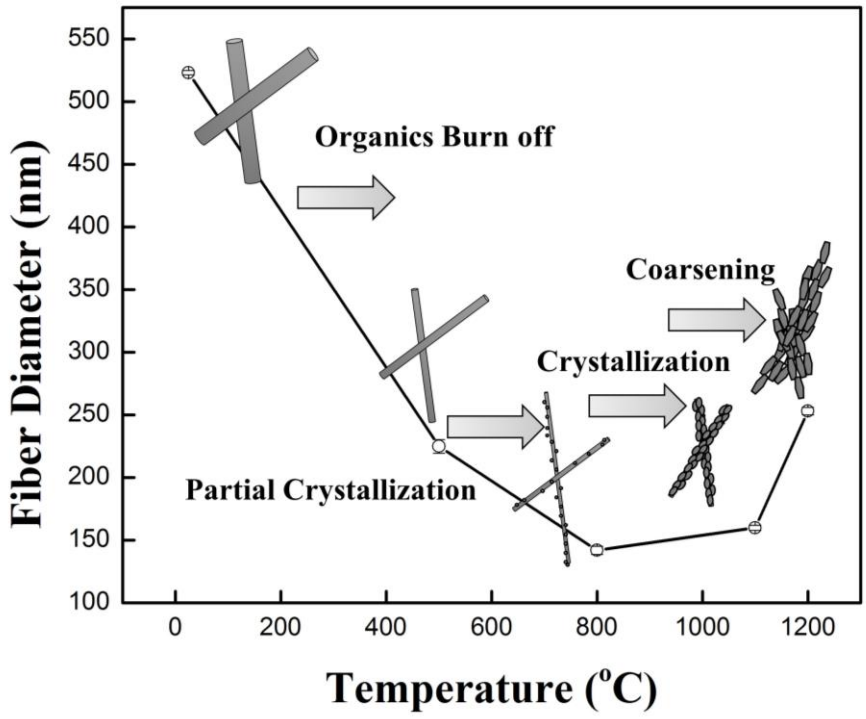

Figure 22. Evolution of fiber dimension as a function of treatment temperature during calcination. The dwelling is 3h. Fiber dimension is based on measuring 100 fibers.

E. Summary

In this chapter, the electrohydrodynamic processing was employed to fabricate $CuAlO_2$ thinfilms and nanofibers through acrylamide and sol-gel routes, respectively. The $CuAlO_2$ thinfilms exhibit moderate visible transmittance and sheet resistivity, after calcined at only 800°C. The film via electrospray and post-calcination is dense and uniform. The electrospinning parameters, as well as the precursor viscosity, were investigated in order to fabricate uniform and continuous fibers. The transformation of polymeric fibers into ceramics fibers involves diminution of the polymeric fiber, crystallization and coarsening of the ceramic fibers. In both cases, the deposition time of the electrohydrodynamic process is relatively short and could be performed at ambient atmosphere. Finally, phase-pure delafossite $CuAlO_2$ was obtained. The electrical and optical properties will be further discussed in later chapters.

MODELLING OF ELECTROSPINNING PROCESS: JET INSTABILITIES AND FIBER DIMENSION PREDICTION

A. Introduction

A major part of the current study utilized electrospinning as a main electrohydrodynamic process technique to fabricate $CuAlO_2$ materials. The microstructure evolution, as well as the influence of electrospinning parameters such as voltage and viscosity on fiber morphologies have been discussed in previous chapter. The experimental results have revealed a strong correlation between electrospinning parameters and fiber microstructure. In other words, the electrospinning process could be highly controllable. The electrohydrodynamic behavior of a droplet during the electrospinning process is more complicated than electrospray process. In a typical electrospinning process, after the Taylor cone is formed under equilibrium between surface tension and electrical force, a slender and continuous liquid filament is formed and accelerates to the collector. The filament will then undergo thinning and whipping before reaching the collector. Reneker al. [111,112] proposed that straight jet could be only stabilized for a small distance away from the nozzle. The repulsive forces (Coulomb force) between adjacent charged filament will later cause lateral perturbation, which further leads to bending instability within the slender jet stream. Several models have been developed to model the electrospinning process of polymeric jet, such as Lattice Boltzmann method[113], linear Maxwell method[112,114], and non-linear upper convected Maxwell method[115]. All the methods hold a common view that the jet consists of individual filament or beads, which are electrified and exhibit strong Coulomb interaction. For the first part of this chapter, a mathematical model derived from Reneker's model was used to simulate the jet trajectory. The second part will focus on the prediction of terminal jet diameter.

B. Mathmatical model and coding

After the Taylor cone is formed, the fluid jet is treated as segments of individual beads, as shown in Figure 23. For an individual bead, the electric force could be described as follows:

$$f_e = -e\frac{V}{h} \tag{4}$$

where e is the electron charge, V is the external applied voltage and h is the working distance, as shown in Figure 23. According to the common jet treatment from most of the modelling methods, two adjacent beads in the slender jet are interconnected under viscoelastic force. For a single bead i with mass m and charge e, the two adjacent beads i-1 and i+1 impose two viscoelastic force components on bead i, which is:

$$\begin{aligned} f_v = {} & \pi a_{i+1}^2 \sigma_{i+1}[i\frac{x_{i+1}-x_i}{l_{i+1}} + j\frac{y_{i+1}-y_i}{l_{i+1}} + k\frac{z_{i+1}-z_i}{l_{i+1}}] \\ & -a_{i-1}^2 \sigma_{i-1}[i\frac{x_i-x_{i-1}}{l_{i-1}} + j\frac{y_i-y_{i-1}}{l_{i-1}} + k\frac{z_i-z_{i-1}}{l_{i-1}}] \end{aligned} \tag{5}$$

This equation contains x-y-z coordinates and the l is the distance between two beads, σ is the viscoelastic stress and a is the jet radius for a specified bead. Assuming the initial jet diameter out from the nozzle at t=0 is a_0, the mass conservation still holds throughout the jet liquid, there are:

$$a_i = a_0\sqrt{L/l_i} \tag{6}$$

$$a_{i\pm N} = a_0\sqrt{L/l_{i\pm N}} \tag{7}$$

where L is the screening length scale and could be defined as a function of initial diameter at t=0 and elastic modulus G:[112]

$$L = \sqrt{\frac{e^2}{\pi a_0^2 G}} \tag{8}$$

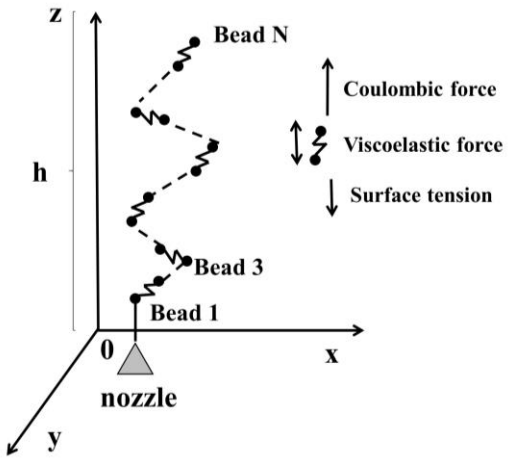

Figure 23. Segments of individual beads. The dumbbell consisting of two beads indicates viscoelastic force, Coulombic force and surface tension. The working distance is denoted as h.

In Figure 23, there are two other force components acting on bead i, which are Coulombic force and surface tension of opposite direction. The Coulombic force in 3-dimensional coordination could be expressed as:

$$f_c = \sum_{\substack{m=1 \\ m \neq i}} \frac{e^2}{l_{im}^2}\left(\mathrm{i}\frac{x_i - x_m}{l_{im}} + j\frac{y_i - y_m}{l_{im}} + k\frac{z_i - z_m}{l_{im}}\right) \tag{9}$$

Equation 9 includes the total Coulombic force acting on bead i, since the Coulombic force is dependent on all surrounding bead. The surface tension could be described as:

$$f_c = -\frac{a\pi\bar{a}^2 k_i}{\sqrt{(x_i^2 + y_i^2)}}[\mathrm{i}|x_i|\mathrm{sign}(\mathrm{x}_i) + \mathrm{j}|y_i|\mathrm{sign}(\mathrm{y}_i)] \tag{10}$$

$\bar{a}$ is the average bead radius of i+1 and i-1 beads around bead i. k_i is the curvature of bead i, which could be directly calculated in the x-y coordinate. Figure 24 illustrates the geometric parameters for calculating curvature k.

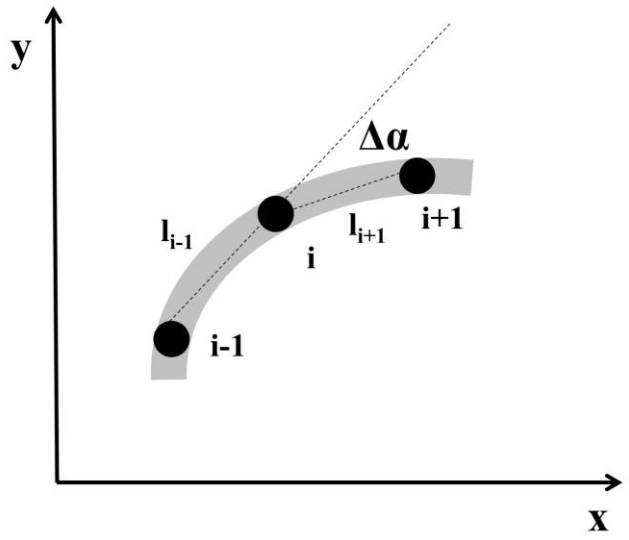

Figure 24. Schematic diagram of jet curvature of bead i.

The curvature k_i at bead i could be calculated as:

$$k_i = \left| \frac{\Delta\alpha}{l_{i-1} + l_{i+1}} \right| \tag{11}$$

Given the electric force(4) viscoelastic force(5), Coulombic force(9) and surface tension(10), the total force applied on bead i during electrospinning could be written as: (bead position could be assigned $r_i = ix_i + jy_i + kz_i$)

$$\begin{aligned} m\frac{d^2 r_i}{dt^2} = -e\frac{V}{h} + \sum_{\substack{m=1 \\ m\neq i}} \frac{e^2}{R_{im}^2}(r_i - r_m) + \frac{\pi a_{i+1}^2 \sigma_{i+1}}{l_{i+1}}(r_{i+1} - r_i) \\ -\frac{\pi a_{i-1}^2 \sigma_{i-1}}{l_{i-1}}(r_i - r_{i-1}) - \frac{a\pi a^{-2} k_i}{\sqrt{(x_i^2 + y_i^2)}}[\mathrm{i}\left|x_i\right|\mathrm{sign}(\mathrm{x}_i) + \mathrm{j}\left|y_i\right|\mathrm{sign}(\mathrm{y}_i)] \end{aligned} \tag{12}$$

Equation (12) is a second-order partial differential equation in x-coordinate. In order to solve this equation, a differential equation solver ode45 in MATLAB (version: R2014a, MathWorks, Natick, MA) was used. The ode45 solver is based on an explicit Runge-Kutta method. Based on equation (12), the bead position at a certain integrated

time, as well as velocity could be calculated. The number of beads (N) modelled is 500. The converted variables from equation (12) to the MATLAB code is shown in Appendix. The main program consists of the initial conditions, electrospinning parameters and partial differential equation derived from equation (12). The complete code is also included in appendix.

C. Instability of the trajectory of the jet

The header of the MATLAB code defines the initial conditions and electrospinning parameters. The detailed parameters and their values are shown in Table II. The simulation of electrospinning process by varying the viscosity is shown in Figure 25. At low viscosity, the simulated jet involves multiple trajectories along z-axis. No stable and single jet is formed in this case. When the viscosity is set to higher values, stable jet could be formed. A comparison between Figure 25(b) and (c) shows that a higher viscosity could achieve a longer stabilized trajectory before whipping occurs.

Table II. Physical Parameters Used to Model the Electrospinning Process.

Parameters	Value
Modelling time (tfinal)	0.02 s
Number of beads (N)	500
Working distance (h)	0.15 m
Bead mass (m)	0.3E-8 kg
Charge (e)	2.83E-9 C[112]
Voltage (V)	15000 V
Elastic modulus (G)	1E8 Pa[116]
Viscosity	7.5 Pa·S
Length scale (L)	2E-3
Initial radius (a_0)	500E-6 m
Surface tension (α)	0.7[112]

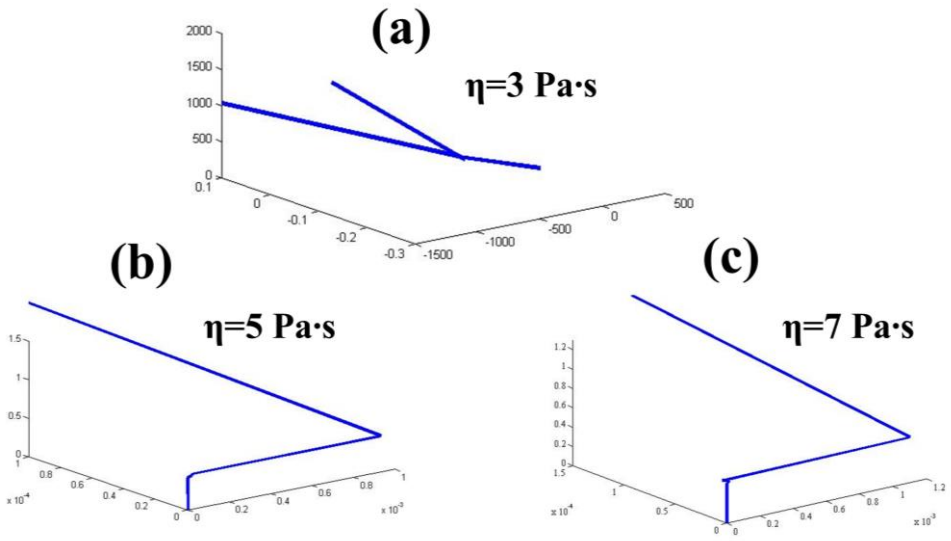

Figure 25. Simulated electrospinning process with modified viscosity.

D. Predicting the terminal fiber diameter during electrospinning

The second part of this chapter is focused on predicting the terminal fiber diameter. According to the simulation data, the instability of the jet occurred under all modelling conditions. With the fiber thinning and transport downstream towards the collector, the surface tension eventually balances the charge repulsion, leading to a settled fiber diameter, namely, the terminal fiber diameter. Since the output of the aforementioned model only include bead positions, it is necessary to find alternatives to correlate final fiber dimension with other electrospinning parameters. In this regard, we recalled the equation (3) in Chapter 1, which finds a relation between jet terminal diameter h and (Q/I). However, it is noteworthy that this equation neglects the viscoelastic force between neighboring beads. At the final stage of electrospinning, the jet is away from the origin and undergoes drying process, which has less elastic force.

Table III summarized the experimentally acquired jet currents and fiber diameter. It could be seen that in the case of PVP electrospinning, the jet current increases with the increase of flow rate. By increasing the applied voltage, there is a slightly decrease in fiber diameter, possibly due to the higher electric force. According the equation (3), the log of fiber diameter follows a linear relationship with the log of (Q/I), which is the ratio

of flow rate to jet currents. Figure 26 plots such logarithmic relationship based on experimental results. It could be seen that all data points could be fitted linearly. The slope of the experimental fitting from two voltages is similar. However, there is a large discrepancy from theoretical prediction based on equation (3).

Table III. Experimental Flow Rate, Jet Current and As-Spun Fiber Diameter.

	Flow Rate (mL/min)	Voltage (V)	Jet Current (A)	Diameter (m)
15kV	60	2.20E-03	2.20E-08	5.24E-07
	42	1.90E-03	1.90E-08	4.78E-07
	30	2.10E-03	2.10E-08	4.45E-07
	18	1.50E-03	1.50E-08	3.96E-07
	6	1.30E-03	1.30E-08	3.32E-07
	Flow Rate (mL/min)	Voltage (V)	Jet Current (A)	Diameter (nm)
25kV	60	4.80E-03	4.80E-08	4.75E-07
	42	4.20E-03	4.20E-08	4.52E-07
	30	3.50E-03	3.50E-08	3.98E-07
	18	2.80E-03	2.80E-08	3.64E-07
	6	6.00E-05	6.00E-10	341

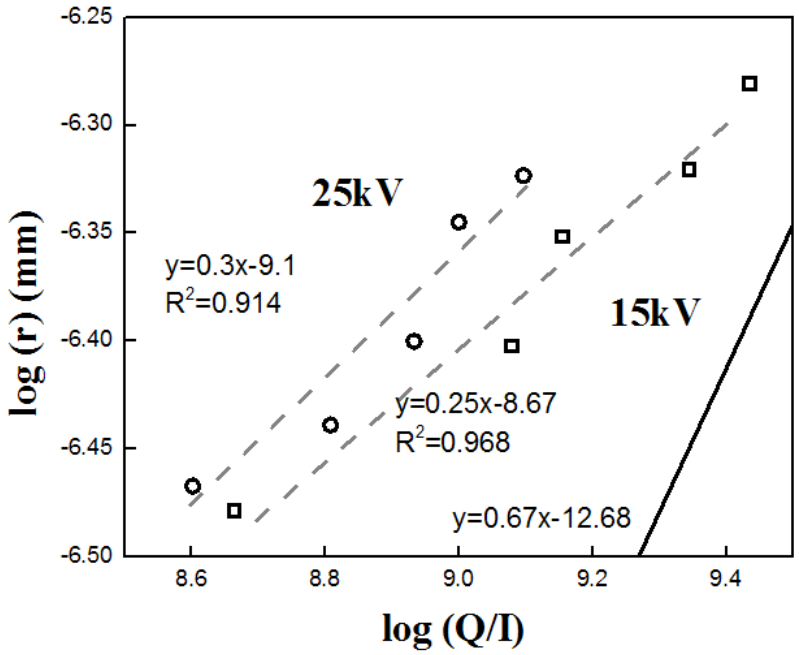

Figure 26. The log of terminal fiber diameter r versus the log of (Q/I). The electrospinning voltage is set as 15 and 25kV. Dashed lines denote the experimental fitting and solid line denotes the theoretical prediction.

E. Summary

The simulation of electrospinning process was simulated by solving the second-order differential equations based on Newton's second law. The inclusion of viscoelastic force, electric force, Coulombic force and surface tension could yield a suitable electrospinning model. In this case, the viscosity of the bead was modified and the simulation results were compared to the experimental results. At high viscosity, the simulation shows that a stable jet could be formed at ~0.4mm away from the nozzle. The stabilized distance decreases with the decrease of viscosity. Instability of the jet trajectory is observed during simulation. When the viscosity is below 5 Pa·s, multiple random trajectories were observed due to the failure of convergence equation, which indicates that the stable and single jet could not be formed. The prediction of fiber diameter was also attempted. The experimental results reveal a quite log-linear relationship between the inverse of volume charge density and final fiber dimension. The large discrepancy between experimental results and prediction may result from perturbation of the jet, as demonstrated by the early simulation in this chapter.

THE Y^{3+} DOPED $CuAlO_2$: OPTICAL AND ELECTRICAL PROPRETIES

A. Introduction

$CuAlO_2$ is a typical p-type transparent oxide which has a wide bandgap (>3eV) and room temperature photoluminescence due to the UV near-band-edge emission through the recombination of free excitons [117-120]. The delafossite structure in the class of $CuMO_2$ (M site accounts for trivalent ions) materials allows for chemical bond stretching from either Cu-O bond (xy-plane) or M-O bond (z-direction) and it is widely acknowledged that the electrical properties are limited by carrier compensation through local lattice relaxations. The electronic density towards different oxide ligand can be altered by changing M site cations. Therefore in order to increase the intrinsic electrical conductivity of delafossite $CuAlO_2$, introducing divalent or trivalent doping as impurities or substitute into the layered crystal lattice is the main attempt to enhance the performance of p-type transparent conducting oxides [121]. As a result, reduced effective mass and band gap tuning usually occurs even though there is still lack of knowledge in interpretation of the doping mechanisms, as well as some inconstancy between bandgap engineering and electrical measurements data. It is also noteworthy that in addition to visible transmittance and electrical properties, delafossite $CuAlO_2$ also presents UV near-band-edge emission at room temperature which makes it suitable for LED applications. The direct transition of carriers from valence band to conduction band and the recombination of free excitons lead to the luminescence in the UV range. The luminescent properties can be affected by copper environment in which the off-centered monovalent copper is linearly coordinated with the antiprismatic oxygen. The size of M^{3+}-cation corresponds to the stretching or relaxation in the Cu-O bond and therefore affect the electronic density and photoluminescence spectra. The idea of M^{3+} site doping with trivalent ions has been developed in recent years and the effects of the dopant have been discussed in the morphological and electrical perspective [4]. In their discussion, the phenomenon of O intercalation as a result of lattice distortion contributes to the variation in resistivity. However, probing the effect of trivalent dopant via luminescent or other optical methods has not been reported to the best of our knowledge.

In the present work, ceramic EHD processed $CuAlO_2$ thinfilms and nanofibers have been prepared in their form on quartz substrates for luminescence characterizations. The characterization of Y^{3+}-doped CuAlO2 were performed. Moreover, near-band-edge emission at room temperature was identified and the dielectric constant could be estimated in the high frequency region. The effective mass, together with band-gap enhancement could be extracted from these transparent fibers coated samples to quantify the intercalation of yttrium affecting the host band-edge.

B. Charaterization of Y^{3+}-doped $CuAlO_2$ thinfilms.

Due to the poor p-type conductivity of delafossite $CuAlO_2$, there have been many attempts to improve the electrical conductivity, such as divalent doping [35-37] and nitrogen doping[122]. Trivalent dopant in substitution of the Al site, has become a new experimental interest in recent years. Based on some calculation results,[2] the substitution doping is predicted to increase the density of states at the top of the valence band. Additionally, the change of M-O covalency could lead to a decrease of O valance charge in the Cu-O-Al unit, which finally mediates the Cu d states and an improved conductivity would be expected. Inspired by the $CuYO_2$ compounds and the potential alloying effects, Y ion was chosen to partial substitute Al site. Figure 27 depicts three typical electrical characterization methods. All the samples exhibited semiconducting conductivity with a monotonically reduced thermal activation energy as the yttrium doping increased. Even though the various hopping mechanisms in $CuAlO_2$ have been reported, at the measured temperature range, the linearity indicted a thermal activation type hopping. Recalling the change of optical direct band gap shown in Figure 27(c), the introduction of yttrium modified the band edge and might change the Cu-O confinement to a degree that the excitons underlying the valence band became more delocalized, thus decreasing the activation energy when thermally excited from VB to CB. The overall resistivity obtained from calculating the V-I slope shows a decrease from 689 Ω·cm to 580 Ω·cm as the Y concentration goes up from 0 to 5at. %. The room-temperature sheet resistivity and optical band-gap are shown in Table IV. Even though the improvement is very small, the consistency lying within the band-gap, resistivity and thermal activation energy might indicate that the substitutional trivalent doping with orderly alloying effects could be

useful for a better understanding of the doping mechanisms compared to divalent doping, which may increase the charge complexity and obscure some underlying phenomena.

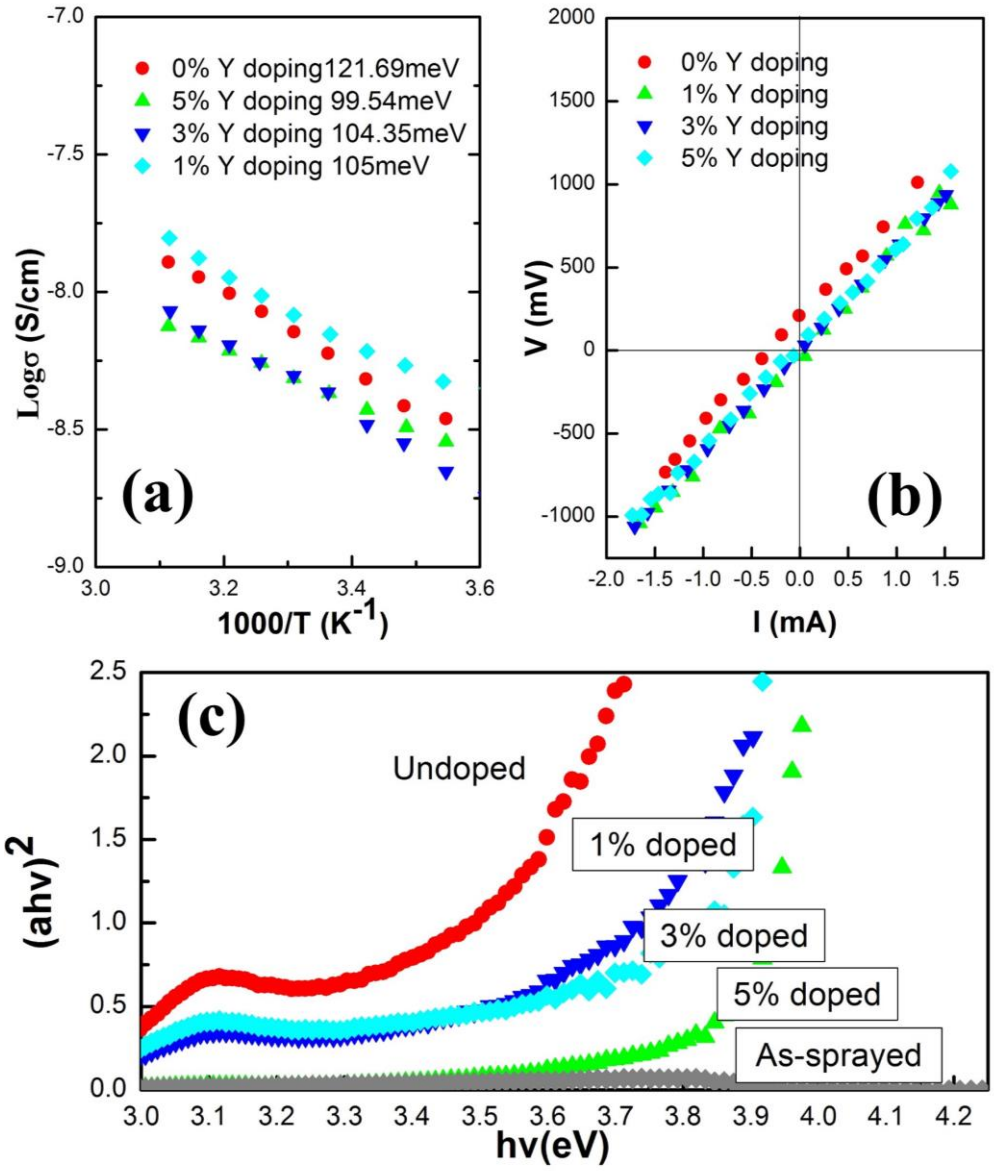

Figure 27. Summary of electrical properties of electrosprayed $CuAlO_2$ thin films: (a) Temperature-dependent DC conductivity; (b) Four-probe V-I curve; (c) Tauc plot extrapolated from UV diffuse reflectance.

Table IV. Room Temperature Sheet Resistivities and Optical Band-gap of $CuAlO_2$ Thinfilms.

Doping Level	0 at%	1 at%	3 at%	5 at %
Resistivity (Ω cm)	689	601	582	605
Band-gap (eV)	3.24	3.48	3.42	3.68

The fate of electrohydrodynamic is its simplicity in producing nanostructured coatings or thin films with high transparency in the visible region, which is highly favored by transparent conducting oxides. The samples could be easily deposited onto glass or quartz substrates due to the strong attractive force between charged jet and grounded collector. After annealing, the polycrystalline structure could be formed. The sample from electrospray has a lowered transmittance in the visible region in Figure 28. The transmittance spectrum has previously shown in Figure 15. The purpose here is to compare with the transmittance of electrospun fibers deposited on a quartz substrate. The dense polycrystalline delafossite anisotropic structure could enhance the beam scattering thus decreasing the transmittance. On the other hand, the electrospun sample with a stacking thickness of ~ 20μm[123], has a porous structure and due to the stacking of fiber mats and reduced contact area, the actual coating thickness absorbing the visible light could not be high. Therefore, the electrospun sample exhibited higher transmittance compared to the electrospray coating.

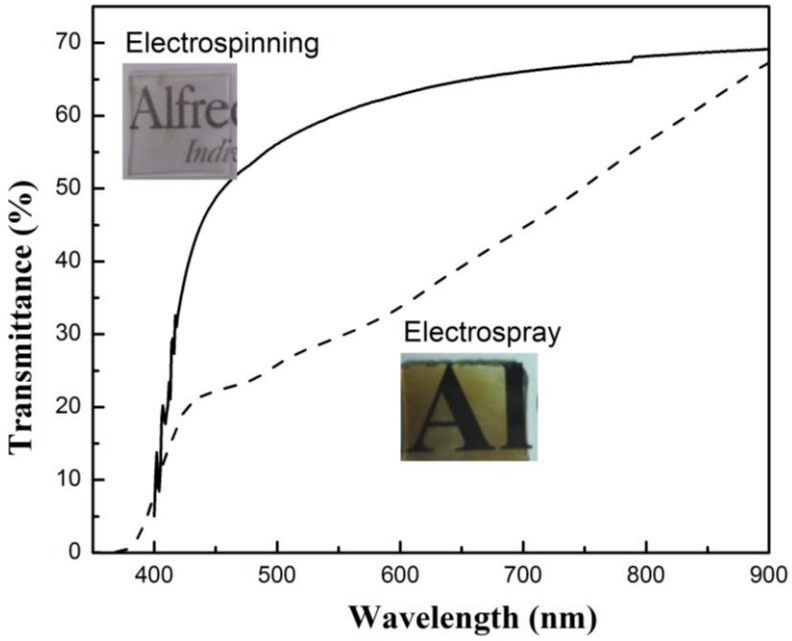

Figure 28. Transmittance spectra of CuAlO2 coatings from both electrospray and electrospinning.

C. Blueshift in near-band-edge emission in Y^{3+}-doped $CuAlO_2$ nanofibers

Polyvinylpyrrolidone nanofibers have been electrospun from a precursor solution containing equal molar quantities of copper nitrate trihydrate (99-104%, Sigma-Aldrich) and aluminum nitrate nonahydrate (98.0-102.0%, Sigma-Aldrich). Yttrium nitrate hexahydrate (99.8%, Sigma-Aldirch) was added as dopant source in quantities sufficient to replace 0%, 1%, and 5% of the Al^{3+}. The electrospun fibers were deposited on quartz substrate for later optical characterizations. Heat treatment of the nanofibers was then carried out at 1100°C to transform the polymeric fibers into crystalline $CuAlO_2$ fibers. The as-spun nanofibers were held at the elevated temperatures for either 2, 4, or 5 hours in order to obtain ceramic nanofibers with different crystallite sizes (shown in Table V). The average thickness of the nanofibers coated on quartz substrate was ~20µm. Photoluminescence studies (Horiba Spex FluoroLog Tau-3) were performed at room temperature using an excitation wavelength of 365nm. The CuAlO2 fibers coated on

quartz slide was directly measured. The slit was kept at 4/3 (ex/em) in order to normalize the spectra intensities in terms of wavelength among different samples.

Table V. Sample Crystallite Size Under Different Dwelling Time

Dwelling Time (hr)	Crystallite Size (nm)		
	undoped	1% Y	5% Y
2	23.04±0.057	17.52±0.23	19.5±0.38
4	26.07± 0.07	19.6±0.12	20.12±0.24
5	32.74±0.047	23.4±0.12	21.6±0.155

The fibrous fiber morphology was sustained after thermal annealing, which is shown in Figure 29 (a), (b) and (c). There was no evident difference in fiber diameter and coating thickness among samples with different doping levels. The XRD pattern (space group: R-3m) shows a prominent preferred orientation in the z-direction, which implied that the nucleation was initiated along the radial direction and the strong diffraction peaks were facilitated by the stacking fibrous layers. The Rietveld method was carried out in Bruker TOPAS and both the experimental and fitting deviation profiles were shown in Figure 30.

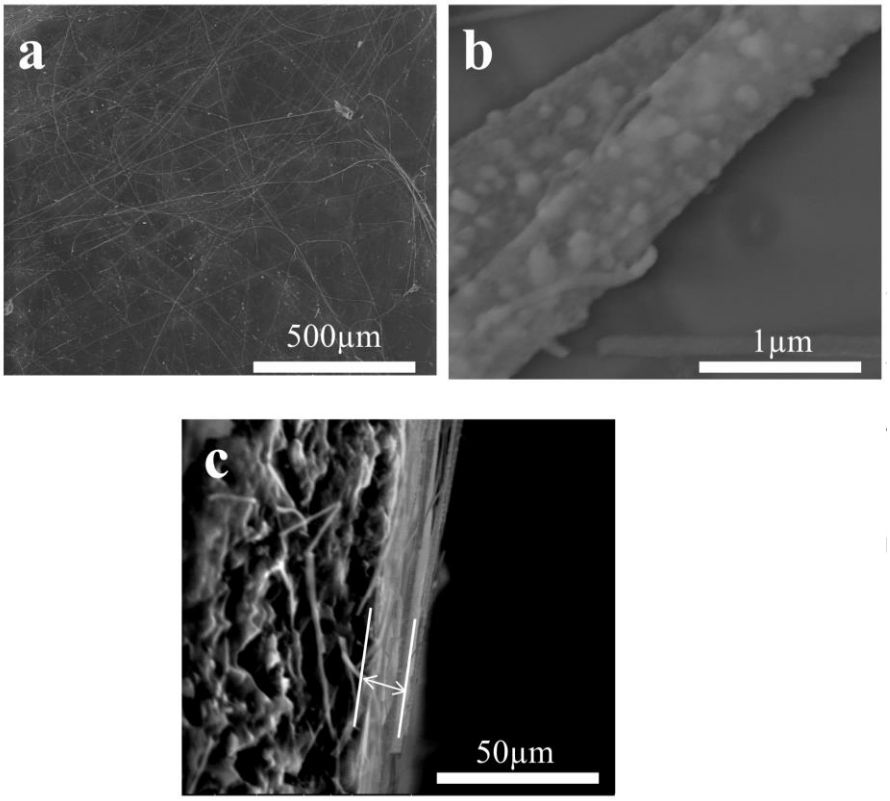

Figure 29. (a) and (b) SEM micrographs of CuAlO2:1%Y fibers electrospun on quartz; (c) cross-section image indicating the fiber thickness ~20μm.

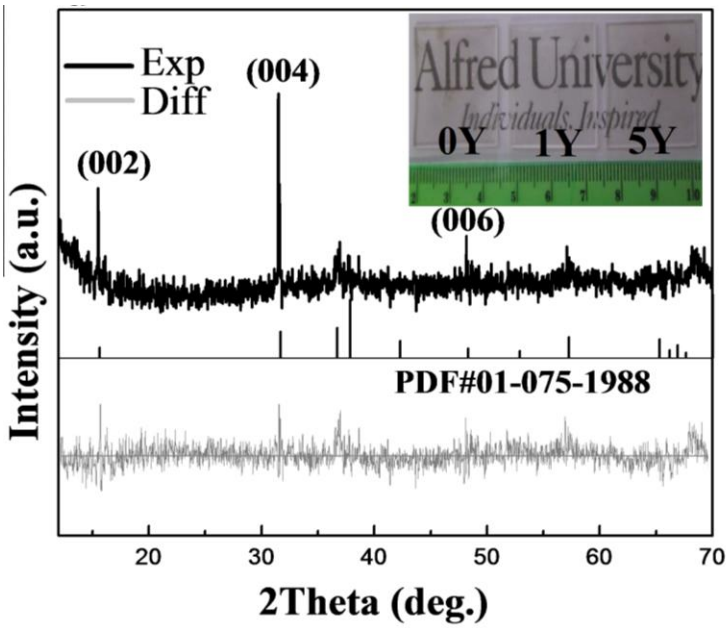

Figure 30. Experimental XRD pattern and fitting deviation profile. Inset shows the digital images of transparent fiber-coated quartz slides.

Since the bare quartz substrate is not luminescent, the broad emission peaks shown in Figure 31 belong to the direct transition of this wide band gap material. The PL spectra confirm that free excitonic emission can be expressed by wide band-gap oxides in which the bound excitons dominate only at low temperatures, and free excitonic emissions dominate at higher temperature (room temperature) due to strong localization of electron-hole pairs[124,125]. Superlattice materials, in which the charge carriers are confined to two dimensional regions, are known to show a concentrated localization of electron-hole pairs. This results in enhanced electron-hole interactions which effect the optical properties of nanomaterials. In delafossite $CuAlO_2$, the Cu-O bonds in the O-Cu-O dumbbell layers determine the electronic structure near the band-gap and lead to strong localization of excitons in the x-y plane as well as larger binding energy. Since the binding energy exceeded the room temperature thermal energy ($kT \approx 0.025eV$), room temperature PL emissions were presented. Figure 31 (a) shows that the undoped sample exhibited a broad peak centered at 458nm. The sample doped with 1% Y^{3+} peaked at 439nm while the sample with 5% Y^{3+} content peaked at 423nm. A previous study which investigated delafossite-type oxides such as $CuLaO_2$ and $CuYO_2$ identified the source of these luminescent spectra[47]. The luminescent spectra consist of two adjacent emission bands from the transition between $4p_{x,y}$ to $3d_z^2$-4s, and $3d_z^2$+4s to $3d_z^2$-4s. The $3d_z^2$+4s to $3d_z^2$-4s transition originated from hybridization of the $3d_z^2$ with 4s orbitals. Relaxation from the excited state causes the Cu-O bond to stretch, thereby decreasing the electronic density in the x-y plane and increasing the electronic density along the z axis. The introduction of yttrium did not modify the direct transition type. Instead, the degree to which the Cu-O bond was stretched by the introduction of the dopant resulted in the observed variations in peak location. The asymmetrical peak shape shown in the PL spectra was caused by an overlap of the two Gaussian peaks associated with the $3d_z^2$+4s to $3d_z^2$-4s transition of both $CuAlO_2$ and $CuYO_2$. Increased yttrium content correlated with narrower emission intensity distribution for the two Gaussian peaks. As the covalency of the Cu-O bond increased from $CuYO_2$ to $CuAlO_2$, hybridization between the $3d_z^2$ and 4s orbitals became more prolific with higher Cu-O binding energies. This lifted the non-bonding 3dz2-4s orbital energy in order to compensate for the antibonding $3d_z^2$+4s orbitals. This will increase the excitation energy from $CuAlO_2$ to $CuYO_2$. As a

result, the deconvoluted $CuYO_2$ spectra (denoted as triangle in Figure 31(a)) were shifted to a shorter wavelength. Additionally, the experimental binding energy for $Cu2p_{3/2}$ and Al2p (Figure 31 (b) and (c)) shifts to lower values at higher dopant concentrations (932.5/74.4eV for CAO-0Y, 931.7/73.34eV for CAO-1Y and 930.9/73.21eV for CAO-5Y), indicating a reduced binding energy around O-Cu-O and MO6 after Y intercalation, which is also consistent with the observed blueshift in PL spectra Figure 31 (d) confirms the Y doping into the lattice and the peak intensity increases with the increase of the doping concentration.

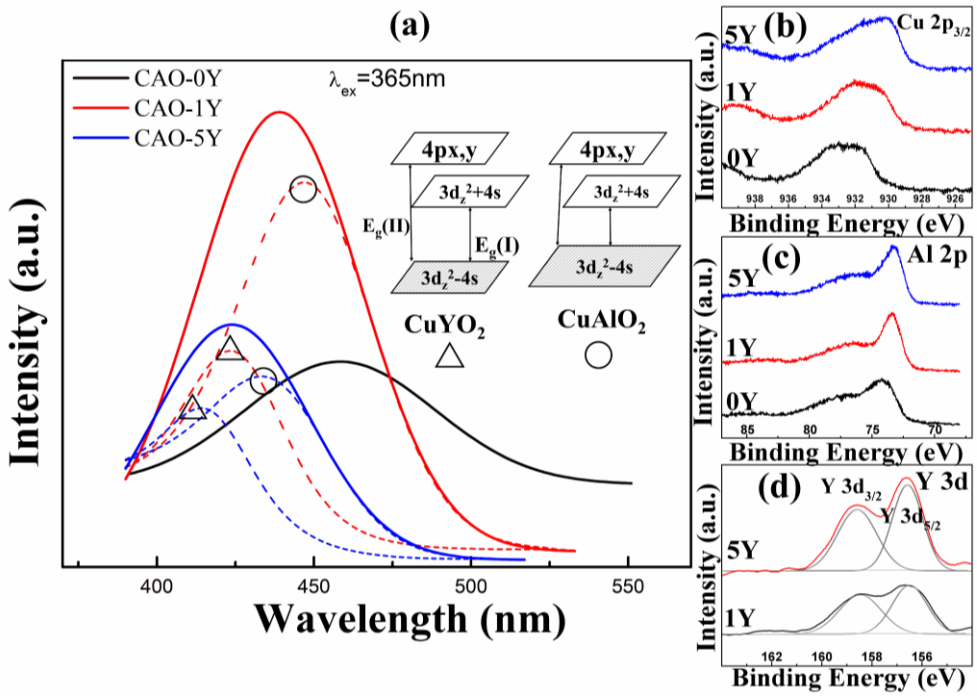

Figure 31. Photoluminescence emission spectra (a) of $CuAlO_2$ nanofibers annealed for 2h (Solid line: experimental observation; dotted line: deconvolution of asymmetric peak due to yttrium intercalation). XPS spectra of Cu 2p (b), Al2p (c) and Y3d (d).

The blueshift in the UV near-band-edge emission is also dependent on the size effect. This band-gap enhancement can be calculated from below:

$$\Delta E = E_g^{nano} - E_g^{bulk} = \frac{h^2}{8\mu^* \rho^2} - \frac{1.8e^2}{4\pi\varepsilon_r \varepsilon_0 \rho} \qquad (13)$$

where represents the band-gap enhancement between bulk materials and nanostructured materials. Other variables include h, or Plank's constant; μ^*, which is the reduced mass of the electrons and holes; ρ the size of the crystallites; e, the electronic charge; ε_r, the relative permittivity and ε_0, the vacuum permittivity of free space. Equation (13) consists of particle-in-a-box quantum localization energy plus Coulomb energy. In order to determine the values on the right-hand-side of the Equation (13), μ^* and ε_r are required for the $CuAlO_2$ electrospun fibers. Therefore, UV-Visible transmittance and diffuse reflectance measurements were performed to estimate the value of the two terms from the transparent oxide samples. In an oxide insulator, the conducting electrons in high frequency ranges (near UV to visible) are dominant and the dielectric constant ε_r is therefore reduced to its real part. The ε_r can be calculated from the following equations:

$$n = \frac{1+\sqrt{R}}{1-\sqrt{R}} \qquad (14)$$

$$\varepsilon_r = n^2 \qquad (15)$$

Here, R is the reflectance data from the UV-visible diffuse reflectance measurement. Figure 32 depicts the results of the optical measurement in the range between 350 to 800nm. The upper limiting boundary value for dielectric constant could be calculated from Equation (15), which is ~2.8 for undoped samples.

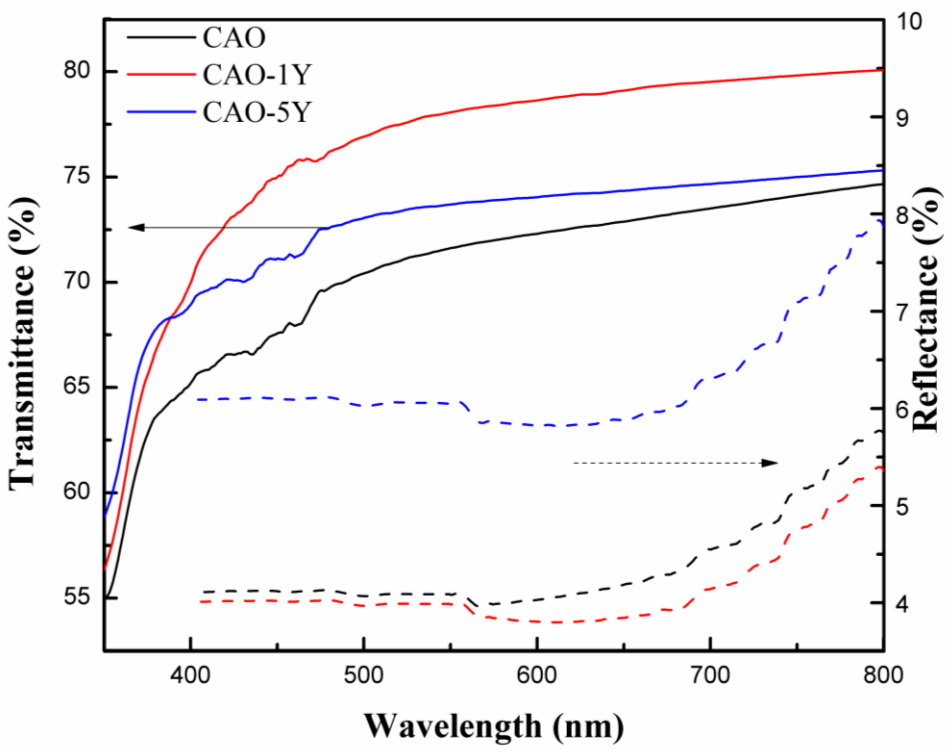

Figure 32. Transmittance and reflectance measurements on the quartz substrate coated with $CuAlO_2$ fibers.

The theoretical value of μ^* can then be estimated with Equation (16) for the hydrogen-model binding energy (Eb) equation:

$$E_b = \frac{\mu^*}{m_0 \varepsilon_r^2} R^\infty \tag{16}$$

where R^∞ is the Rydberg constant (13.6eV) and m_0 is the free electron mass. When considering the room temperature excitation of the thermal energy ~0.025eV as the boundary binding energy, the reduced mass, μ^*, can be estimated to be $0.023\,m_0$ for the undoped sample, $0.016\,m_0$ for the sample with 1% Y^{3+}, and $0.012\,m_0$ for the sample with 5% Y^{3+}. The reduced mass decreases with the increase of Y^{3+} dopant level, which is basically a cause of the decrease of the dielectric constant. Similarly, the XPS indicated a reduced binding energy environment and a weaker localization of excitons in the two-dimensional confinement of Cu-O bonds, which could also lead to reduced mass

decrease. These values can be considered to be the boundary values of the reduced mass for the purposes of Equation (13). By substituting the boundary values of reduced mass μ^* and the dielectric constant ε_r into the Equation (13), the theoretical band-gap enhancement as a function of crystallite size is plotted as solid lines in Figure 33. The degree of band-gap enhancement also corresponds with the blueshift observed in the PL spectra. Further increasing the dopant level would shift the emission spectra to higher energies. Under the assumption of the quantum size effect expressed in Equaiton 4, the experimental data was obtained from the differences between the bulk band-gaps and the PL spectra peak energies. The bulk band gap was measured as the optical direct band gap from the UV diffuse reflectance. The Kubelka-Munk equation was employed to calculate the bulk direct allowed band-gap for the nanofibers. The band-gap energies of the samples with 0%, 1% and 5% Y^{3+} dopant content were found to be 3.26ev, 3.42eV and 3.52eV. The increased band-gap which resulted from the introduction of yttrium is consistent with the theoretical model relating to the excitation energy to various Cu-O bond environments.

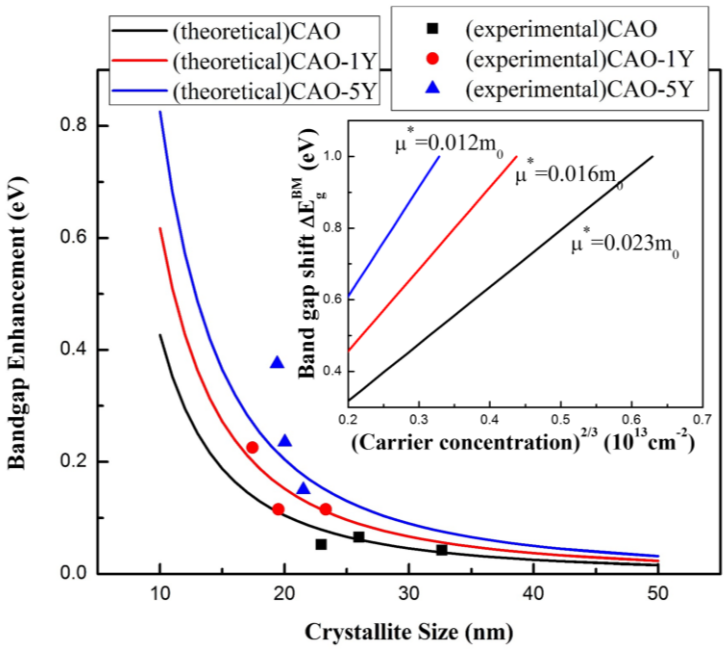

Figure 33. Band-gap enhancement calculation based on theoretical estimation from UV-visible optical properties and the experimental data from both PL spectra and optical band-gap of nanofibers with different crystallite size. Inset plot shows the associated Burstein-Moss effect.

It should be noted that in Figure 33, the band-gap enhancement curves of the three samples which were projected based upon the size effect model did not match up with the experimental data points gathered from those samples at the different crystallite sizes. The undoped sample fit the theoretical curve well for crystallites below a crystallite size of 35nm. This would suggest that band-gap enhancement values could be calculated exclusively from crystallite size. However, when a further blueshift was induced by the $3d^9 4p^1$ to $3d^{10}$ transition in the $CuYO_2$ structure, the experimental data deviated from the quantum confinement estimation. We attribute this shift to the Burstein-Moss effect, which refers to the band gap widening in response to the change of carrier concentrations[107,126]. The Burstein-Moss energy gap shift is shown in the inset of and can be calculated by the following equation:

$$\Delta E_g^{BM} = \frac{h^2}{8\pi^2 \mu^*} \left(3\pi^2 n\right)^{\frac{2}{3}} \tag{17}$$

The carrier concentration in this equation is given by n. Assuming that $CuAlO_2$ and $CuYO_2$ have similar electron density maps[127], then the reduced mass can be the cause of the corresponding Burstein-Moss band-gap enhancement (shown in inset of Figure 33), which exhibits a similar range of enhancement with the fitting discrepancies from quantum size model. The 4d orbitals formed by the Y^{3+} dopant at the lower edge of the conduction band caused the additional band-gap adjustments. The prominent coupling between the reduced mass and the Cu-O distance reveals that hole hopping could be enhanced augmented by the substitution of Y^{3+} into the M^{3+} site.

D. Summary

In conclusion, the room-temperature photoluminescence of $CuAlO_2$ nanofibers was observed having a blueshift at elevated doping levels. A quantum size effect model was also evaluated to probe the fitting discrepancies associated with the yttrium intercalation and the binding energies of the Cu-O bond. The band-gap was further enhanced by the

addition of a trivalent yttrium dopant. This caused a blue shift of the photoluminescence spectra, a phenomenon which has promising potential for the development of blue-violet photoluminescence. This investigation based on PL and optical characterization may provide useful guidance for the dopant enhanced transparent oxides with nanostructures.

LUMINESCENCE OF ELECTROSPUN $CuAlO_2$ FIBERS WITH TRIVALENT ION SUBSTITUTION FOR Al CATIONS

A. Introduction

While most researchers focus on the electrical properties of $CuAlO_2$ as a p-type transparent conducting oxide, there are few reports of $CuAlO_2$ as a potential phosphor material. In addition, with the development of field emission display and other flat display technologies, new generation of phosphors with good luminescence, conductivity and stability are required. $CuAlO_2$ could be a promising host material in which the Al site could be substituted with various trivalent rare earth dopants, without changing the hole transport within the Cu^+ plane [128]. Since the main conduction path in delafossite crystals is close-packed Cu^+ layers[129], the electrical properties could be sustained in addition to photoluminescence properties. Conventional solid-state synthesis of $CuAlO_2$ powders or thin films requires high temperature sintering and repeated thermal treatments. In this study, we prepared $CuAlO_2$ fibers via a cost-effective electrospinning method. The wire-like $CuAlO_2$ nanostructures possess higher surface area and sintering activity, which could lower the annealing temperature. Additionally, the one-dimensional material may also present extraordinary effectiveness in light emitting and transparent conducting [130-132]. The dopant cation, Eu^{3+}, was chosen as the first emission activator and intense red emission from f-f transition of Eu^{3+} was identified. The Eu^{3+} activator center was successfully doped into the Al^{3+} site and this delafossite-type material could be used as potential host for luminescence application. Besides of the down-conversion enabled by Eu^{3+} ions, up-conversion in $CuAlO_2$ host was also achieved, which indicates a suitable host environment for RE^{3+} ions. A tentative study on chemical unit co-substitution was conducted by partially replacing $[Al^{3+}+Al^{3+}]$ with $[Mg^{2+}+Si^{4+}]$ aliovalent ions. The concept of chemical unit co-substitution was recently introduced by Xia and

Poeppelmeier[133,134] in some solid-solution phosphors. The distortion of polyhedral and modified electron-phonon coupling were found to contribute to the continuous control over photoluminescence. As illustrated in Figure 1, the AlO6 octahedral plays critical role as activator host. Therefore it is plausible to tune the PL properties by changing the host environment.

B. Down-conversion in Eu^{3+} doped $CuAlO_2$

The samples preparation follows the procedures described in aforementioned experimental sections. The X-ray diffraction (XRD) patterns together with RWP (residual weight pattern) values from the refinements are shown in Figure 34 along with the standard $CuAlO_2$ ($R\bar{3}m$) phase for comparison. All samples show a single $CuAlO_2$ phase with no other crystal structure identified. This shows that the post annealing condition is sufficient to transform the polymeric as-spun fibers into a single, crystalline delafossite structure. In addition, samples (not shown in Figure 34) with a higher annealing temperature of 1200 °C shows undesired $CuAl_2O_4$ phase due to the oxidation of cuprous ions. Annealing at lower temperatures than 1040 °C, both $CuAlO_2$ and CuO phases result, due to the insufficient reaction between CuO and $CuAl_2O_4$[42,135]. It is noteworthy that crystallinity differs among samples with different Eu doping. Samples with the 0.001 and 0.003 Eu doping show lower degree of crystallinity corresponding to broader diffraction peaks. However, when the doping concentration exceeds 0.01, well-defined $CuAlO_2$ delafossite peaks are exhibited. According to the bonding environment shown later, the substituted Eu and resultant Eu-O bond may alter the bonding environment, allowing for higher mass diffusivity and more sufficient crystallization, which might explain the promotional effect of Eu on $CuAlO_2$ crystallization. In a word, the nanofiber-derived single-phase $CuAlO_2$ via single step annealing and relatively short dwelling time implies that one-dimensional ceramic fibers have higher sintering activity than powders or thinfilms[58].

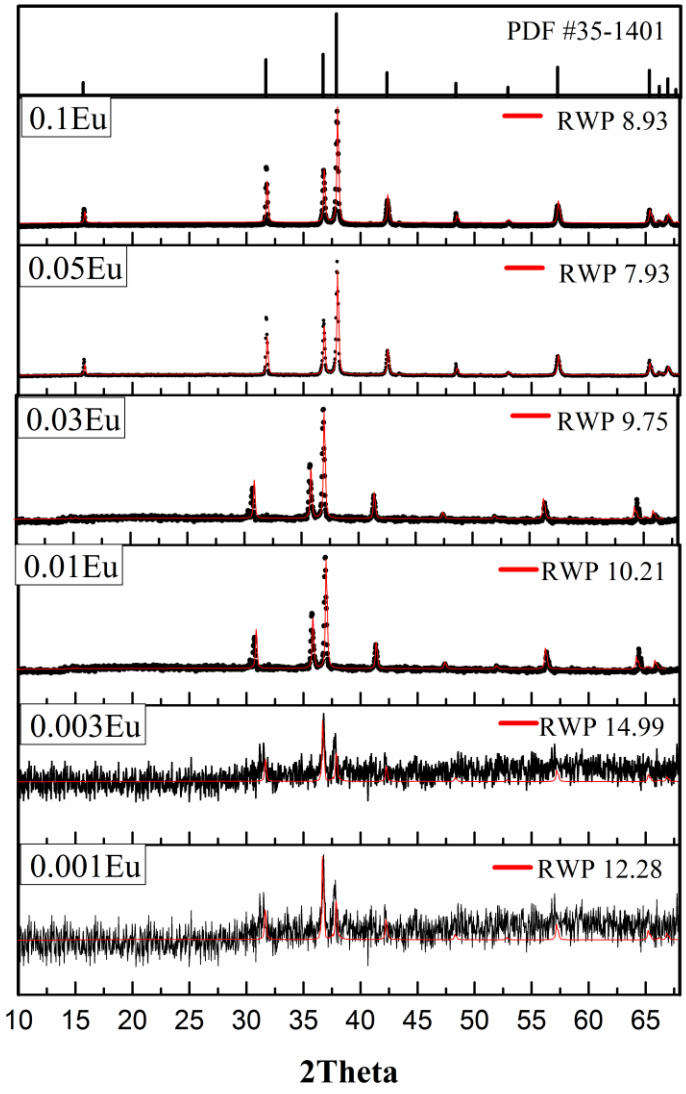

Figure 34. XRD patterns of $CuAl_{1-x}Eu_xO_2$ (x=0.001, 0.003, 0.01, 0.03, 0.05 and 0.1) electrospun fibers annealed at 840°C for 3h, with standard PDF#35-1041corresponding to 3R-polytype delafossite $CuAlO_2$.

The lattice parameters extracted from the Rietveld refinement of the delafossite phase $CuAl_{1-x}Eu_xO_2$ are shown in

Figure 35. The lattice parameter a increases with increasing Eu concentration while c remains nearly constant. This behavior could be explained by a pseudolinear relationship between lattice constant and trivalent ion radius r_R in a delafossite structure [136]. According to our host material, $CuAlO_2$, the lattice constant could be estimated

by $a = 2.784 \times r_R + 1.437$, in which the constant 2.784 was calculated from the a value at zero doping level from the standard powder diffraction file (PDF#35-1401). The trivalent ion radius r_R follows a weighted sum of both Al^{3+} radius and Eu^{3+} radius ($r_R = (1-x)r_{Al} + xr_{Eu}$) [137]. By employing the Vegard's law, the Eu^{3+} ions are assumed to exclusively occupy the Al^{3+} sites, due to their equivalent charge and more difficulties in impurity doping of Cu-O dumbbells with strong covalency between Cu^{+} d^{10} levels and O-2p orbitals. Based on the two equations above, the calculated value is shown as a dashed line in

Figure 35.

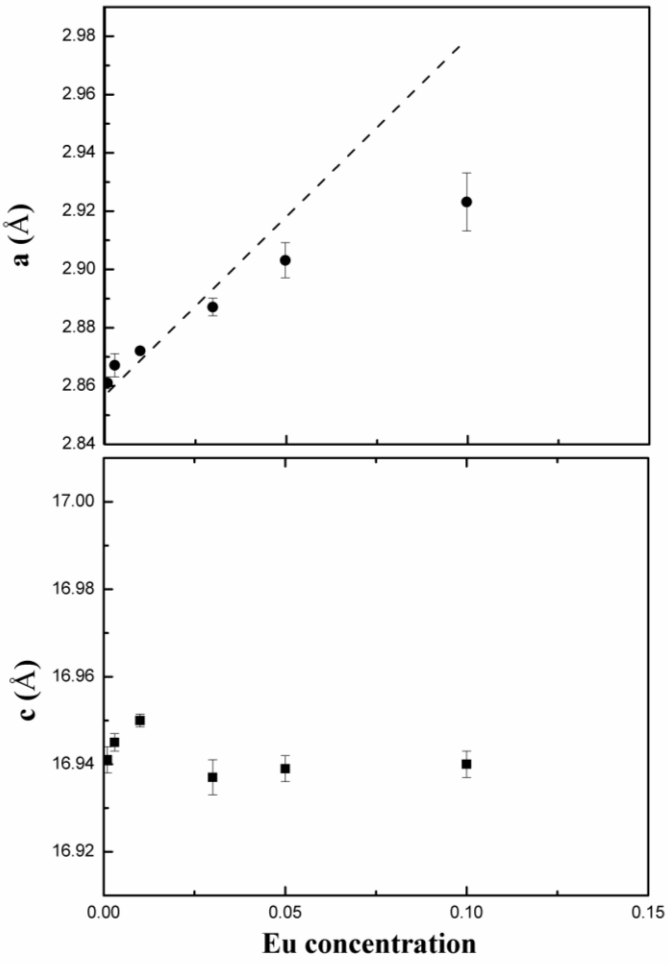

Figure 35. The lattice parameters of a and c of the 3R-polytype structure delafossite $CuAl_{1-x}Eu_xO_2$ as a function of Eu concentration. The dash line shows the respective calculated a values.

It can be seen that both experimental and calculated parameters follow a similar trend as a function of Eu concentration. The deviation could be attributed to the stoichiometric variation in starting precursors and the difference between nominal and doped Eu ion concentrations. The c value is independent of r_R and at various doping levels, the lattice parameter c remains almost constant. The trends in both a and c in terms of dopant concentration imply that Eu^{3+} substitutes Al^{3+} site in this delafossite structure.

The SEM micrographs are shown in Figure 36. After thermal annealing, the smooth polymeric as-spun fibers become coarse and rough, with nano-sized polygonal grains observed on the fibers. The microstructure evolution with the increasing doping concentration is also prominent, from well-sustained non-woven fibers to a disconnected porous structure. According to the significant radius difference between Eu^{3+} and Al^{3+} ions, the introduction of Eu^{3+} in the Al^{3+} site may cause lattice distortions and unrelaxed strains. Additionally, the radial crystallization on self-supported fibers imposes excess surface strain on the crystallites. As a result, excess enthalpy was produced for crystallization and a higher crystallinity is expected with a further increasing in Eu level, in a similar manner revealed from XRD patterns. When the Eu concentration increased with further increase in crystallinity to a degree that the bonding to crystallites cannot hold the accumulated stress in the cylindrical fibrous structure, the non-woven fibers break up and the crystallites start growing as isolated particles.

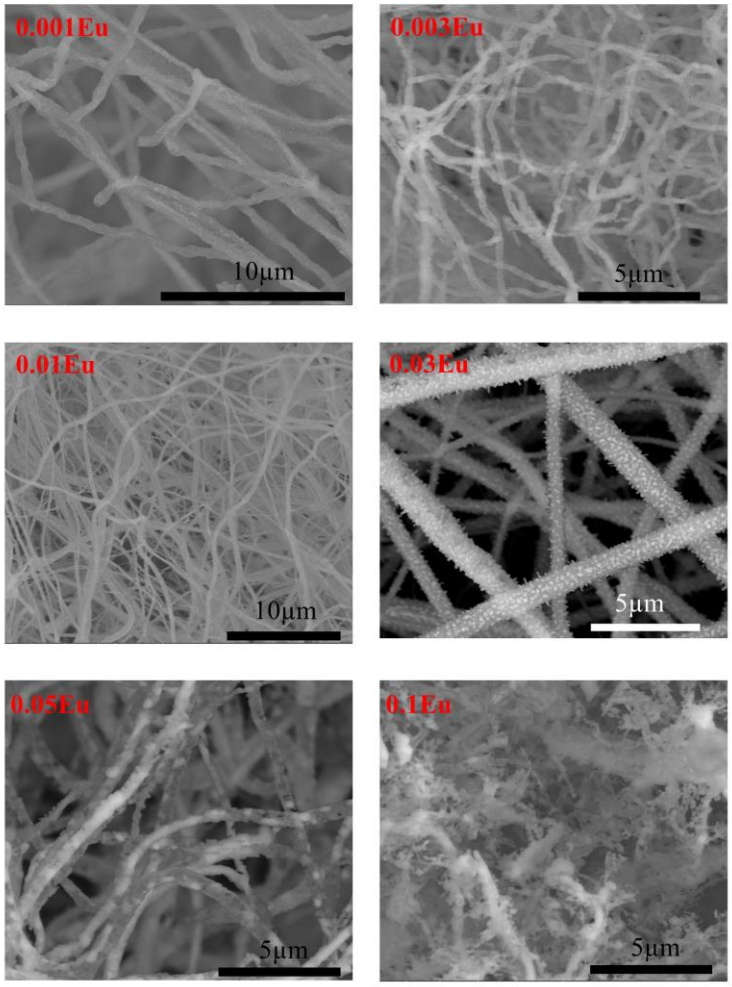

Figure 36. SEM microstructure of $CuAl_{1-x}Eu_xO_2$ (x=0.001, 0.003, 0.01, 0.03, 0.05 and 0.1) electrospun fibers annealed at 840°C for 3h.

During the annealing process of the electrospun fibers, the organics derived from the PVP addition must be eliminated in order to achieve well-crystallized ceramic fibers suitable for luminescence application. EDS was employed to confirm the burn-out of the polymers shown in Figure 37. Before thermal annealing, the energy peaks associated with C and N were prominent because of the existence of PVP ($(C_6H_9NO)_n$). After 1100 °C annealing, there were no C or N peaks identified; only Cu, Al, O, and Eu (enlarged inset in Figure 37) peaks were observed. The polymer burn-out, thermal decomposition and crystallization proceeded simultaneously during the annealing, which shows that this delafossite-type phosphor could be synthesized as one-dimensional fibers.

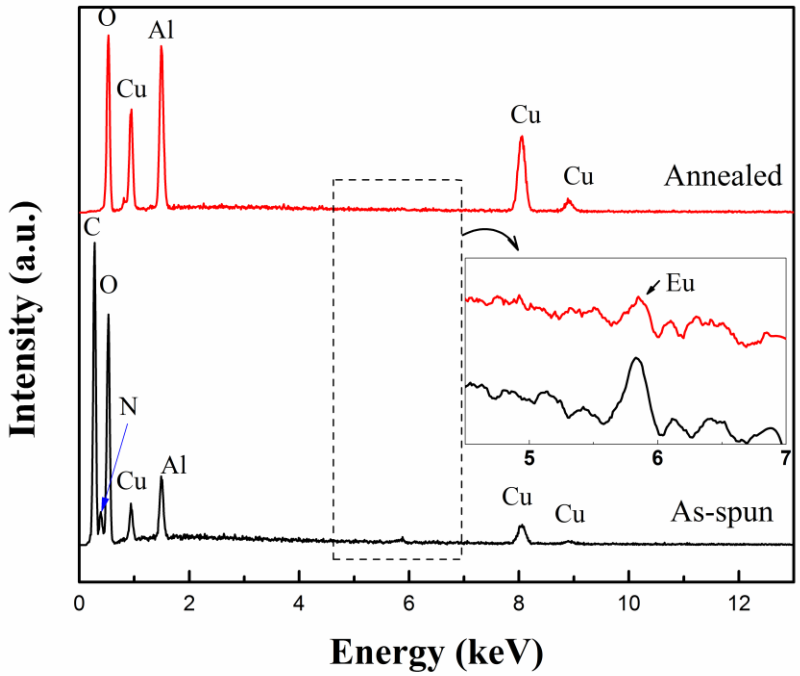

Figure 37. EDS spectra of as-spun polymeric fibers and annealed $CuAl_{0.99}Eu_{0.01}O_2$ ceramic fibers.

The photoluminescence of $CuAl_{1-x}Eu_xO_2$ (x=0.001, 0.003, 0.01, 0.03, 0.05 and 0.1) electrospun fibers have been studied at two excitation wavelengths (365 nm and 420 nm). Delafossite-type $CuMO_2$ has room temperature luminescence due to its UV near-band-edge emissions [99,138-140]. The Cu-O bonds in the O-Cu-O dumbbell layers determine the electronic structure near the band-gap and lead to strong localization of excitons in the x-y plane as well as larger binding energy. This causes hybridization between the $3d_z^2$ and 4s orbitals in the $CuMO_2$ delafossite. Since the binding energy exceeded the room temperature thermal energy (kT≈0.025 eV), room temperature PL emissions were presented [118,119]. We herein reported the room temperature near-band-edge emissions from the Eu-doped $CuAlO_2$ fibers with slightly different peak energies compared to other studies[119,141]. The peak positions in terms of relative intensity shown in Figure 38 mainly centered at ~407 nm, indicating a 0.3 eV decrease in the direct band-gap compared to a normal 370 nm emission in thin films or bulks. Since the reported direct band-gap values of $CuAlO_2$ vary from 3.0 eV to 3.8 eV and highly depend on fabrication method, the

near-band-edge emission is supposed to shift accordingly. The oxygen vacancies, surface defects and crystallinity associated with fabrication methods in low dimensional $CuAlO_2$ thin films or nanoparticles often yield dispersed band-gap values. In his particular study, the peak energy shift is also attributed to a fiber-derived band-gap energy change. A similar phenomenon has been observed in TiO_2 ceramic fibers[142], that band-gap increases with the excess pressure on the fiber circular cross section. The inset in Figure 38 shows the measured optical band gap in our study, the absorption edge (3.084 eV corresponds to ~402nm) of which is similar to the PL peak energy, which lead to the conjecture that the emission with the excitation wavelength of 365nm results from the $CuAlO_2$ near-band-edge transition. We also need to consider other factors regarding to the violet emission. The defect origin from V_{Cu} in the delafossite material is assumed to form an acceptor level above the zero vibrational level[2,45], leading to a Stokes shift in the spectrum. Since our experiments were performed at room temperature and no other peaks associated with Eu^{3+} activators were observed from the emission spectra, the broad violet emission is unlikely from transition to defect levels. Byrne et al.[141] recently observed a coexistence of both a near-band-edge UV emission and a blue emission at ~430 nm at 14.5 K, with almost 100 nm Stokes shift. Revisiting the study by Jacob et al.[47] on $CuYO_2$ and $CuLaO_2$, the prolific hybridization from Cu 4p/3d orbitals and the resultant $3d_z^2$+4s and $3d_z^2$-4s splitting only give rise to an asymmetric and overlapped peak feature rather than large Stokes shift. In addition, the effect of defect states on room temperature excitation still remains unclear, which definitely requires further investigation. The one dimensional fibrous microstructure with major surface defects may also cause a band-gap narrowing in some oxide materials[143]. However, since there have been no reports on the photoluminescence of $CuAlO_2$ in the form of fibers to the best of our knowledge, at the current stage we may conjecture that the decrease in the band-gap associated with lower excitation energy (365 nm in our case) leads to the red shift in the PL emission spectra. At different dopant levels, the band-gap extracted from the PL peak energies in Figure 38 decreases with the increase of Eu level, indicating the further band modifications as a result of trivalent ion substitution and change of degree in Cu 4p/3d hybridization.

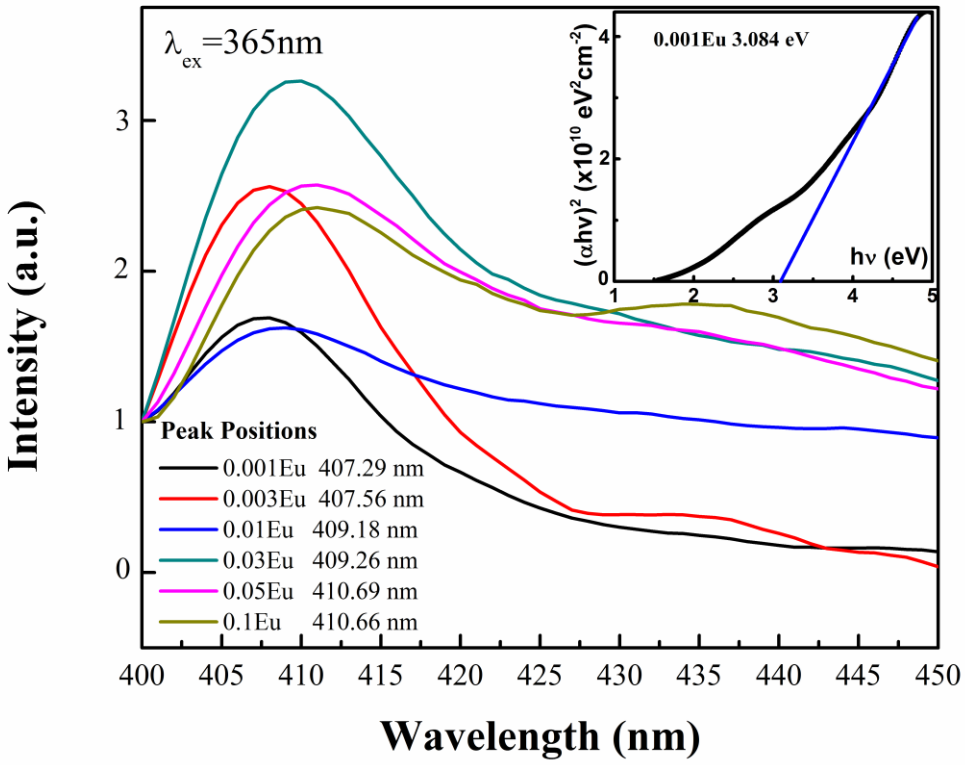

Figure 38. Near-band-edge photoluminescence of $CuAl_{1-x}Eu_xO_2$ excited at 365nm.

We also compared the peak energies in terms of doping levels. Regardless of the variation in relative PL emission intensities, the spectrum shifts to longer wavelength as the doping level goes up, roughly from 407.29 nm in $CuAl_{0.999}Eu_{0.001}O_2$ to 410.66 nm in $CuAl_{0.9}Eu_{0.1}O_2$. Based on the previous study[47,94], this monotonic shift to lower energies is due to the change of hybridization between Cu $4p_{x,y}$ to $3d_z^2 \pm 4s$, under the influence of trivalent partial substitution on Cu-O bond. As the Cu-O covalency increase from $CuAlO_2$ to $CuAl_{1-x}Eu_xO_2$, hybridization between the $3d_z^2$ and 4s orbitals became more prolific which would lift the non-bonding $3d_z^2$-4s orbital energy in order to compensate for the antibonding $3d_z^2$+4s orbitals. Therefore the transition energy between $3d_z^2$-4s and $4p_{x,y}$ is lowered upon introducing Eu^{3+} ions. Our observation also confirmed the prediction that this Stokes shift would increase as the size of trivalent metal ion increases[141]. For all the doped samples at excitation wavelength of 365 nm, only the

broad near-band-edge emission was identified and no peaks associated with Eu f-f transitions were observed above 500 nm. At higher excitation energies, the excitons near the band edge may undergo fast recombination across the band-gap and non-radiative relaxation to the ground state while the transitions to Eu activators become absent.

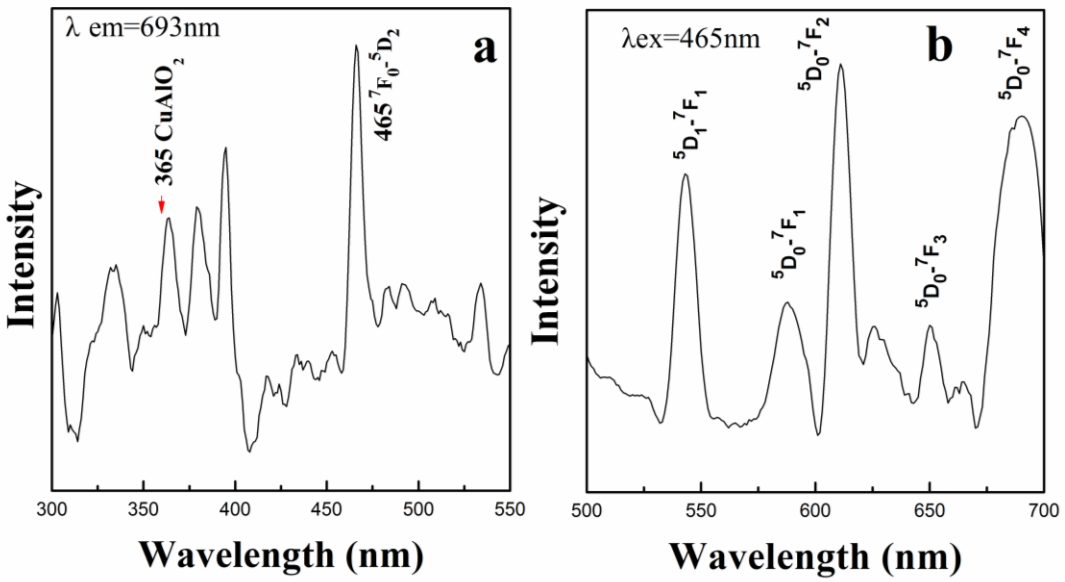

Figure 39. Photoluminescence emission spectra of $CuAl_{1-x}Eu_xO_2$ excited at 420nm, showing the emission bands from Eu^{3+} activator centers.

PL excitation and emission spectra from $CuAl_{0.99}Eu_{0.01}O_2$ are shown in Figure 39. The excitation peaks between 300 and 500 nm correspond to Eu^{3+} intra-4f transitions. The $^7F_0$-$^5D_2$ line at 465nm is the strongest line in the excitation spectrum. The peak at 365 nm was identified as the intrinsic excitation peak from $CuAlO_2$, according to Ahmad's work on $CuAlO_2$ nanoparticles[144] and our previous work on nanofibers[94]. The emission spectrum with 465 nm excitation shows broad bands at 587, 610, 654 and 690 nm, which are due to the f-f transition of $^5D_0 \rightarrow {}^7F_J$ of Eu^{3+}, respectively. For the 0.01Eu sample, $^5D_1 \rightarrow {}^7F_1$ transition was also observed. The two-channel emission diagram is depicted in Figure 40(a). The strongest $^5D_0 \rightarrow {}^7F_2$ red emission is the result of hypersensitive transitions with $\Delta J=2$ indicating the environment around the activator centers. The increasing $^5D_0 \rightarrow {}^7F_2$ emission intensity from samples with x=0.001-0.01 indicates a higher symmetry local site. Upon the occupancy of Eu^{3+} ions in the octahedral center, the

lattice was distorted and the local symmetry of Eu^{3+} continued to change with increasing Eu^{3+} doping level. As a consequence, the probability of each $^5D_0 \rightarrow {}^7F_J$ transition channels may change, which leads to the variation of intensity of the six $^5D_0 \rightarrow {}^7F_2$ emissions shown in Figure 40(b). The overall red emission intensity increases with the increase of doping concentration up to 0.01Eu. Above this doping level, the intensity significantly drops due to the concentration quench effect[19,20] shown in Figure 40(c). With the increase of Eu^{3+} concentration, the cross-relaxation becomes dominant due to the reduced distance between two Eu^{3+} activator ions. Therefore, the luminescence emission intensity almost vanishes at higher Eu^{3+} concentration. Since the activator is introduced solely on the Al^{3+} site, the critical transfer distance (R_c) could be estimated by the following equation:

$$R_c \approx 2\left(\frac{3V}{4\pi x_c N}\right)^{\frac{1}{3}} \qquad (18)$$

where V is the unit cell volume, x_c is the critical concentration and N is the number of Al^{3+} ions per unit cell. For $CuAlO_2$ host (N=3), x_c is roughly equal to 0.01 at which concentration the maximum luminescent intensity was observed. The cell volume from XRD refinement is 120.75 $Å^3$ and the R_c was calculated to be approximately 20 Å. For a Eu^{3+}- Eu^{3+} distance larger than 5 Å, the multipolar interaction is dominant and the exchange interaction is negligible [145]. Therefore, the main mechanism for concentration quenching in the $CuAlO_2$:Eu^{3+} phosphor is the multipolar interaction.

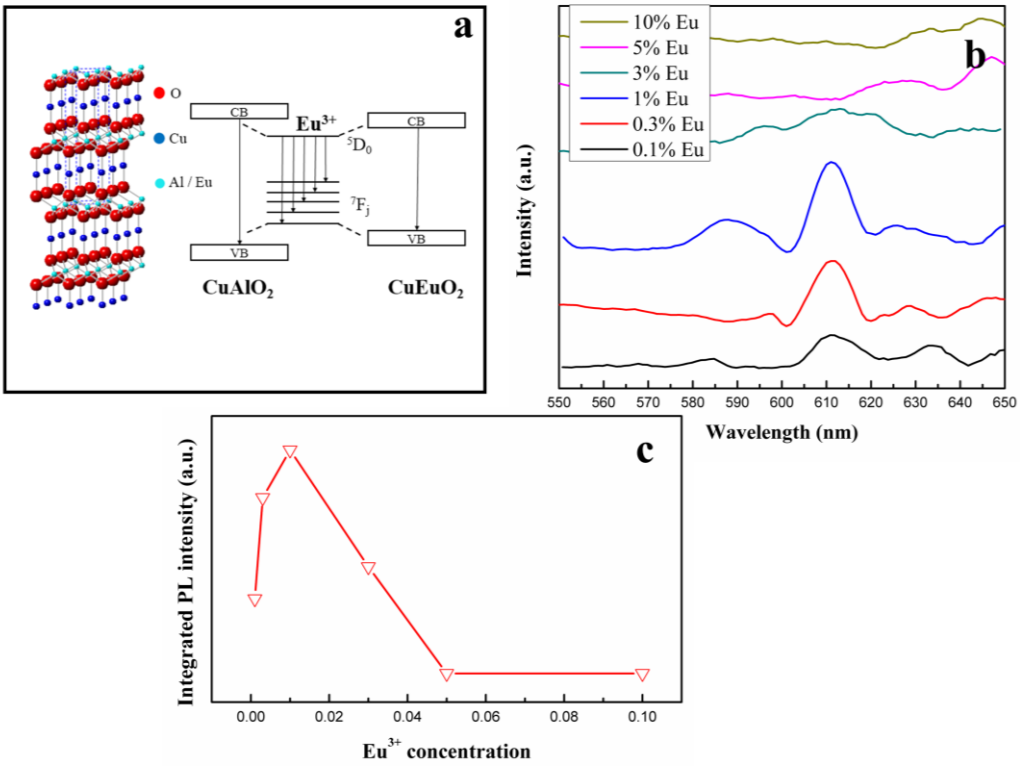

Figure 40. Schematic diagram of photoluminescence emission channels in the rare-earth doped delafossite $CuAlO_2$.

Room temperature Raman spectra are shown in Figure 41. It has been widely acknowledged that in delafossite structure with $\Gamma = A_{1g}+E_g+3A_{2u}+3E_u$, only the first two modes are Raman active.[146,147] The A modes correspond to the vibrational movements in the direction of Cu-O bonds and the E modes represent the vibrations in the perpendicular direction. A previous report on particulate $CuAlO_2$[141] shows two sharp peaks at 418 and 767 cm^{-1}, respectively. However, the Raman scattering peaks could shift to a large extent depending on the trivalent ion species. $CuLaO_2$ with the same crystal geometry has two peaks centered at 300 and 650 cm^{-1}.[148] The lowered frequencies could be due to a higher M atom mass and weaker M-O bond. The room temperature Raman spectrum that we obtained here shows a similar E_g position but a slight lower frequency of A_{1g} mode, which might provide supplementary information on trivalent substitution. Upon the introduction of larger Eu^{3+} ions, the MO_6 along the ab plane would go through a decrease in bonding energy, which is also confirmed by XPS in later discussion. Therefore the E_g

characterized by the vibration along the ab-plane mode should shift to lower frequency. However, from the experimental data, the E_g shows a typical $CuAlO_2$ peak position whereas the A_{1g} peak shifts to lower frequency for both undoped and doped samples, which might lead to the conjecture that the decrease of the A_{1g} frequency might due to the electrospinning synthesis during which the MO_6 octahedral bonding energy is lowered. Another possible explanation for the decrease of A_{1g} mode could be extrapolated from our near-band-edge emission observation. Since the Cu-O covalency is predicted to increase in the doped sample, the higher degree of hybridization might cause the A_{1g} vibration mode to move to lower frequency. In addition, the band width of E_g mode become broader after Eu doping, indicating that the E_g mode is more sensitive to the substitution of trivalent ions.

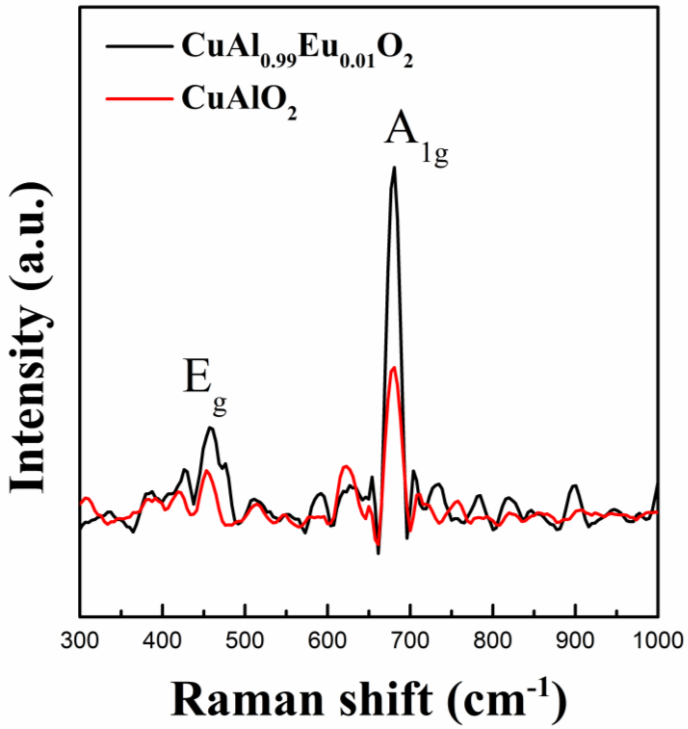

Figure 41. Room temperature Raman spectrum under 1064 nm excitation provided by a Nd:YVO_4 laser.

The binding energies (BE) of the atoms were examined by XPS and calibrated with respect to the C 1s BE (284.6 eV). The XPS high resolution Cu 2p, Al 2p and Eu 4d spectra are shown in Figure 42. The BE for Cu $2p_{3/2}$ is centered at ~933.4 eV for all three

samples with no shift observed with Eu doping. It has been widely acknowledged that in the delafossite structure the strong two-dimensional confinement of Cu-O bonds along the z-axis restrains the electronic structure[118]. Therefore the substitution of Eu^{3+} ions along the ab plane has little effect on the charge density around Cu^{+} ions. For the spectra shown in Fig. 10(b), the peaks can be deconvoluted into Al 2p and Cu 3p components. In contrast to Cu $2p_{3/2}$ peaks, the Al 2p peaks shift to lower binding energies at higher dopant concentrations (74.52 eV for x=0.001, 74.09 eV for x=0.003 and 73.54 eV for x=0.01) due to the environment change around the MO_6 octahedra along the ab plane. The different Cu $2p_{3/2}$ and Al 2p BE responses to trivalent ion substitution leads to the conjecture that the introduced rare earth within the MO_2 layer would insignificantly disturb the hole conduction path in the Cu^{+} layer. Therefore, the p-type conductivity might not be impaired. In Figure 42(c), the presence of Eu 4d spectra indicates the successful doping of europium ions into the delafossite lattice. The trivalent europium compounds with orbit-spin splitting Eu^{3+} $4d_{5/2}$ and Eu^{3+} $4d_{3/2}$ have been shown to have a binding energy of 135 and 142.5 eV[149,150], which is similar to what we observed in our study.

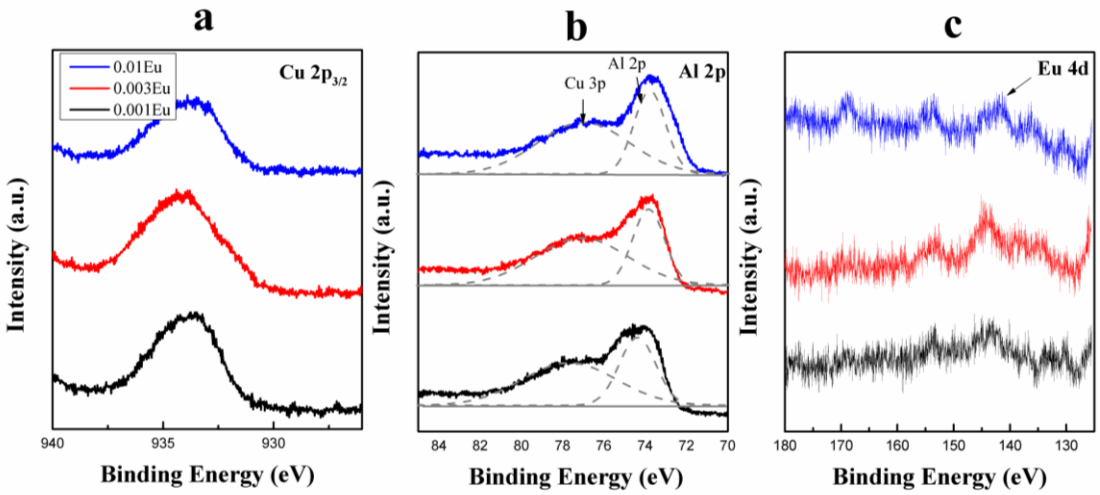

Figure 42. XPS spectra of (a) Cu $2p_{3/2}$, (b) Al 2p, and (c) Eu 4d levels.

The temperature dependence of electrical conductivity of the electrospun fibers is shown in Figure 43. Arrhenius plots were used to identify the thermal-activation type of

these wide band-gap materials. DC current was applied through a piece of fiber mat sandwiched by two rectangular graphite foils, which were used to minimize the contact resistance. The conductivity increases as the temperature increases, showing semiconduction. At ~300 K, the electrical conductivity for 0.1% Eu doped $CuAlO_2$ fibers is ~0.05 S cm^{-1} with a thermal activation energy of ~0.09 eV. The room temperature conductivity increased with elevated Eu doping levels, from 0.05 S cm^{-1} to 0.17 S cm^{-1}. This could be attributed to the substitution of Eu cations which induced the lattice distortion and increased the hole concentrations. On the other hand, the substitution of Eu on the Al site may introduce a smaller band-gap associated with $CuEuO_2$ and this modification at the near-band-edge may also contribute to the hole conductivity enhancement. Based on the plot shown in Fig. 11, when the doping level is as small as 0.1%, logσ decreases linearly with the reciprocal of temperature. However as the doping concentration increased, a variable-range hopping mechanism occurred [151], which could be seen from the segmented slopes at different temperature ranges. The slope at higher temperature range between 570 K and 800 K is lower than that at a lower temperature range between 300 and 400 K. A revisit to PL energy peaks shown Fig. 6 could lead to the conjecture that the change in thermal activation may result from the various band-gaps induced by Eu partial substitution, since the band-gaps decreases with the increase of Eu concentration. In addition to the DC temperature-dependent conductivity measurement, the Hall coefficient shown in Table VI shows a p-type semiconductivity.

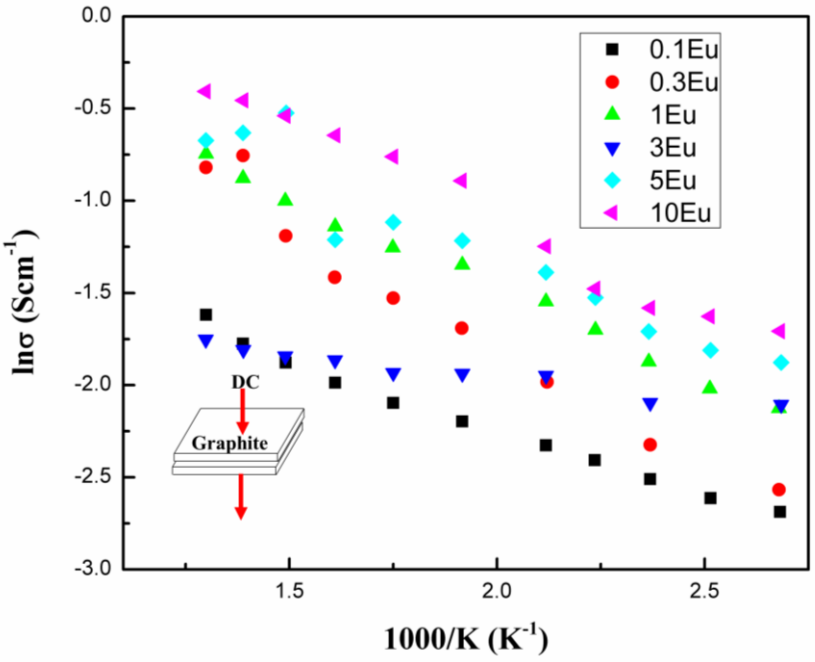

Figure 43. Arrhenius plots of DC electrical conductivity in $CuAlO_2$ fibers.

Table VI. Hall-effect Measurements of Eu-doped Samples.

Sample	R_H (cm^3/C)	Density (cm^{-3})
$CuAl_{0.999}Eu_{0.001}O_2$	+5.48	1.14×10^{18}
$CuAl_{0.9}Eu_{0.1}O_2$	+6.94	8.99×10^{17}

C. Photoluminescence of $CuAlO_2$ doped with selected trilavent ions

Figure 44 records the excitation and emission spectra of the sample doped with Yb^{3+}. The samples of CAO: 0.1at% Yb^{3+} and CAO:1at% Yb^{3+} showed typical Yb 4f emission under the excitation wavelength of 286nm. From the excitation spectra, which centered at around 284nm, are due to the transfer from $CuAlO_2$ host (O^{2-} 2p levels) to Yb ions. Since this transfer is dominant in intensity, it shadowed the excitation peak of the intrinsic $CuAlO_2$ which normally centered at ~360nm (shown as the shoulder peak in the low level doped samples). From literature, the Yb doped nanophosphors (not used as optical fibers or lasers) excited in the UV region could exhibit obvious cooperative energy transfer via dipole-dipole interaction. Since pure $CuAlO_2$ has a UV emission, which has just twice of the energy required for f-f transition of Yb ions. Therefore, it is possible for this

cooperative energy transfer to occur from the host to Yb ions, thus overriding the violet emission of $CuAlO_2$ itself.

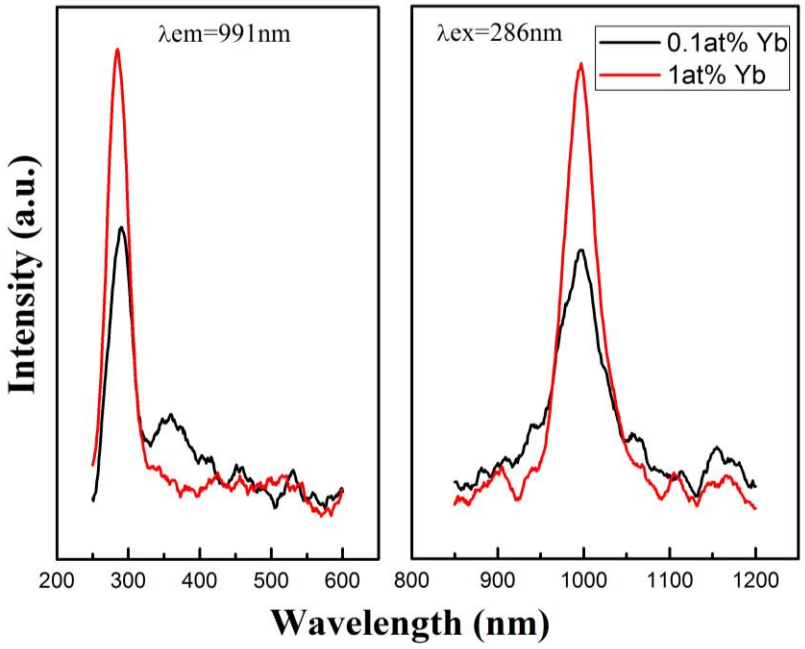

Figure 44. PLE(left) and PL(right) spectra of Yb:$CuAlO_2$ nanofibers.

Er^{3+} is generally used to provide transition channels for up-conversion luminescence, in which lower excitation photon energy is converted to higher emission energies. Figure 45 presents the up-conversion PL spectrum with 980 laser excitation. A broad green emission peak is identified in the $CuAlO_2$ host material. Additionally, there is no prominent difference between the Er^{3+} doped and Yb^{3+}-sensation sample.

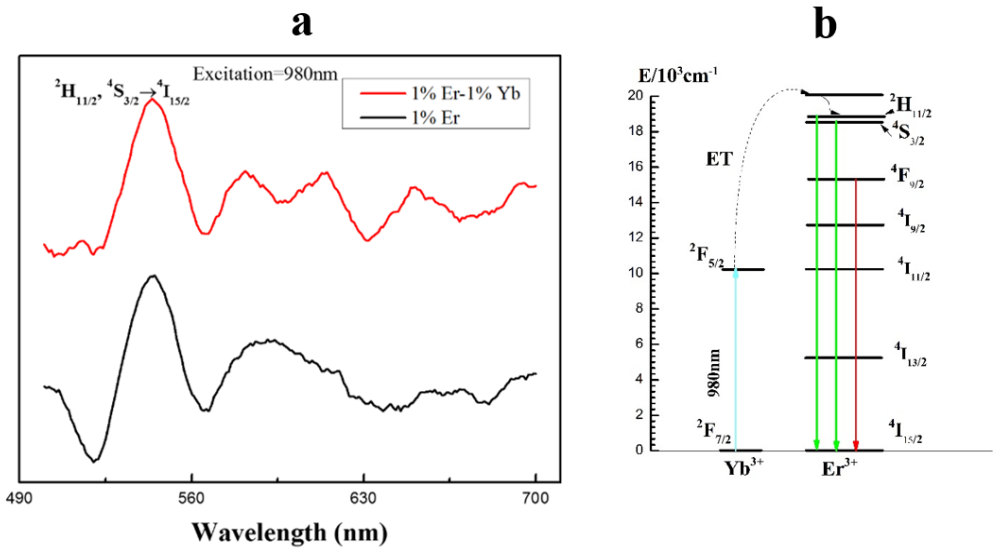

Figure 45. Figure 4.5. (a)Up-conversion luminescence spectra of Er^{3+} doped and Er^{3+}-Yb^{3+} co-doped $CuAlO_2$ and (b) energy level diagram energy level diagram: up-headed cyan solid arrow indicates pump at 980 nm into $^2F_{5/2}$ level of Yb^{3+} and $^4I_{11/2}$ level of Er^{3+}. Down-headed solid lines indicate three different up-conversion mechanisms based on energy transfer from Yb^{3+} to Er^{3+}, giving rise to the strong green (545 nm, 595nm) and week red (660 nm) emissions in (a), respectively.

The mono-trivalent partial substitution for Al site could introduce new photoluminescence functionality which overshadows the original band-transition from monolithic $CuAlO_2$. Some RE ions, such as Eu^{3+}, are sensitive to host environment and thus could be used as crystal field probe[152-156]. In this study, a novel concept of chemical unit co-substitution was utilized by regarding AlO6 as a chemical cage. This idea has recently been realized in several solid-solution phosphors with Eu doping[157,158]. The charge compensation could be written as $[Al^{3+}+Al^{3+}]\rightarrow[Mg^{2+}+Si^{4+}]$, in which regime the new AlO6 after co-doping consists of MgO6 and SiO6 octahedras. The MgO6 and SiO6 also serve as important luminescence host in other crystal structures, such as oxyapatite[159,160] and pervoskites[161-163], which emit tunable luminescence.

Figure 46 summarized the $CuAlO_2$ nanofibers with different Si-Mg concentrations. Pure 3R phase could be maintained with 10 at.% Al substituted by Mg and Si ions. At higher doping concentrations, CuO and silicates products were formed instead of

delafossite. Since the sum of ionic radii of [Mg^{2+}+Si^{4+}] (CN=6) is much larger than that of the [Al^{3+}+Al^{3+}], the AlO6 unit could only withstand a relatively low concentration of aliovalent ions.[31,164] The saturation amount is determined to be ~10 at.%, after which multi phases occur. The lattice parameter a before the phase separation is plotted in Figure 47. Followed a similar trend of monotonic increase as discerned in

Figure 35, the partial co-substitution results in the expansion of the cell.

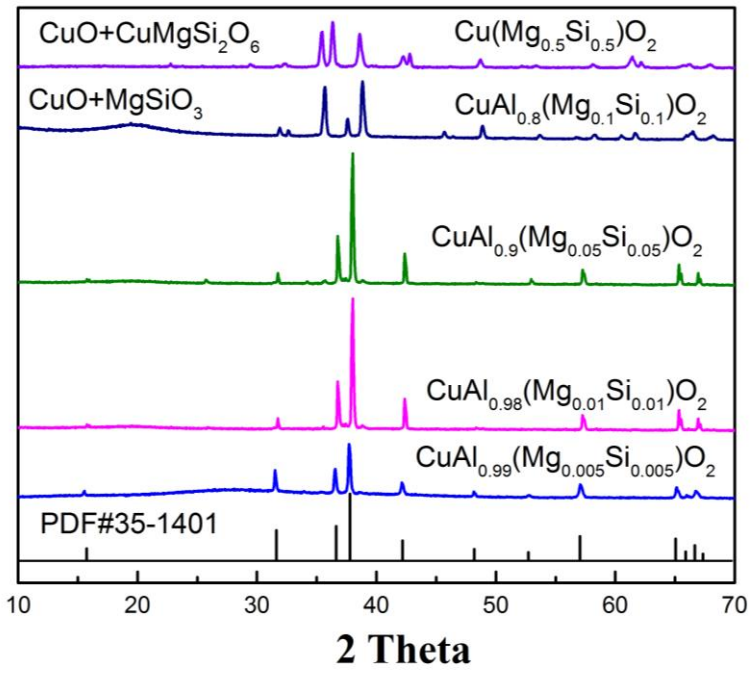

Figure 46. XRD patterns of Cu[Al^{3+}+Al^{3+}][Mg^{2+}+Si^{4+}]O_2 nanofibers.

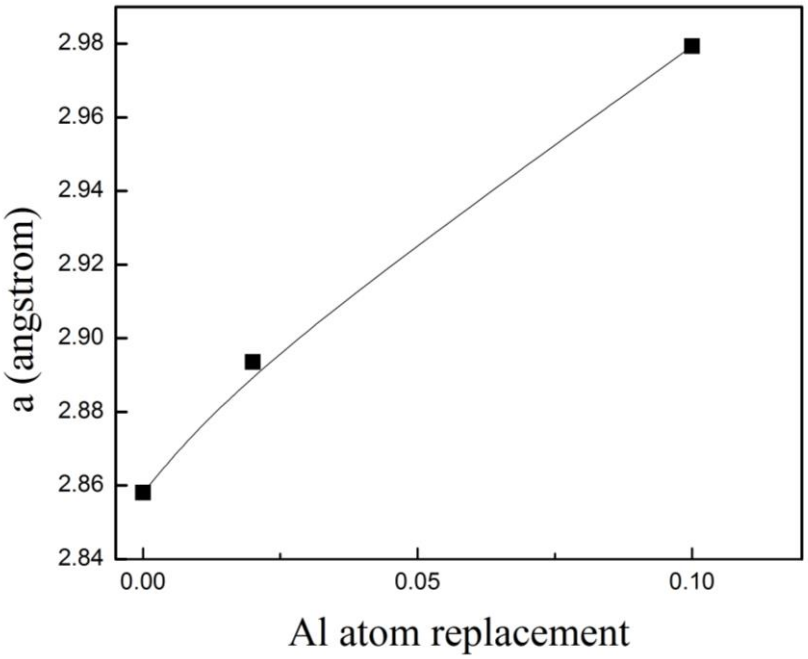

Figure 47. Dependence of the measured lattice constant a on atomic percentage of Al atom replaced by Si^{4+} and Mg^{2+}.

The lattice change in the AlO6 octahedral also leads to a change in ligand field, which is supported by photoluminescence spectra in the Eu doped samples. Figure 48 depicts the characteristic Eu excitation and emission bands from $Cu[Al^{3+}+Al^{3+}][Mg^{2+}+Si^{4+}]O_2$ host. Strong emission centered at 700nm was observed and no emission peaks under 650nm were observed. Compared to the $CuAlO_2$ host, the AlO6 unit co-substitution results in a single band transition from $^5D_0 \rightarrow {}^7F_4$, a switch from red to deep red. Since the Eu activator is sensitive to crystal field, it could be postulated that the electronic and magnetic dipole associated with other $^5D_0 \rightarrow {}^7F_J$ transitions are forbidden as the host environment changes. The current results also show the potential of tuning the PL emission in $CuAlO_2$ towards lower energies towards the near-infrared region. When all the Al sites were substituted by Mg and Si ions, no luminescence is detected in the visible range, probably due to the absence of delafossite phase. There has been no reports on RE doped CuO and $CuMgSi_2O_6$, therefore it is highly possible that the Eu 5D-7F transitions are not allowed in those crystals.

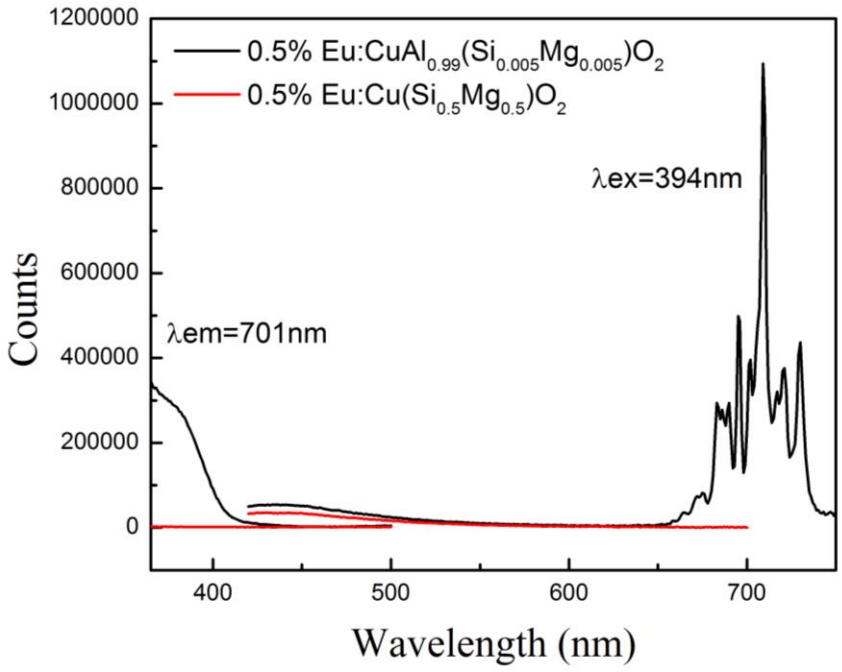

Figure 48. PLE and PL spectra of 0.5at% Eu:$CuAl_{0.99}(Si_{0.005}Mg_{0.005})O_2$ and 0.5at% Eu:$Cu(Si_{0.5}Mg_{0.5})O_2$ at monitoring wavelength of 701nm and excitation wavelength of 394nm.

Upon introducing the co-dopant, the original UV near-band-gap emission is also examined in Figure 49. As the doping concentration increases, the PL intensity drastically decreases. Looking back into the PL shift in the visible region, the excitation spectra shows a broad half peak below 400nm, corresponding to the Eu 701nm emission, which corroborates the UV absorption of MO6 host. The decreased PL with increased Mg and Si may indicate the absorption in (Mg/Si)O6. As a consequence, the energy transfers from (Mg/Si)O6 rather than the AlO6, leading to a further change in visible emission. Moreover, when compared to the previous Y and Eu doped specimens, there is an evident blue shift in the co-dopant scenarios. Considering the same preparation conditions, the increased emission energy is due to the change of AlO6 octahedral. The shifted near-band-edge emission, indicative of direct transition from valance band to conduction band, may imply that the band gap increases with the presence of (Mg/Si)O6 octahedras.

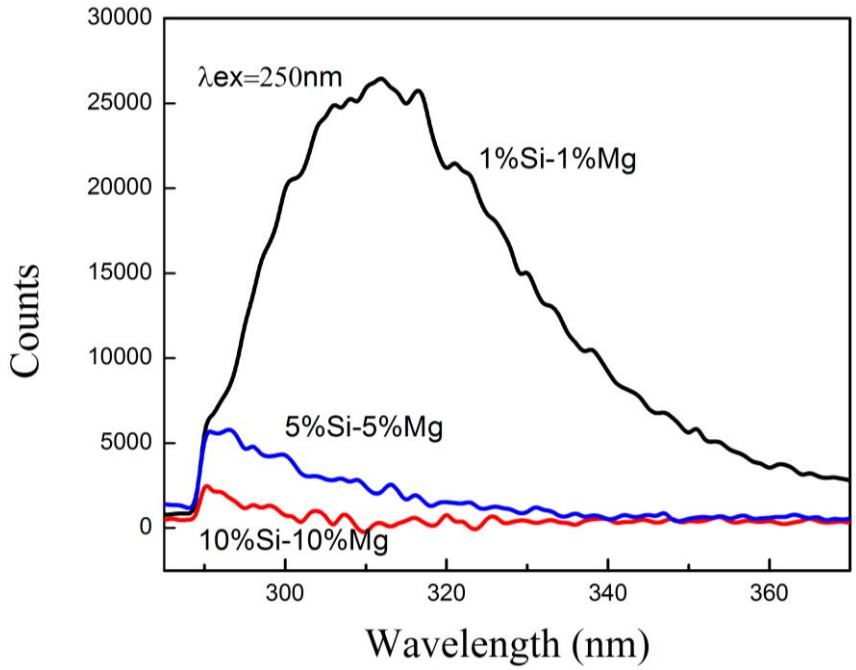

Figure 49. PL spectra in the UV region under excitation of 250nm.

D. Summary

$CuAl_{1-x}Eu_xO_2$ (x=0.001, 0.003, 0.01, 0.03, 0.05 and 0.1) fibers have been fabricated through a combination of a chemical solution method and electrospinning technique. This method could effectively synthesize single-phase $CuAlO_2$ via one-step annealing in air. The lattice parameter a follows a pseudolinear relationship with Eu concentration while the lattice parameter c remains almost constant with Eu concentrations. This implied that the delafossite-type $CuAlO_2$ could be used as a potential host material for the rare-earth Eu^{3+} partial substitution on trivalent site. Further photoluminescence measurements indicated that upon two excitation wavelengths of 390 nm and 465 nm, the $CuAl_{1-x}Eu_xO_2$ exhibits two emission behaviors from both intrinsic near-band-edge violet emission and Eu^{3+} $^5D_0 \rightarrow {}^7F_J$ red emission, which shows that this material might be versatile in multi-channel light emitting. All fibers show semiconducting behavior as a function of temperature, and the room temperature conductivity increased monotonically with an increase of Eu concentration. The variation in thermal activation energy as a result of Eu substitution indicates different hopping mechanisms occurs at inhomogeneous near-band-

edges in the Eu doped delafossite structure. Further study on other selected RE ions corroborates the versatility of the AlO6 structure hosting luminescent activators. A tuned deep red emission is acknowledged with partially replacing AlO6 with (Si/Mg)O6. However, the luminescence drastically disappears at high Si^{4+}-Mg^{2+} concentrations, as a result of phase separation and non-luminescence features of CuO and $CuMgSi_2O_6$. There is also a strong absorption in (Si/Mg)O6 host, which is attributed to the change of Eu^{3+} 5d-7f transition energy.

STATELLITE PROJECT: BULK $CuAlO_2$ REACTIVE SYNTHESIS BY SPARK PLASMA SINTERING AND PRESSURELESS ELECTRIC-FIELD ASSISTED SINTERING

A. Introduction

The p-type $CuAlO_2$ with synergistical conductivity and optical transmittance has been so far studied in low dimensions such as thin films in optoelectronic applications. Even though this transparent conducting oxide has fair performance comparing to n-type TCOs, it shows great potential in some other emerging technologies, such as thermoelectrics[7], electrodes[165] and phosphors[94], where the bulk $CuAlO_2$ could be used. The delafossite-structured $CuAlO_2$ with an anisotropic conductivity within the Cu-Cu basal plan[129] is highly favorable for those applications during the scale-up processing and the host lattice could accommodate multivalent ions, making it a good candidate for functional building blocks. Besides the poor conductivity 10^3–10^4 times lower than that of n-type TCOs for the hole localization of anion oxides[166], the conductivity for the p-type $CuAlO_2$ highly depends on the processing procedures in practice. The plausible reasons might lie in the fact that the nonstoichiometric O defect dominating the hole carrier conductivity is sensitive to oxygen partial pressure and the as-synthesized $CuAlO_2$ powders are not phase pure. Commonly used techniques to fabricate the $CuAlO_2$ compound often involve high temperature solid-state reaction, reduced atmosphere or repeated heat treatment. Based on the thermodynamic rule, the $CuAlO_2$ is metastable below 1000ºC in ambient atmosphere whereas a stable spinel $CuAlO_4$ could be formed at the temperature range of 625 to 1000ºC. Practical techniques often reduce the oxygen partial pressure to reduce the reaction temperature, yet still requires long processing time to form stable delafossite phase.

We herein report a rapid synthesis of $CuAlO_2$ under the electrical field by using the spark plasma sintering and homemade field-assisted furnace. The formation of $CuAlO_2$ phase is observed in both low vacuum and ambient atmosphere. The applied electric field could lower the synthesis temperature significantly regardless of oxygen partial pressure based on the Ellingham diagram[139,167]. The as-sintered bulk $CuAlO_2$ exhibit enhanced

conductivity in contrast to nanopowders and the photoluminescence spectra was further employed to examine phase purity.

B. Results and discussion

Stoichiometric commercial Al_2O_3 (Sigma-Aldrich, 99%, <50nm) and CuO (American Elements, 99.9%, <30nm) powders were ball milled in ethanol. The dried mixed powders were examined by TG/DTA (TA instruments, Q600) in both air and nitrogen atmosphere at a heating rate of 10ºC/min. As shown in Fig. 1a, the weight stabilized beyond 300ºC in air after desorption of H_2O and CO_2, followed by a steady increase after 800ºC. This could be due to oxidation of unstable $CuAlO_2$ by the following equation:

$$4CuAlO_2 + O_2 \rightarrow 2CuO + 2CuAl_2O_4 \qquad (19)$$

According to the phase equilibria in the system of Cu_2O-CuO-Al_2O_3[135], the $CuAlO_4$ and CuO phases containing Cu(II) are stable at the temperature range of 625 to 1000ºC whereas the delafossite $CuAlO_2$ is a metastable phase below 1000ºC. At the temperature above 1000ºC, a sudden mass decrease was observed corresponding to a sharp endothermic peak. Following chemical reaction could be proposed:

$$CuO + CuAl_2O_4 \leftrightarrow 2CuAlO_2 + (1/2)O_2 \qquad (20)$$

When heated in flowing nitrogen, the oxygen partial pressure was reduced to ~10^{-4}atm compared to ~0.2atm in air and the chemical reaction temperature for $CuAlO_2$ could be reduced. As a result, the onset temperature in Figure 50(b) for the major weight loss began at 900ºC for reaction. There is also a slight mass decrease at 600ºC, which may indicate the reduction of CuO into Cu_2O and the Cu_2O could later react with Al_2O_3 to form $CuAlO_2$ directly. By reviewing the thermogravimetric behavior of heating CuO-Al_2O_3 mixed oxides in both air and nitrogen, the kinetic stability of $CuAlO_2$ formation could be estimated based on the reaction ratio α (mass change divided by saturation mass). The α equals to 1-exp(-kt) therefore the rate constant k could be calculated based on time and reaction ratio. From Figure 50(c), it could be seen that the activation energy in air represented by the slope is slightly higher than that in nitrogen. It could be concluded that the solid-state reaction of $CuAlO_2$ could be achieved in either air or

nitrogen and the formation temperature also indicates the minimum thermal requirements reported in current $CuAlO_2$ literatures.

The multi-step thermodynamic formation and multiphase during solid state reaction may give rise to phase purity issues and long dwelling time. In addition, the low oxygen partial pressure may also increase the processing complexity and affect the thermal stability. This may pose less challenges for thin film fabrication. However, for bulk $CuAlO_2$ synthesis, it is necessary to ease the complexities during solid state reaction. The effect of applied electric field during ceramic sintering has been studied in many aspects, ranging from sintering morphologies, phase formation to sintering kinetics. Most of the thermodynamic studies on $CuAlO_2$ and other delafossites often use oxygen partial pressure as a crucial variable to determine the critical transformation temperatures. The applied electric field and related electric effects may modify the kinetics and should therefore be investigated when considering bulk $CuAlO_2$ fabrication. In addition, any tunable properties enabled by electric field may also shed new light on the current p-type TCO study.

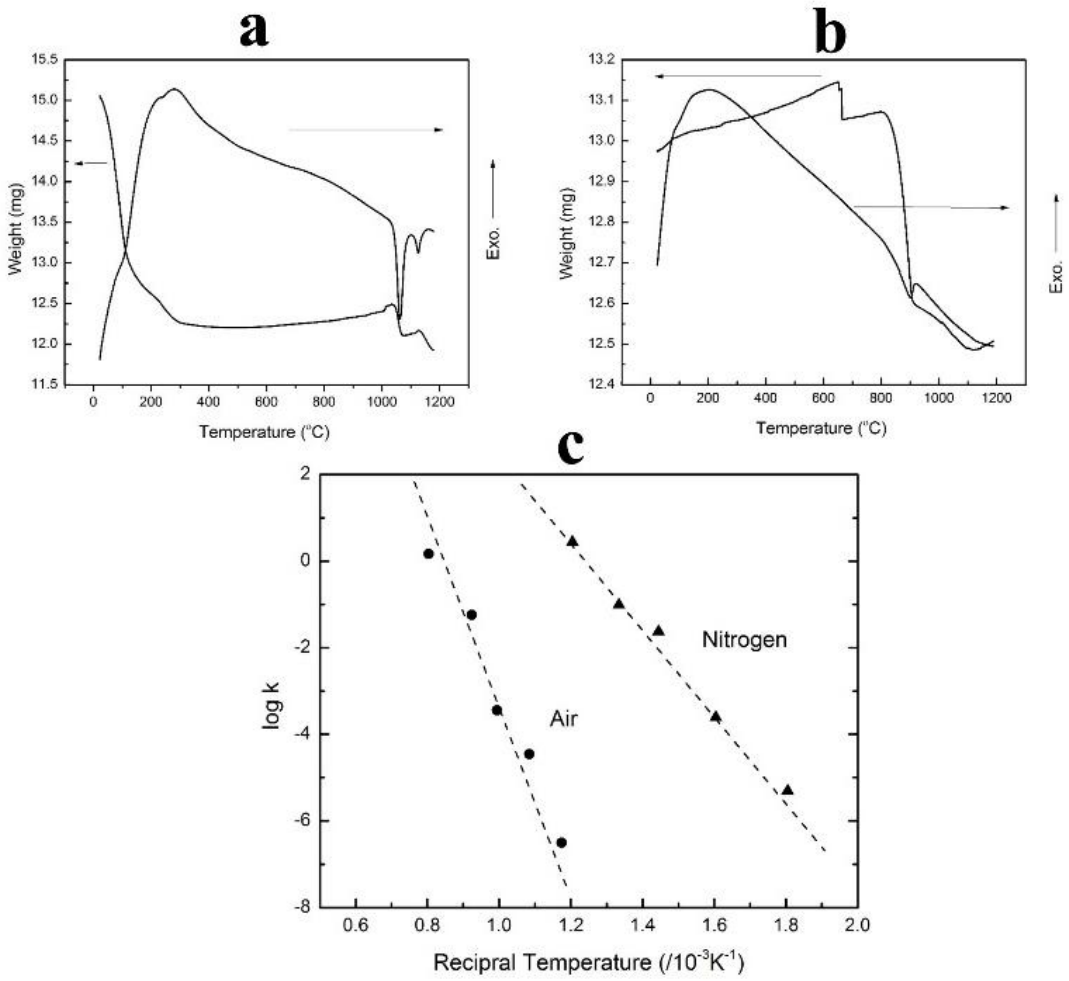

Figure 50. Thermogravimetric diagrams of heating CuO-Al_2O_3 powders in both air (a) and nitrogen (b), with Arrhenius plot of rate constant k as a function of temperature based on reaction (4).

Spark plasma sintering (SPS, FCT Systeme GmbH) was used to provide high DC current and low voltage under a low vacuum condition (7×10^{-2} torr). The low vacuum is believed to lower the synthesis temperature for $CuAlO_2$ according to previous TG/DTA tests. Even though the SPS is inherently favorable for fabricating $CuAlO_2$, there have been few reports on synthesizing or sintering $CuAlO_2$ by SPS or under an electric field. In order to better examine the effect of electric field, a homemade field-assisted annealing (FAA) furnace was used in which two Pt electrodes were inserted into a tube furnace with two ends applied on the two sides of the cold-pressed pellets. In this case, there are no pressure and vacuuming so the sintering could be performed in ambient atmosphere. A

low voltage of 50V and high voltage of 2kV were applied respectively to generate different DC electric field. During the course of studying reactive synthesis under electric field, the sinterability and phase stability of pure $CuAlO_2$ compound were also investigated, as shown in the XRD patterns from Figure 51(a). It is noteworthy that even though the as-synthesized $CuAlO_2$ is thermal stable upon heating cycles to high temperatures, it becomes unstable at the present of electric field, in both SPS and FAA scenarios. The $CuAlO_2$ powders used in this study were prepared by a sol-gel method[107]. The redox of Cu is severe when sintered by SPS and a total decomposition into Cu and Al_2O_3 occurred at a temperature of 1050ºC as shown in Figure 51(a). The powder remained unsintered at temperatures below 800ºC. Therefore, the consolidation of $CuAlO_2$ by SPS is not feasible even at low vacuum levels. For the field-assisted annealing (FAA) and sintering in ambient atmosphere without pressure, decomposition was also observed with resultants the same as that from the reverse reaction of (20). Even though the oxygen partial pressure in this case is high, making the reverse reaction likely to happen, the $CuAlO_2$ and Cu(I) are more stable at high temperatures above 1000ºC. One of the major difference between SPS and FAA is the plasma discharge within the particles at low temperatures prior to sintering and this may lead to Cu redox and melting at grain interfaces, which could explain the phase configurations of $CuAlO_2$ sample sintered by SPS. The FAA on the other hand, could also exhibit large electric field with space charge and higher activation energies at interfaces and grain boundaries. Previous studies[168,169] on electric-field assisted sintering also observed the high surface energies and local melting at intermediate electric field, especially for smaller particles. As a consequence, the presence of CuO might also partially result from the oxidation of Cu after elimination of the interfaces and gaps during coarsening and sintering.

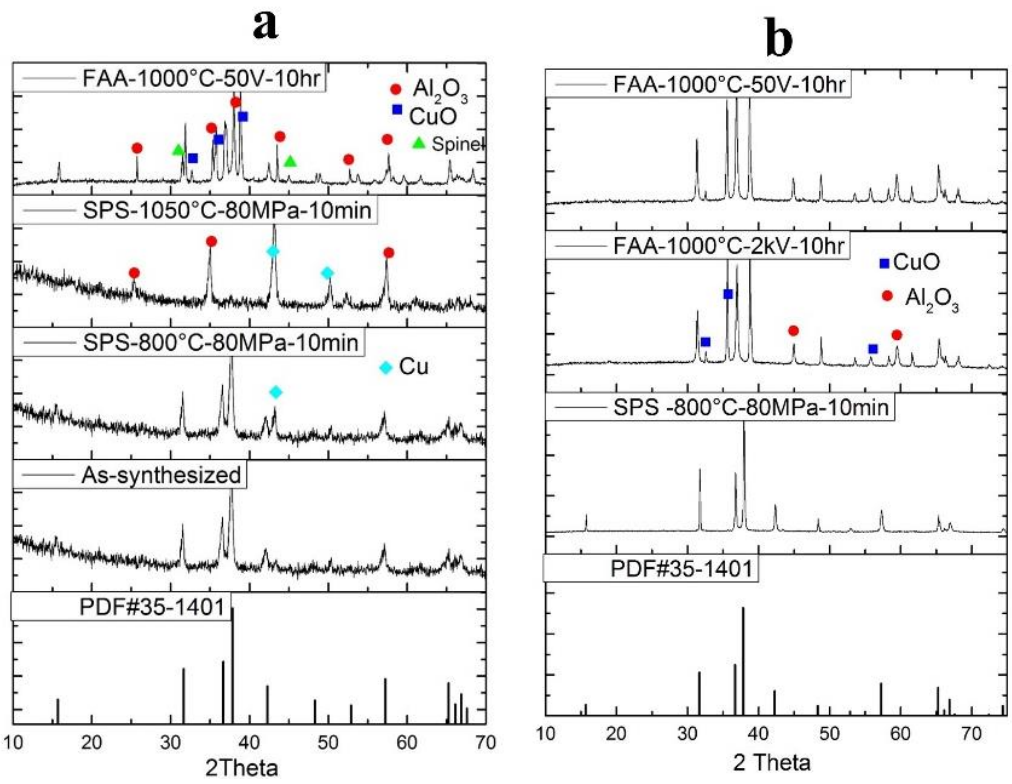

Figure 51. XRD patters after sintering by SPS and FAA, with two different starting powders: (a) As-synthesized $CuAlO_2$ and (b) CuO-Al_2O_3 mixed powders.

Given the difficulties of consolidating $CuAlO_2$ particles, CuO-Al_2O_3 mixed powders could be an alternative providing oxide powder beds to avoid redox and shortened the overall preparation procedures. As shown in Figure 51(b), pure delafossite $CuAlO_2$ could be synthesized and sintered simultaneously through SPS at 800ºC for only 10min under 80MPA. In comparison to the TG/DTA curves in flowing nitrogen with lower oxygen partial pressure, the onset $CuAlO_2$ forming temperature in SPS is even lower. Even in the case of FAA samples processed in air, the $CuAlO_2$ could be formed at a temperature 50ºC lower than that indicated in the TG/DTA curves. There are also some CuO and Al_2O_3 yet not spinel $CuAl_2O_4$ presented. This could be due to the secondary decomposition of as-formed $CuAlO_2$ due to the long dwelling time required to consolidate the pellets in the pressureless sintering.

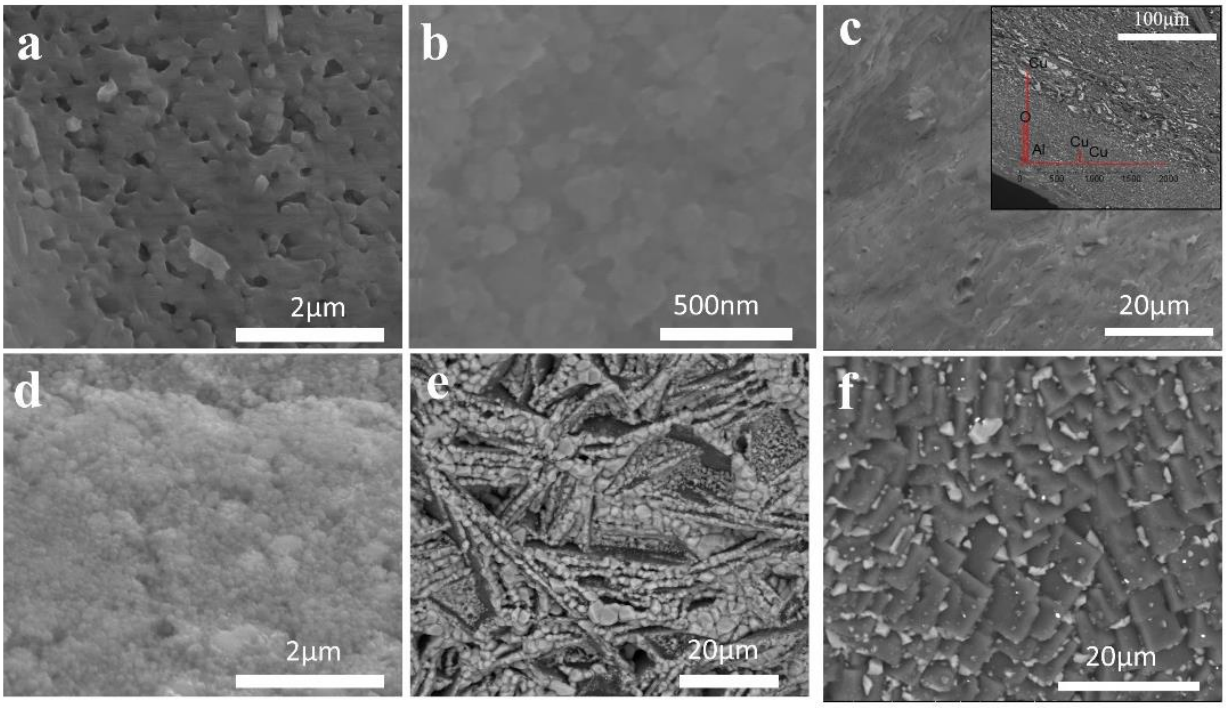

Figure 52. SEM images of samples sintered from CuO-Al_2O_3 precursors. SPS: (a) 700ºC, 10min, 80MPa; (b) 800ºC, 10min, 80MPa; (c) 1000ºC, 10min, 80MPa; FAA: (d) no electric field applied, 1000 ºC, 10hr; (e) 10kV/cm,1000 ºC, 10hr; (f) 0.25kV/cm, 1000 ºC, 10hr.

The corresponding SEM micrographs exhibit evident variances between the two sintering techniques. Figure 52(a)-(c) illustrate the densification of reactive synthesized $CuAlO_2$ particles at elevated sintering temperatures. Laminar grains were observed in Fig. 3c in a direction perpendicular to the uniaxial press. The inset of Figure 52(c) shows the onset of lamination at the surface. The surface layer is Cu-rich from the EDS spectra, indicating a partial Cu redox might occur near the surface when SPS sintering at higher temperatures. The outside layer of the SPS sample in contact with graphite mold and vacuum surroundings may be more likely to undergo the Cu redox reaction than the inner parts. The release of oxygen from the solid-state reaction during sintering could ease the low oxygen partial pressure in the inner parts, thus facilitating the formation of delafossite and prevent the Cu reduction. The FAA treatment in both low and high electric field yielded different microstructures. When high electric field was applied, the lath-shaped domain structure was formed whereas a fish-scale-shaped microstructure was

formed at low electric field. The white particles residing in the grain boundaries is alumina rich. Those microstructures with aligned or partially aligned grains may also be beneficial to its anisotropic electrical properties.

The as-sintered samples all exhibit semiconducting behavior depicted by Figure 53(a). Due to the different phase configurations the conductivity varies, with the Cu-rich sample showing the highest conductivity, followed by the phase-pure $CuAlO_2$ by SPS reactive sintering at 800ºC. The FAA treated samples show lower conductivity because of the presence of alumina phase. Additionally, with the phase separation and the increase of heterointerfaces, the DC conductivity was impaired significantly. Table VII also summarizes some electrical properties obtained by Van der Pauw–Hall method. The conductivity measured from four-point probe is consistent with the observation from Figure 53(a). All the samples exhibit p-type conductivity and the carrier densities decrease significantly as the increase portion of non-conducting alumina.

Table VII. Electrical Properties of Selected Samples Measured by Hall Measurement.

Sintering method - Starting powder	σ (Scm^{-1})	R_H (cm^3C^{-1})	n_p (cm^{-3})
$CuAlO_2$ powder pellet	0.029	+8.65	7.22×10^{17}
SPS-$CuAlO_2$	0.427	+5.24	1.19×10^{18}
SPS-CuO-Al_2O_3-800ºC	0.132	+4.38	1.43×10^{18}
SPS-CuO-Al_2O_3-1000ºC	0.220	+3.24	1.93×10^{18}
FAA-10kV/cm- CuO-Al_2O_3	0.005	+12.8	4.88×10^{17}
FAA-0.25kV/cm- CuO-Al_2O_3	0.007	+14.5	4.3×10^{17}

The $CuAlO_2$ could also emit light in the UV-blue regions at room temperatures due to the near-band-edge excitation, which could be regarded as a sensitive approach to confirm the phase purity and examine the crystallinity. The photoluminescence emission spectra shown in Figure 53(b) summarized the samples with different phase configurations involved in this study. When comparing the phase pure bulk $CuAlO_2$ with sol-gel synthesized nanopowders, the emission peak from the bulk sample is well defined

with a slight red-shift due to the weak quantum confinement[119]. There is a small should peak at around 380nm in the nanopowders, which could be ascribed to the intrinsic luminescent band from alumina. In the bulk samples, only the broad and intensified $CuAlO_2$ direct transition was presented. There are no other emission bands in the visible region identified in both samples. In Figure 53(c), the pressureless sintered sample in high electric field shows two emission bands at 460nm and 485nm respectively. Considering the bandgap of CuO (1.6eV), Cu_2O(2.3eV) and $CuAl_2O_4$ (2.1eV)[170], it is unlikely for those compounds to emit in this region. Therefore, the observed shortened Stokes shift in this sample after long dwelling in air might be originated from Cu^{2+} ions embedded in $CuAlO_2$ or alumina matrix. There is a tiny band at ~600nm which could be attributed to the near-band-edge emission from $CuAl_2O_4$ phase. This phase amount may not be sufficient to be revealed by the XRD, however the PL spectra could be utilized to identify if any metastable spinel phase remains after heating over 1000ºC. Figure 53(d) corresponds to the $CuAlO_2$ powder sintered by SPS. The dominant peak centered at ~540nm correspond to the existence of Cu_2O, which is not observed in FAA and reactive SPS samples. This may lead to the similar conjecture that the direct SPS sintering of $CuAlO_2$ could expedite the reduction of Cu(II) and the metastable Cu(I) after high temperature sintering may reside in either Cu_xO or alumina after the total decomposition of the $CuAlO_2$.

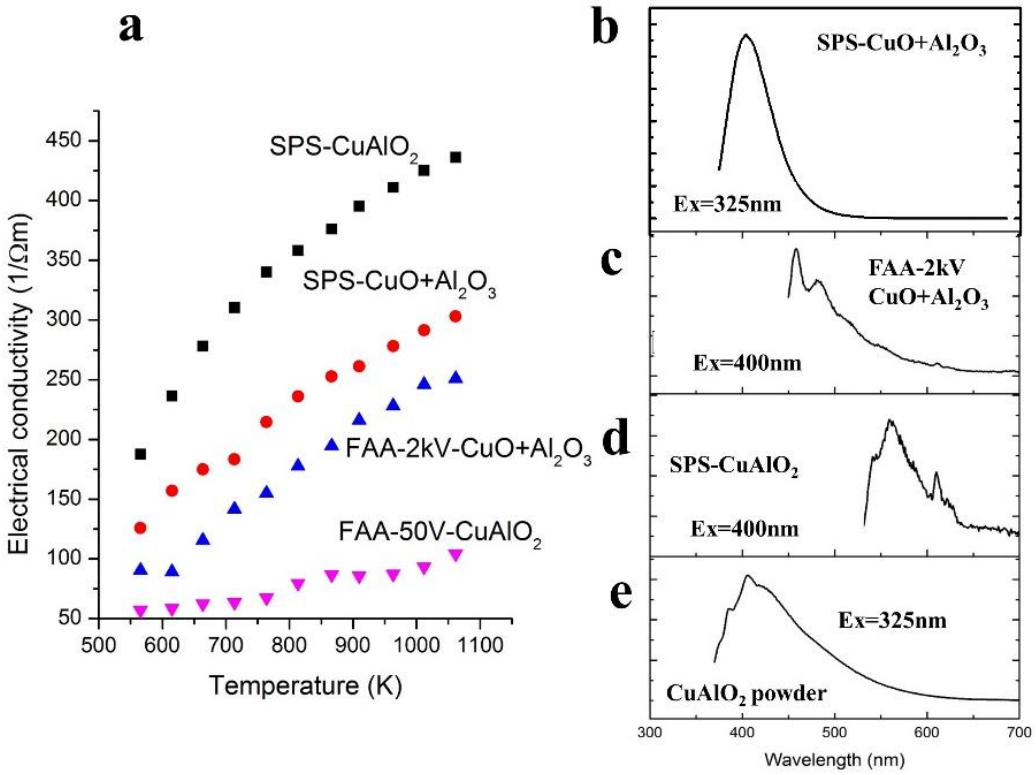

Figure 53. (a) Temperature dependent conductivity (sintering technique-starting powder) and (b) room-temperature photoluminescence emission spectra.

C. Summary

In conclusion, we presented the difficulties of direct consolidation of $CuAlO_2$ powders under electric field in both low vacuum and ambient. The thermodynamic stability of $CuAlO_2$ could be impaired even under the circumstances of stable CuO-Al_2O_3 solid reaction upon heating above 1000ºC with similar activation energies in both low oxygen partial pressure and air. Under intermediate and high DC electric fields, even no pressure and vacuum is applied, the delafossite phase transformation temperature was lowered with trace amount of metastable spinel phase. The proposed reactive synthesis of $CuAlO_2$ through SPS is highly feasible to produce phase pure delafossite confirmed by its bulk optical properties. The tunable microstructures under electric field in this anisotropic material are also favorable for bulk applications and enhancing the electrical conductivity.

SUMMARY AND CONCLUSIONS

This thesis focused on electrohydrodynamic processing of $CuAlO_2$ thinfilms and nanofibers, and optical characterization of $CuAlO_2$ with partial substitution of trivalent ions. Given the recent progress and open questions of transparent conducting oxide being considered for the application of optoelectronics, semiconductors, thermoelectrics and photocatalysis, tuning the microstructure and physics properties are prioritized. In this regard, several main conclusions have been reached in this work:

(1). The electrohydrodynamic technique has been successfully employed to produce $CuAlO_2$ thinfilms and nanofibers, with fine microstructure and moderate electrical properties. After calcination, the $CuAlO_2$ still maintained fibrous structure, which is essential for surface applications.

(2). The modelling of electrospinning process was performed by treating the jet stream as beads segments. According to the simulation, the occurrence of jet whipping in the electric field is caused by perturbation of the equilibrium equations. At low viscosity, multiple trajectories are randomly distributed, indicative of individual bead spray, similar to the electrospray process.

(3). Even though the volume charge density follows log-linear rule with final fiber diameter, a large discrepancy between experimental observation and theoretical prediction is discerned. The drastic change in the slope may indicate that the equilibrium between jet surface tension and electrostatic repulsive force is not met when the jet reached the collector.

(4). The study of Y^{3+}-doped $CuAlO_2$ reveals that the near-band-edge emission is closely related to the 3d-4s hybridization even at room temperature. Additionally, the difference between optical band-gap and band-gap interpreted by near-band-edge emission results from a strong quantum size effect in nanofibrous $CuAlO_2$.

(5). The up- and down- conversion were observed in RE doped $CuAlO_2$ fibers. The delafossite could serve as a promising photoluminescence host due to the accommodation of Al^{3+} site.

FUTURE WORK

The current work consists of two major parts: applying electrohydrodynamic processing on a p-type transparent oxide and the special focus on optical properties of $CuAlO_2$. Regarding to these two parts, some suggestions are proposed for future work.

(1). Compared to the electrospinning, the electrosprayed $CuAlO_2$ thinfilms could serve as a promising alternative for making p-type TCOs. However, the film quality, such as coverage, roughness and uniformity via electrospray still cannot rival other more sophisticated coating method, such as PLD and sputtering. Therefore, there still room for optimizing the electrospray parameters, from precursors to spray conditions.

(2). There have been many well-established modelling methods for electrospinning. However, due to the various physical properties of the precursor and other unknown electrohydrodynamic behaviors during electrospinning, a complete and practical modelling method has not been developed. In this study, the discrepancy between the experimental of PVP electrospinning and the theoretical model may imply that the viscoelastic force could be still dominant at the final stage of the electrospinning. In addition, the mathematical model and code could be improved accordingly and give off more accurate results.

(3). For the photoluminescence characterization, all the measurements were currently performed at room temperature. The effect of trivalent ions on delafossite optical and electrical properties is pronounced. By changing the cation species and tuning the binding energies, the $CuAlO_2$ host could exhibit various PL behaviors. Therefore, it would be more interesting to know the energy transfer at low temperatures, when the trivalent site is substituted or the original band transfer is overshadowed by other activator from rare earth dopants.

REFERENCES

1. H. Kawazoe, M. Yasukawa, H. Hyodo, M. Kurita, H. Yanagi, and H. Hosono, "P-Type Electrical Conduction in Transparent Thin Films of $CuAlO_2$," *Nature,* **389** [6654] 939-42 (1997).

2. D. O. Scanlon, A. Walsh, B. J. Morgan, G. W. Watson, D. J. Payne, and R. G. Egdell, "Effect of Cr Substitution on the Electronic Structure of $CuAl_{1-x}Cr_xO_2$," *Phys. Rev. B,* **79** [3] 035101 (2009).

3. K. Ueda, T. Hase, H. Yanagi, H. Kawazoe, H. Hosono, H. Ohta, M. Orita, and M. Hirano, "Epitaxial Growth of Transparent P-Type Conducting $CuGaO_2$ Thin Films on Sapphire (001) Substrates by Pulsed Laser Deposition," *J. Appl. Phys.,* **89** [3] 1790-3 (2001).

4. H. F. Jiang, X. B. Zhu, H. C. Lei, G. Li, Z. R. Yang, W. H. Song, J. M. Dai, Y. P. Sun, and Y. K. Fu, "Effect of Cr Doping on the Optical–Electrical Property of $CuAlO_2$ Thin Films Derived by Chemical Solution Deposition," *Thin Solid Films,* **519** [8] 2559-63 (2011).

5. C. G. Read, Y. Park, and K.-S. Choi, "Electrochemical Synthesis of P-Type $CuFeO_2$ Electrodes for Use in a Photoelectrochemical Cell," *J. Phys. Chem. Lett.,* **3** [14] 1872-6 (2012).

6. R. Hinogami, K. Toyoda, M. Aizawa, S. Yoshii, T. Kawasaki, and H. Gyoten, "Active Copper Delafossite Anode for Oxygen Evolution Reaction," *Electrochem. Commun.,* **35** 142-5 (2013).

7. K. Mori, H. Sakakibara, H. Usui, and K. Kuroki, "Ideal Band Shape in the Potential Thermoelectric Material $CuAlO_2$: Comparison to Na_xCoO_2," *Phys. Rev. B,* **88** [7] 075141 (2013).

8. S. Thirumalairajan, V. R. Mastelaro, and C. A. Escanhoela Jr, "In-Depth Understanding of the Relation between $CuAlO_2$ Particle Size and Morphology for Ozone Gas Sensor Detection at a Nanoscale Level," *ACS Appl. Mater. Interfaces,* **6** [23] 21739-49 (2014).

9. G. J. Exarhos and X.-D. Zhou, "Discovery-Based Design of Transparent Conducting Oxide Films," *Thin Solid Films,* **515** [18] 7025-52 (2007).

10. G. Exarhos, "Engineering Performance in Tco Films for Energy Applications," *ECS Trans.,* **19** [18] 29-42 (2009).

11. T. J. Coutts, D. L. Young, and X. Li, "Characterization of Transparent Conducting Oxides," *MRS Bull.,* **25** [08] 58-65 (2000).

12. B. G. Lewis and D. C. Paine, "Applications and Processing of Transparent Conducting Oxides," *MRS Bull.,* **25** [08] 22-7 (2000).

13. D. S. Ginley and C. Bright, "Transparent Conducting Oxides," *MRS Bull.,* **25** [08] 15-8 (2000).

14. H. Kim, J. Horwitz, W. Kim, A. Mäkinen, Z. Kafafi, and D. Chrisey, "Doped ZnO Thin Films as Anode Materials for Organic Light-Emitting Diodes," *Thin Solid Films,* **420** 539-43 (2002).

15. Z. Yao, B. He, L. Zhang, C. Zhuang, T. Ng, S. Liu, M. Vogel, A. Kumar, W. Zhang, and C. Lee, "Energy Band Engineering and Controlled P-Type Conductivity of $CuAlO_2$ Thin Films by Nonisovalent Cu-O Alloying," *Appl. Phys. Lett.,* **100** [6] 062102 (2012).

16. T. Konry and R. S. Marks, "Physico-Chemical Studies of Indium Tin Oxide-Coated Fiber Optic Biosensors," *Thin Solid Films,* **492** [1] 313-21 (2005).

17. K. Badeker, "Concerning the Electricity Conductibility and the Thermoelectric Energy of Several Heavy Metal Bonds," *Ann. Phys.(Leipzig),* **22** [4] 749-66 (1907).

18. H.-M. Kwon, D.-W. Han, D.-J. Kwak, and Y.-M. Sung, "Preparation of Nanoporous F-Doped Tin Dioxide Films for TCO-Less Dye-Sensitized Solar Cells Application," *Curr. Appl Phys.,* **10** [2, Supplement] S172-S5 (2010).

19. J. Zhao, W. Zhang, E. Xie, Z. Ma, A. Zhao, and Z. Liu, "Structure and Photoluminescence of $BGa_2O_3:Eu^{3+}$ Nanofibers Prepared by Electrospinning," *Appl. Surf. Sci.,* **257** [11] 4968-72 (2011).

20. J. Chen, J. Wang, F. Zhang, D. Yan, G. Zhang, R. Zhuo, and P. Yan, "Structure and Photoluminescence Property of Eu-Doped SnO_2 Nanocrystalline Powders Fabricated by Sol–Gel Calcination Process," *J. Phys. D: Appl. Phys.,* **41** [10] 105306 (2008).

21. S. Cho, J. Ma, Y. Kim, Y. Sun, G. K. Wong, and J. B. Ketterson, "Photoluminescence and Ultraviolet Lasing of Polycrystalline Zno Thin Films Prepared by the Oxidation of the Metallic Zn," *Appl. Phys. Lett.,* **75** [18] 2761-3 (1999).

22. T. Minami, S. Takata, T. Kakumu, and H. Sonohara, "New Transparent Conducting $MgIn_2O_4$-$Zn_2In_2O_5$ Thin Films Prepared by Magnetron Sputtering," *Thin Solid Films,* **270** [1] 22-6 (1995).

23. T. Minami, K. Shimokawa, and T. Miyata, "P-Type Transparent Conducting In_2O_3–Ag_2O Thin Films Prepared by Rf Magnetron Sputtering," *J. Vac. Sci. Technol., A,* **16** [3] 1218-21 (1998).

24. K. Yanagawa, Y. Ohki, T. Omata, H. Hosono, N. Ueda, and H. Kawazoe, "Preparation of $Cd_{1-x}Y_xSb_2O_6$ Thin Film on Glass Substrate by Radio Frequency Sputtering," *Appl. Phys. Lett.,* **65** [4] 406-8 (1994).

25. R. Cava, J. M. Phillips, J. Kwo, G. Thomas, R. Van Dover, S. Carter, J. Krajewski, W. Peck Jr, J. Marshall, and D. Rapkine, "$GaInO_3$: A New Transparent Conducting Oxide," *Appl. Phys. Lett.,* **64** [16] 2071-2 (1994).

26. J. M. Phillips, R. Cava, G. Thomas, S. Carter, J. Kwo, T. Siegrist, J. Krajewski, J. Marshall, W. Peck Jr, and D. Rapkine, "Zinc-Indium-Oxide: A High Conductivity Transparent Conducting Oxide," *Appl. Phys. Lett.,* **67** [15] 2246-8 (1995).

27. J. Varley, A. Janotti, C. Franchini, and C. Van de Walle, "Role of Self-Trapping in Luminescence and P-Type Conductivity of Wide-Band-Gap Oxides," *Phys. Rev. B,* **85** [8] 081109 (2012).

28. A. Banerjee and K. Chattopadhyay, "Recent Developments in the Emerging Field of Crystalline P-Type Transparent Conducting Oxide Thin Films," *Prog. Cryst. Growth. Ch.,* **50** [1] 52-105 (2005).

29. I. Hamada and H. Katayama-Yoshida, "Energetics of Native Defects In," *Physica B,* **376–377** [0] 808-11 (2006).

30. G. Thomas, "Materials Science: Invisible Circuits," *Nature,* **389** [6654] 907-8 (1997).

31. R. D. Shannon, D. B. Rogers, and C. T. Prewitt, "Chemistry of Noble Metal Oxides. I. Syntheses and Properties of ABO_2 Delafossite Compounds," *Inorg. Chem.,* **10** [4] 713-8 (1971).

32. A. Buljan, M. Llunell, E. Ruiz, and P. Alemany, "Color and Conductivity in Cu_2O and $CuAlO_2$: A Theoretical Analysis of D10···D10 Interactions in Solid-State Compounds," *Chem. Mater.,* **13** [2] 338-44 (2001).

33. M. Lalic, J. Mestnik-Filho, A. Carbonari, R. Saxena, and M. Moralles, "Influence of Cd Impurity on the Electronic Properties of $CuAlO_2$ Delafossite: First-Principles Calculations," *J. Phys.: Condens. Matter.,* **14** [22] 5517 (2002).

34. A. Banerjee, R. Maity, and K. Chattopadhyay, "Preparation of P-Type Transparent Conducting $CuAlO_2$ Thin Films by Reactive DC Sputtering," *Mater. Lett.,* **58** [1] 10-3 (2004).

35. G. Dong, M. Zhang, W. Lan, P. Dong, and H. Yan, "Structural and Physical Properties of Mg-Doped $CuAlO_2$ Thin Films," *Vacuum,* **82** [11] 1321-4 (2008).

36. H. Jiang, X. Wang, X. Zang, W. Wu, S. Sun, C. Xiong, W. Yin, C. Gui, and X. Zhu, "Electronic Properties of Bivalent Cations (Be, Mg and Ca) Substitution for Al in Delafossite $CuAlO_2$ Semiconductor by First-Principles Calculations," *J. Alloy. Compd.,* **553** 245-52 (2013).

37. B. W. Huang, C. Y. Wen, G. W. Lin, P. Y. Chen, Y. H. Jiang, P. K. Kao, C. T. Chi, H. Chang, I. Cheng, and J. Z. Chen, "Influence of Ca/Al Ratio on Properties of Amorphous/Nanocrystalline Cu–Al–Ca–O Thin Films," *J. Am. Ceram. Soc.,* **98** [1] 125-9 (2015).

38. C.-Y. Tsay and C.-L. Chen, "Improved Electrical Properties of P-Type $CuGaO_2$ Semiconductor Thin Films through Mg and Zn Doping," *Ceram. Int.,* **43** [2] 2563-7 (2017).

39. C.-Y. Tsay and C.-L. Chen, "Growth and Characterization of Sol-Gel Derived $CuGaO_2$ Semiconductor Thin Films for Uv Photodetector Application," *J. Cryst. Growth.,* (2016).

40. S. Rojas, T. Joshi, R. Wheatley, M. Sarabia, P. Borisov, D. Lederman, and A. Cabrera, "Optical Detection of Carbon Dioxide Adsorption on Epitaxial $CuFe_{1-x}Ga_xO_2$ Delafossite Film Grown by Pulse Laser Deposition," *Surf. Sci.,* **648** 23-8 (2016).

41. D. Xiong, Q. Zhang, S. K. Verma, H. Li, W. Chen, and X. Zhao, "Use of Delafossite Oxides $CuCr_{1-x}Ga_xO_2$ Nanocrystals in P-Type Dye-Sensitized Solar Cell," *J. Alloy. Compd.,* **662** 374-80 (2016).

42. D. Xiong, X. Zeng, W. Zhang, H. Wang, X. Zhao, W. Chen, and Y.-B. Cheng, "Synthesis and Characterization of $CuAlO_2$ and $AgAlO_2$ Delafossite Oxides through Low-Temperature Hydrothermal Methods," *Inorg. Chem.,* (2014).

43. D. Byrne, N. Bennett, and A. Cowley, "The Role of Annealing Conditions on the Low Temperature Photoluminescence Properties of $CuAlO_2$," *J. Lumin.,* **170** 212-8 (2016).

44. D. Byrne, A. Cowley, N. Bennett, and E. McGlynn, "The Luminescent Properties of $CuAlO_2$," *J. Mater. Chem. C,* **2** [37] 7859-68 (2014).

45. D. O. Scanlon and G. W. Watson, "Conductivity Limits in $CuAlO_2$ from Screened-Hybrid Density Functional Theory," *J. Phys. Chem. Lett.,* **1** [21] 3195-9 (2010).

46. B. A. Williamson, J. Buckeridge, J. Brown, S. Ansbro, R. G. Palgrave, and D. O. Scanlon, "Engineering Valence Band Dispersion for High Mobility P-Type Semiconductors," *Chem. Mater.*, (2016).

47. A. Jacob, C. Parent, P. Boutinaud, G. Le Flem, J. Doumerc, A. Ammar, M. Elazhari, and M. Elaatmani, "Luminescent Properties of Delafossite-Type Oxides $LaCuO_2$ and $YCuO_2$," *Solid State Commun.,* **103** [9] 529-32 (1997).

48. G. Le Flem, "Monovalent Copper in Insulators," *J. Alloy. Compd.,* **188** 36-41 (1992).

49. C. Parent, P. Boutinaud, G. Le Flem, B. Moine, C. Pedrini, D. Garcia, and M. Faucher, "Monovalent Copper-Activated Oxygenated Insulators," *Opt. Mater.,* **4** [1] 107-13 (1994).

50. P. Boutinaud, C. Parent, G. Le Flem, C. Pedrini, and B. Moine, "Spectroscopic Investigation of the Copper (I)-Rich Phosphate $CuZr_2(PO_4)_3$,"*J. Phys.: Condens. Matter.,* **4** [11] 3031 (1992).

51. S. Chiu and J. Huang, "Characterization of P-Type $CuAlO_2$ Thin Films Grown by Chemical Solution Deposition," *Surf. Coat. Technol.,* **231** 239-42 (2013).

52. M. Fang, H. He, B. Lu, W. Zhang, B. Zhao, Z. Ye, and J. Huang, "Optical Properties of P-Type $CuAlO_2$ Thin Film Grown by Rf Magnetron Sputtering," *Appl. Surf. Sci.,* **257** [20] 8330-3 (2011).

53. H. Fong, I. Chun, and D. Reneker, "Beaded Nanofibers Formed During Electrospinning," *Polymer,* **40** [16] 4585-92 (1999).

54. A. L. Yarin, S. Koombhongse, and D. H. Reneker, "Taylor Cone and Jetting from Liquid Droplets in Electrospinning of Nanofibers," *J. Appl. Phys.,* **90** [9] 4836-46 (2001).

55. D. Li and Y. Xia, "Electrospinning of Nanofibers: Reinventing the Wheel?," *Adv. Mater.,* **16** [14] 1151-70 (2004).

56. W. Sigmund, J. Yuh, H. Park, V. Maneeratana, G. Pyrgiotakis, A. Daga, J. Taylor, and J. C. Nino, "Processing and Structure Relationships in Electrospinning of Ceramic Fiber Systems," *J. Am. Ceram. Soc.,* **89** [2] 395-407 (2006).

57. Y. Wu and R. L. Clark, "Electrohydrodynamic Atomization: A Versatile Process for Preparing Materials for Biomedical Applications," *J. Biomater. Sci., Polym. Ed.,* **19** [5] 573-601 (2008).

58. Y. Liu, T. L. Olson, and Y. Wu, "Luminescence and Microstructure of Nd Doped $Y_2Si_2O_7$ Electrospun Fibers," *J. Am. Ceram. Soc.,* **97** [8] 2390-3 (2014).

59. H. Wu, L. Hu, M. W. Rowell, D. Kong, J. J. Cha, J. R. McDonough, J. Zhu, Y. Yang, M. D. McGehee, and Y. Cui, "Electrospun Metal Nanofiber Webs as High-Performance Transparent Electrode," *Nano Lett.,* **10** [10] 4242-8 (2010).

60. D. Li and Y. Xia, "Direct Fabrication of Composite and Ceramic Hollow Nanofibers by Electrospinning," *Nano Lett.,* **4** [5] 933-8 (2004).

61. K. Mahmood, R. Munir, H. W. Kang, and H. J. Sung, "An Atmospheric Pressure-Based Electrospraying Route to Fabricate the Multi-Applications Bilayer (AZO/ITO) TCO Films," *RSC Adv.,* **3** [48] 25741-51 (2013).

62. B. Liu, K. Nakata, M. Sakai, H. Saito, T. Ochiai, T. Murakami, K. Takagi, and A. Fujishima, "Mesoporous TiO_2 Core–Shell Spheres Composed of Nanocrystals with Exposed High-Energy Facets: Facile Synthesis and Formation Mechanism," *Langmuir,* **27** [13] 8500-8 (2011).

63. D. Li and Y. Xia, "Fabrication of Titania Nanofibers by Electrospinning," *Nano Lett.,* **3** [4] 555-60 (2003).

64. Z. Liu, D. D. Sun, P. Guo, and J. O. Leckie, "An Efficient Bicomponent TiO_2/SnO_2 Nanofiber Photocatalyst Fabricated by Electrospinning with a Side-by-Side Dual Spinneret Method," *Nano Lett.,* **7** [4] 1081-5 (2007).

65. Z. Zhang, C. Shao, X. Li, L. Zhang, H. Xue, C. Wang, and Y. Liu, "Electrospun Nanofibers of ZnO− SnO_2 Heterojunction with High Photocatalytic Activity," *J. Phys. Chem. C,* **114** [17] 7920-5 (2010).

66. Y. Ding, Y. Wang, L. Zhang, H. Zhang, and Y. Lei, "Preparation, Characterization and Application of Novel Conductive Nio–Cdo Nanofibers with Dislocation Feature," *J. Mater. Chem.,* **22** [3] 980-6 (2012).

67. O. Wilhelm, S. Pratsinis, D. Perednis, and L. Gauckler, "Electrospray and Pressurized Spray Deposition of Yttria-Stabilized Zirconia Films," *Thin Solid Films,* **479** [1] 121-9 (2005).

68. A.-M. Azad, "Fabrication of Yttria-Stabilized Zirconia Nanofibers by Electrospinning," *Mater. Lett.,* **60** [1] 67-72 (2006).

69. Y. Matsushima, T. Yamazaki, K. Maeda, and T. Suzuki, "Fabrication of SnO_2 Particle-Layers Using the Electrospray Method and Gas Sensing Properties for H_2," *J. Electroceram.,* **13** [1-3] 765-70 (2004).

70. A. Hosseinmardi, N. Shojaee, M. Keyanpour-Rad, and T. Ebadzadeh, "A Study on the Photoluminescence Properties of Electrospray Deposited Amorphous and Crystalline Nanostructured ZnO Thin Films," *Ceram. Int.,* **38** [3] 1975-80 (2012).

71. A. Bazargan, S. Fateminia, M. E. Ganji, and M. Bahrevar, "Electrospinning Preparation and Characterization of Cadmium Oxide Nanofibers," *Chem. Eng. J.,* **155** [1] 523-7 (2009).

72. X. Yang, C. Shao, Y. Liu, R. Mu, and H. Guan, "Nanofibers of CeO_2 Via an Electrospinning Technique," *Thin Solid Films,* **478** [1–2] 228-31 (2005).

73. G. Larsen, R. Velarde-Ortiz, K. Minchow, A. Barrero, and I. G. Loscertales, "A Method for Making Inorganic and Hybrid (Organic/Inorganic) Fibers and Vesicles with Diameters in the Submicrometer and Micrometer Range Via Sol-Gel Chemistry and Electrically Forced Liquid Jets," *J. Am. Chem. Soc.,* **125** [5] 1154-5 (2003).

74. Y. Mizuno, E. Hosono, T. Saito, M. Okubo, D. Nishio-Hamane, K. Oh-ishi, T. Kudo, and H. Zhou, "Electrospinning Synthesis of Wire-Structured $LiCoO_2$ for Electrode Materials of High-Power Li-Ion Batteries," *J. Phys. Chem. C,* **116** [19] 10774-80 (2012).

75. C. Shao, H. Guan, Y. Liu, and R. Mu, "MgO Nanofibres Via an Electrospinning Technique," *J. Mater. Sci.,* **41** [12] 3821-4 (2006).

76. D. Li, J. T. McCann, Y. Xia, and M. Marquez, "Electrospinning: A Simple and Versatile Technique for Producing Ceramic Nanofibers and Nanotubes," *J. Am. Ceram. Soc.,* **89** [6] 1861-9 (2006).

77. D. P. Smith, "The Electrohydrodynamic Atomization of Liquids," *IEEE T. Ind. Appl.,* [3] 527-35 (1986).

78. B. K. Ku and S. S. Kim, "Electrospray Characteristics of Highly Viscous Liquids," *J. Aerosol. Sci.,* **33** [10] 1361-78 (2002).

79. J. Rosell-Llompart and J. F. De La Mora, "Generation of Monodisperse Droplets 0.3 to 4 Mm in Diameter from Electrified Cone-Jets of Highly Conducting and Viscous Liquids," *J. Aerosol. Sci.,* **25** [6] 1093-119 (1994).

80. R. Hartman, D. Brunner, D. Camelot, J. Marijnissen, and B. Scarlett, "Jet Break-up in Electrohydrodynamic Atomization in the Cone-Jet Mode," *J. Aerosol. Sci.,* **31** [1] 65-95 (2000).

81. M. M. Hohman, M. Shin, G. Rutledge, and M. P. Brenner, "Electrospinning and Electrically Forced Jets. Ii. Applications," *Phys. Fluids,* **13** [8] 2221-36 (2001).

82. M. M. Hohman, M. Shin, G. Rutledge, and M. P. Brenner, "Electrospinning and Electrically Forced Jets. I. Stability Theory," *Phys. Fluids,* **13** [8] 2201-20 (2001).

83. J. Feng, "The Stretching of an Electrified Non-Newtonian Jet: A Model for Electrospinning," *Phys. Fluids,* **14** [11] 3912-26 (2002).

84. S. V. Fridrikh, H. Y. Jian, M. P. Brenner, and G. C. Rutledge, "Controlling the Fiber Diameter During Electrospinning," *Phys. Rev. Lett.,* **90** [14] 144502 (2003).

85. J. T. McCann, D. Li, and Y. Xia, "Electrospinning of Nanofibers with Core-Sheath, Hollow, or Porous Structures," *J. Mater. Chem.,* **15** [7] 735-8 (2005).

86. X. Ji, P. Wang, Z. Su, G. Ma, and S. Zhang, "Enabling Multi-Enzyme Biocatalysis Using Coaxial-Electrospun Hollow Nanofibers: Redesign of Artificial Cells," *J. Mater. Chem. B,* **2** [2] 181-90 (2014).

87. S. Nakamura, "The Roles of Structural Imperfections in Ingan-Based Blue Light-Emitting Diodes and Laser Diodes," *Science,* **281** [5379] 956-61 (1998).

88. C. A. Mirkin, "Tweezers for the Nanotool Kit," *Science,* **286** [5447] 2095-6 (1999).

89. R. O'barr, M. Lederman, S. Schultz, W. Xu, A. Scherer, and R. Tonucci, "Preparation and Quantitative Magnetic Studies of Single-Domain Nickel Cylinders," *J. Appl. Phys.,* **79** [8] 5303-5 (1996).

90. H. Song, H. Yu, G. Pan, X. Bai, B. Dong, X. Zhang, and S. Hark, "Electrospinning Preparation, Structure, and Photoluminescence Properties of Ybo3: Eu3+ Nanotubes and Nanowires," *Chem. Mater.,* **20** [14] 4762-7 (2008).

91. G. Dong, X. Xiao, Y. Chi, B. Qian, X. Liu, Z. Ma, E. Wu, H. Zeng, D. Chen, and J. Qiu, "Size-Dependent Polarized Photoluminescence from $Y_3Al_5O_{12}:Eu^{3+}$ Single Crystalline Nanofiber Prepared by Electrospinning," *J. Mater. Chem.,* **20** [8] 1587-93 (2010).

92. R. S. Devan, R. A. Patil, J. H. Lin, and Y. R. Ma, "One-Dimensional Metal-Oxide Nanostructures: Recent Developments in Synthesis, Characterization, and Applications," *Adv. Funct. Mater.,* **22** [16] 3326-70 (2012).

93. A. B. Suryamas, M. M. Munir, F. Iskandar, and K. Okuyama, "Photoluminescent and Crystalline Properties of $Y_{3-x}Al_5O_{12}:Ce_x^{3+}$ Phosphor Nanofibers Prepared by Electrospinning," *J. Appl. Phys.,* **105** [6] 064311 (2009).

94. Y. Liu, Y. Huang, H. J. Seo, and Y. Wu, "Blueshift in near-Band-Edge Emission in Y^{3+}-Doped $CuAlO_2$ Nanofibers," *Opt. Mater. Express,* **4** [12] 2602-7 (2014).

95. Y. Liu, Y. Gong, N. P. Mellott, B. Wang, H. Ye, and Y. Wu, "Luminescence of Delafossite-Type $CuAlO_2$ Fibers with Eu Substitution for Al Cations," *Sci. Technol. Adv. Mater.* , **17** [1] 200-9 (2016).

96. B. J. Ingram, G. B. González, T. O. Mason, D. Y. Shahriari, A. Barnabe, D. Ko, and K. R. Poeppelmeier, "Transport and Defect Mechanisms in Cuprous Delafossites. 1. Comparison of Hydrothermal and Standard Solid-State Synthesis in $CuAlO_2$," *Chem. Mater.,* **16** [26] 5616-22 (2004).

97. A. P. Amrute, Z. Łodziana, C. Mondelli, F. Krumeich, and J. Perez-Ramirez, "Solid-State Chemistry of Cuprous Delafossites: Synthesis and Stability Aspects," *Chem. Mater.,* **25** [21] 4423-35 (2013).

98. Z. Deng, X. Zhu, R. Tao, W. Dong, and X. Fang, "Synthesis of $CuAlO_2$ Ceramics Using Sol-Gel," *Mater. Lett.,* **61** [3] 686-9 (2007).

99. D. Y. Shahriari, A. Barnabe, T. O. Mason, and K. R. Poeppelmeier, "A High-Yield Hydrothermal Preparation of $CuAlO_2$," *Inorg. Chem.,* **40** [23] 5734-5 (2001).

100. A. Banerjee, S. Kundoo, and K. Chattopadhyay, "Synthesis and Characterization of P-Type Transparent Conducting $CuAlO_2$ Thin Film by DC Sputtering," *Thin Solid Films,* **440** [1] 5-10 (2003).

101. M. Neumann-Spallart, S. Pai, and R. Pinto, "Pld Growth of $CuAlO_2$," *Thin Solid Films,* **515** [24] 8641-4 (2007).

102. N. Dasgupta, W. Lee, T. P. Holme, and F. B. Prinz. Google Patents, 2010.

103. M. Ohashi, Y. Iida, and H. Morikawa, "Preparation of $CuAlO_2$ Films by Wet Chemical Synthesis," *J. Am. Ceram. Soc.,* **85** [1] 270-2 (2002).

104. H. Jiang, H. Lei, X. Zhu, G. Li, Z. Yang, W. Song, J. Dai, Y. Sun, and Y. Fu, "Effects of Citric Acid on Properties of Single Phase $CuAlO_2$ Thin Films Derived by Chemical Solution Deposition," *J. Alloy. Compd.,* **487** [1] 404-8 (2009).

105. N. Serin, T. Serin, Ş. Horzum, and Y. Çelik, "Annealing Effects on the Properties of Copper Oxide Thin Films Prepared by Chemical Deposition," *Semicond. Sci. Tech.,* **20** [5] 398 (2005).

106. W. Lan, W. Cao, M. Zhang, X. Liu, Y. Wang, E. Xie, and H. Yan, "Annealing Effect on the Structural, Optical, and Electrical Properties of $CuAlO_2$ Films Deposited by Magnetron Sputtering," *J. Mater. Sci.,* **44** [6] 1594-9 (2009).

107. S. Zhao, M. Li, X. Liu, and G. Han, "Synthesis of $CuAlO_2$ Nanofibrous Mats by Electrospinning," *Mater. Chem. Phys.,* **116** [2] 615-8 (2009).

108. H. F. Jiang, X. B. Zhu, H. C. Lei, G. Li, Z. R. Yang, W. H. Song, J. M. Dai, Y. P. Sun, and Y. K. Fu, "Effects of Mg Substitution on the Structural, Optical, and Electrical Properties of $CuAlO_2$ Thin Films," *J. Alloy. Compd.,* **509** [5] 1768-73 (2011).

109. X. Zhang, S. Xu, and G. Han, "Fabrication and Photocatalytic Activity of TiO_2 Nanofiber Membrane," *Mater. Lett.,* **63** [21] 1761-3 (2009).

110. Z. Zhang, X. Li, C. Wang, L. Wei, Y. Liu, and C. Shao, "Zno Hollow Nanofibers: Fabrication from Facile Single Capillary Electrospinning and Applications in Gas Sensors," *J. Phys. Chem. C,* **113** [45] 19397-403 (2009).

111. J. Doshi and D. H. Reneker, "Electrospinning Process and Applications of Electrospun Fibers," *J. Electrostat.,* **35** [2-3] 151-60 (1995).

112. D. H. Reneker, A. L. Yarin, H. Fong, and S. Koombhongse, "Bending Instability of Electrically Charged Liquid Jets of Polymer Solutions in Electrospinning," *J. Appl. Phys.,* **87** [9] 4531-47 (2000).

113. S. Karra, "Modeling Electrospinning Process and a Numerical Scheme Using Lattice Boltzmann Method to Simulate Viscoelastic Fluid Flows"; Texas A&M University, 2007.

114. A. L. Yarin, S. Koombhongse, and D. H. Reneker, "Bending Instability in Electrospinning of Nanofibers," *J. Appl. Phys.,* **89** [5] 3018-26 (2001).

115. S. Theron, A. Yarin, E. Zussman, and E. Kroll, "Multiple Jets in Electrospinning: Experiment and Modeling," *Polymer,* **46** [9] 2889-99 (2005).

116. A. Bernal, I. Kuritka, and P. Saha, "Poly (Vinyl Alcohol)-Poly (Vinyl Pyrrolidone) Blends: Preparation and Characterization for a Prospective Medical Application", *Proceedings of the 13th WSEAS international conference on Mathematical and computational methods in science and engineering*, 978-1 (2001).

117. H. Y. Chen and M. W. Tsai, "Delafossite- $CuAlO_2$ Thin Films Prepared by Thermal Annealing," *J. Nano Res.,* **13** 81-6 (2011).

118. A. N. Banerjee, S. W. Joo, and B.-K. Min, "Quantum Size Effect in the Photoluminescence Properties of P-Type Semiconducting Transparent $CuAlO_2$ Nanoparticles," *J. Appl. Phys.,* **112** [11] 114329 (2012).

119. A. Banerjee and K. Chattopadhyay, "Size-Dependent Optical Properties of Sputter-Deposited Nanocrystalline P-Type Transparent $CuAlO_2$ Thin Films," *J. Appl. Phys.,* **97** [8] 084308 (2005).

120. R. Mo and Y. Liu, "Synthesis and Properties of Delafossite $CuAlO_2$ Nanowires," *J. Sol-gel. Sci. Techn.,* **57** [1] 16-9 (2011).

121. H. Gao, J. Zhou, and M. Lu, "First Principles Study of $CuAlO_2$ Doping with S," *Sci. China Phys. Mech. Astron.,* **53** [7] 1261-5 (2010).

122. R.-S. Yu, S.-C. Liang, C.-J. Lu, D.-C. Tasi, and F.-S. Shieu, "Characterization and Optoelectronic Properties of P-Type N-Doped $CuAlO_2$ Films," *Appl. Phys. Lett.,* **90** [19] 191117--3 (2007).

123. Y. Liu, T. L. Olson, and Y. Wu, "Luminescence and Microstructure of Nd Doped $Y_2Si_2O_7$ Electrospun Fibers," *J. Am. Ceram. Soc.,* (2014).

124. H. Ko, Y. Chen, Z. Zhu, T. Yao, I. Kobayashi, and H. Uchiki, "Photoluminescence Properties of Zno Epilayers Grown on CaF_2 (111) by Plasma Assisted Molecular Beam Epitaxy," *Appl. Phys. Lett.,* **76** [14] 1905-7 (2000).

125. R. Laskowski, N. E. Christensen, P. Blaha, and B. Palanivel, "Strong Excitonic Effects in $CuAlO_2$ Delafossite Transparent Conductive Oxides," *Phys. Rev. B.,* **79** [16] 165209 (2009).

126. C. H. Ong and H. Gong, "Effects of Aluminum on the Properties of P-Type Cu–Al–O Transparent Oxide Semiconductor Prepared by Reactive Co-Sputtering," *Thin Solid Films,* **445** [2] 299-303 (2003).

127. A. Buljan, P. Alemany, and E. Ruiz, "Electronic Structure and Bonding in $CuMO_2$ (M= Al, Ga, Y) Delafossite-Type Oxides: An Ab Initio Study," *J. Phys. Chem. B,* **103** [38] 8060-6 (1999).

128. N. Tsuboi, T. Hoshino, H. Ohara, T. Suzuki, S. Kobayashi, K. Kato, and F. Kaneko, "Control of Luminescence and Conductivity of Delafossite-Type $CuYO_2$ by Substitution of Rare Earth Cation (Eu, Tb) and/or Ca Cation for Y Cation," *J. Phys. Chem. Solids.,* **66** [11] 2134-8 (2005).

129. M. Lee, T. Kim, and D. Kim, "Anisotropic Electrical Conductivity of Delafossite-Type $CuAlO_2$ Laminar Crystal," *Appl. Phys. Lett.,* **79** [13] 2028-30 (2001).

130. W. Bu, Z. Hua, H. Chen, and J. Shi, "Epitaxial Synthesis of Uniform Cerium Phosphate One-Dimensional Nanocable Heterostructures with Improved Luminescence," *J. Phys. Chem. B,* **109** [30] 14461-4 (2005).

131. G. Jia, Y. Zheng, K. Liu, Y. Song, H. You, and H. Zhang, "Facile Surfactant-and Template-Free Synthesis and Luminescent Properties of One-Dimensional Lu_2O_3: Eu^{3+} Phosphors," *J. Phys. Chem. C,* **113** [1] 153-8 (2008).

132. J. Yang, C. Li, Z. Cheng, X. Zhang, Z. Quan, C. Zhang, and J. Lin, "Size-Tailored Synthesis and Luminescent Properties of One-Dimensional $Gd_2O_3:Eu^{3+}$ Nanorods and Microrods," *J. Phys. Chem. C,* **111** [49] 18148-54 (2007).

133. Z. Xia, G. Liu, J. Wen, Z. Mei, M. Balasubramanian, M. S. Molokeev, L. Peng, L. Gu, D. J. Miller, and Q. Liu, "Tuning of Photoluminescence by Cation Nanosegregation in the $(CaMg)_x(NaSc)_{1-x}Si_2O_6$ Solid Solution," *J. Am. Chem. Soc.,* **138** [4] 1158-61 (2016).

134. Z. Xia, C. Ma, M. S. Molokeev, Q. Liu, K. Rickert, and K. R. Poeppelmeier, "Chemical Unit Cosubstitution and Tuning of Photoluminescence in the $Ca_2(Al_{1-x}Mg_x)(Al_{1-x}Si_{1+x})O_7:Eu^{2+}$ Phosphor," *J. Am. Chem. Soc.,* **137** [39] 12494-7 (2015).

135. K. Jacob and C. Alcock, "Thermodynamics of $CuAlO_2$ and $CuAl_2O_4$ and Phase Equilibria in the System Cu_2O-CuO-Al_2O_3," *J. Am. Ceram. Soc.,* **58** [5-6] 192-5 (1975).

136. K. Isawa, Y. Yaegashi, M. Komatsu, M. Nagano, S. Sudo, M. Karppinen, and H. Yamauchi, "Synthesis of Delafossite-Derived Phases, $RCuO_{2+\Delta}$ with R= Y, La, Pr, Nd, Sm, and Eu, and Observation of Spin-Gap-Like Behavior," *Phys. Rev. B,* **56** [6] 3457 (1997).

137. M. Chong, K. Pita, and C. Kam, "Photoluminescence of Sol–Gel-Derived $Y_2O_3:Eu^{3+}$ Thin-Film Phosphors with Mg^{2+} and Al^{3+} Co-Doping," *Appl. Phys. A,* **79** [3] 433-7 (2004).

138. N. Tsuboi, H. Ohara, T. Hoshino, S. Kobayashi, K. Kato, and F. Kaneko, "Luminescence Properties of Delafossite-Type $CuYO_2$ Doped with Calcium, Oxygen or Rare Earth Tb," *Jpn. J. Appl. Phys.,* **44** [1S] 765 (2005).

139. Y. Kumekawa, M. Hirai, Y. Kobayashi, S. Endoh, E. Oikawa, and T. Hashimoto, "Evaluation of Thermodynamic and Kinetic Stability of $CuAlO_2$ and $CuGaO_2$," *J. Therm. Anal. Calorim.,* **99** [1] 57-63 (2010).

140. Q.-J. Liu, N.-C. Zhang, Y.-Y. Sun, F.-S. Liu, and Z.-T. Liu, "Structural, Mechanical, Electronic, Optical Properties and Effective Masses of $CuMO_2$ (M= Sc, Y, La) Compounds: First-Principles Calculations," *Solid State Sci.,* **31** 37-45 (2014).

141. D. Byrne, A. Cowley, N. Bennett, and E. McGlynn, "The Luminescent Properties of $CuAlO_2$," *J. Mater. Chem. C,* **2** [37] 7859-68 (2014).

142. A. Kumar, R. Jose, K. Fujihara, J. Wang, and S. Ramakrishna, "Structural and Optical Properties of Electrospun TiO_2 Nanofibers," *Chem. Mater.,* **19** [26] 6536-42 (2007).

143. A. Naldoni, M. Allieta, S. Santangelo, M. Marelli, F. Fabbri, S. Cappelli, C. L. Bianchi, R. Psaro, and V. Dal Santo, "Effect of Nature and Location of Defects on Bandgap Narrowing in Black TiO_2 Nanoparticles," *J. Am. Chem. Soc.,* **134** [18] 7600-3 (2012).

144. A. Ahmad, T. Jagadale, V. Dhas, S. Khan, S. Patil, R. Pasricha, V. Ravi, and S. Ogale, "Fungus-Based Synthesis of Chemically Difficult-to-Synthesize Multifunctional Nanoparticles of Cualo2," *Adv. Mater.,* **19** [20] 3295-9 (2007).

145. J. Zhang and Y. Wang, "Eu^{3+}-Doped $Ba_3Bi(PO_4)_3$: A Red Phosphor for White Light-Emitting Diodes," *Electrochem. Solid-State Lett.,* **13** [4] J35-J7 (2010).

146. O. Yassin, S. Alamri, and A. Joraid, "Effect of Particle Size and Laser Power on the Raman Spectra of $CuAlO_2$ Delafossite Nanoparticles," *J. Phys. D: Appl. Phys.,* **46** [23] 235301 (2013).

147. J. Pellicer-Porres, D. Martinez-Garcia, A. Segura, P. Rodriguez-Hernandez, A. Munoz, J. Chervin, N. Garro, and D. Kim, "Pressure and Temperature Dependence of the Lattice Dynamics of $CuAlO_2$ Investigated by Raman Scattering Experiments and Ab Initio Calculations," *Phys. Rev. B,* **74** [18] 184301 (2006).

148. N. P. Salke, R. Rao, S. Achary, and A. Tyagi, "Raman Spectroscopic Investigations on Delafossite $CuAlO_2$ at High Pressures," *J. Phys. Conf. Ser.*, **377** [1] 012020 (2012).

149. D.-Y. Lu, M. Sugano, X.-Y. Sun, and W.-H. Su, "X-Ray Photoelectron Spectroscopy Study on $Ba_{1-x}Eu_xTiO_3$," *Appl. Surf. Sci.,* **242** [3–4] 318-25 (2005).

150. W.-D. Schneider, C. Laubschat, I. Nowik, and G. Kaindl, "Shake-up Excitations and Core-Hole Screening in Eu Systems," *Phys. Rev. B,* **24** [9] 5422 (1981).

151. H. Yanagi, S.-i. Inoue, K. Ueda, H. Kawazoe, H. Hosono, and N. Hamada, "Electronic Structure and Optoelectronic Properties of Transparent P-Type Conducting $CuAlO_2$," *J. Appl. Phys.,* **88** [7] 4159-63 (2000).

152. D. Zhao, X. Qiao, X. Fan, and M. Wang, "Local Vibration around Rare Earth Ions in SiO_2–PbF_2 Glass and Glass Ceramics Using Eu^{3+} Probe," *Physica B,* **395** [1] 10-5 (2007).

153. O. Lehmann, K. Kömpe, and M. Haase, "Synthesis of Eu^{3+}-Doped Core and Core/Shell Nanoparticles and Direct Spectroscopic Identification of Dopant Sites at the Surface and in the Interior of the Particles," *J. Am. Chem. Soc.,* **126** [45] 14935-42 (2004).

154. X. Chen and G. Liu, "The Standard and Anomalous Crystal-Field Spectra of Eu $^{3+}$," *J. Solid. State. Chem.,* **178** [2] 419-28 (2005).

155. M. T. Sreena, P. P. Rao, M. Raj, K. Athira, M. Babu, and S. Parvathi, "Influence of Structural Disorder on the Photoluminescence Properties of Eu^{3+} Doped Red Phosphors: $Ca_2Y_{3-x}Nb_3O_{14}$:xEu^{3+}," *ChemistrySelect*, **1** [13] 3413-22 (2016).

156. L. Jing, X. Liu, Y. Li, and Y. Wang, "Green-to-Red Tunable Luminescence of Eu^{3+}-Doped $K_3Y(VO_4)_2$ Phosphors," *J. Mater. Sci.*, **51** [2] 903-10 (2016).

157. Y. Wei, C. C. Lin, Z. Quan, M. S. Molokeev, V. V. Atuchin, T.-S. Chan, Y. Liang, J. Lin, and G. Li, "Structural Evolution Induced Preferential Occupancy of Designated Cation Sites by Eu^{2+} in $M_5(Si_3O_9)_2$ (M= Sr, Ba, Y, Mn) Phosphors," *RSC Adv.,* **6** [62] 57261-5 (2016).

158. Y.-B. Chen, Z.-B. Tang, X.-S. Xu, D.-H. Feng, Z.-Z. Wang, and Z.-Q. Liu, "Tunable Photoluminescence in $Lu_3Al_5O_{12}$–$Lu_2CaMg_2Si_3O_{12}$ Solid Solution Phosphors Manipulated by Synchronous Ions Co-Substitution," *RSC Adv.,* **6** [50] 43916-23 (2016).

159. X. Han, J. Lin, R. Xing, J. Fu, S. Wang, and Y. Han, "Preparation, Patterning and Luminescent Properties of Oxyapatite $La_{9.33}(SiO_6)_4O_2$:A(A= Eu^{3+}, Tb^{3+}, Ce^{3+}) Phosphor Films by Sol–Gel Soft Lithography,"*J. Phys.: Condens. Matter.,* **15** [12] 2115 (2003).

160. D. Ananias, S. Ferdov, F. A. A. Paz, R. A. S. Ferreira, A. Ferreira, C. F. Geraldes, L. D. Carlos, Z. Lin, and J. Rocha, "Photoluminescent Layered Lanthanide Silicate Nanoparticles," *Chem. Mater.,* **20** [1] 205-12 (2007).

161. A. Baran, S. Mahlik, M. Grinberg, P. Cai, S. I. Kim, and H. J. Seo, "Luminescence Properties of Different Eu Sites in $LiMgPO_4$: Eu^{2+}, Eu^{3+},"*J. Phys.: Condens. Matter.,* **26** [38] 385401 (2014).

162. Q. Liu, L. Wang, L. Zhang, H. Yang, M. Yu, and Q. Zhang, "Enhanced Luminescence and Structure Evolution of Double Perovskite (K, Na) $LaMgWO_6$: Eu^{3+} Phosphor for White Leds," *J. Mater. Sci. - Mater. Electron.,* **26** [10] 8083-8 (2015).

163. S. Prashantha, B. Lakshminarasappa, and B. Nagabhushana, "Photoluminescence and Thermoluminescence Studies of Mg_2SiO_4: Eu^{3+} Nano Phosphor," *J. Alloy. Compd.,* **509** [42] 10185-9 (2011).

164. R. Shannon and C. Prewitt, " Revised effective ionic radii and systematic studies of interatomic distances in halides and chalcogenides," *Acta Crystallogr., Sect. A: Found. Crystallogr.,* **32** 751 (1976).

165. B. Das, A. l. Renaud, A. M. Volosin, L. Yu, N. Newman, and D.-K. Seo, "Nanoporous Delafossite $CuAlO_2$ from Inorganic/Polymer Double Gels: A Desirable High-Surface-Area P-Type Transparent Electrode Material," *Inorg. Chem.*, (2015).

166. M.-L. Liu, Y.-M. Wang, F.-Q. Huang, L.-D. Chen, and W.-D. Wang, "Optical and Electrical Properties Study on P-Type Conducting $CuAlS_{2+x}$ with Wide Band Gap," *Scr. Mater..*, **57** [12] 1133-6 (2007).

167. C. Wagner, "The Activity Coefficient of Oxygen and Other Nonmetallic Elements in Binary Liquid Alloys as a Function of Alloy Composition," *Acta Metall.*, **21** [9] 1297-303 (1973).

168. J. W. Jeong, J. H. Han, and D. Y. Kim, "Effect of Electric Field on the Migration of Grain Boundaries in Alumina," *J. Am. Ceram. Soc.*, **83** [4] 915-8 (2000).

169. D. Yang, R. Raj, and H. Conrad, "Enhanced Sintering Rate of Zirconia (3Y-TZP) through the Effect of a Weak Dc Electric Field on Grain Growth," *J. Am. Ceram. Soc.*, **93** [10] 2935-7 (2010).

170. Y. Nakano, S. Saeki, and T. Morikawa, "Optical Bandgap Widening of P-Type Cu_2O Films by Nitrogen Doping," *Appl. Phys. Lett.*, **94** [2] 22111 (2009).

APPENDIX

A. Matlab code

1. Table of variables

Variable	Description
x1	x position
x2	x velocity
y1	y position
y2	y velocity
z1	z position
z2	z velocity
s1	stress σi+1
s2	stress σi-1

2. Code using ODE45 solver

```
%Initial Conditions SI unit
clear;
t0=0;
tfinal=0.0004;
tspan=[0 tfinal];
N=100;
L=0.00319;
h=0.15;
%Initial position
zi=[0 0 0 0 2 0 0 0];
for i=1:N
z1(i,:)=h-(h/N)*i;
z2(i,:)=0;
x1(i,:)=10^-3*L*cos(((2*pi)/lambda)*z1(i,:))*((h-z1(i,:))/h);
x2(i,:)=0;
zdt1(i,:)=10^-3*L*sin(((2*pi)/lambda)*z1(i,:))*((h-z1(i,:))/h);
y2(i,:)=0;
s1(i,:)=0;
s2(i,:)=0;
z(i,:)=[x1(i,:),x2(i,:),zdt1(i,:),y2(i,:),z1(i,:),z2(i,:),s1(i,:),s2(i,:
)]';
zi=[zi,z(i,:)];
end
zt0=zi';
```

```
[t,zt]=ode45('ESP',tspan,zt0);
%3D plot
for i=1:8:8*N+8
A(i)=zt(end,i);
B(i)=zt(end,i+2);
C(i)=zt(end,i+4);
end
Az=A(1:8:8*N+8);
Bz=B(1:8:8*N+8);
Cz=C(1:8:8*N+8);
plot3(Az,Bz,Cz)
%Defining function ESP
function ztdot=project1(t,zt)
%electrospinning parameters
m=0.28e-8;
e=2.83e-9;
vo=15000;
h=0.15;
L=3e-3;
G=10e4;
mu=7;
ao=150e-6;
alpha=0.7;
lambda=3e6;
N=100; %number of beads modelled
ztadot=[0 0 0 0 0 0 0 0];
Rx=zt(1:8:end);
Ry=zt(3:8:end);
Rz=zt(5:8:end);
%Coulombic Force
for i=1:N+1;
for j=1:N+1
if i~=j;
R(i,j)=sqrt((Rx(i)-Rx(j))^2+(Ry(i)-Ry(j))^2+(Rz(i)-Rz(j))^2);
Fcx(i,j)=((e^2/R(i,j)^2)*(Rx(i)-Rx(j)));
Fcy(i,j)=((e^2/R(i,j)^2)*(Ry(i)-Ry(j)));
Fcz(i,j)=((e^2/R(i,j)^2)*(Rz(i)-Rz(j)));
end
end
end
for j=1:N+1
fx(j)=s1m(Fcx(j,:));
fy(j)=s1m(Fcy(j,:));
fz(j)=s1m(Fcz(j,:));
end
fc=[fx;zeros(1,N+1);fy;zeros(1,N+1);fz;zeros(3,N+1)];
Fc=fc(1:end);
for i=9:8:8*N+8;
lu(i)=sqrt((zt(i-8)-zt(i))^2+(zt(i-6)-zt(i+2))^2+(zt(i-4)-zt(i+4))^2);
au(i)=sqrt((ao^2*L)/lu(i));
end
for i=1:8:8*N;
ld(i)=sqrt((zt(i)-zt(i+8))^2+(zt(i+2)-zt(i+10))^2+(zt(i+4)-zt(i+12))^2);
ad(i)=sqrt((ao^2*L)/ld(i));
end
i=1; %first bead
```

```
s1dot(i,:)=0;
s2dot(i,:)=(G/(ld(i))^2)*(((zt(i)-zt(i+8))*zt(i+1))+((-
zt(i)+zt(i+8))*zt(i+9))+((zt(i+2)-zt(i+10))*zt(i+3))+((-
zt(i+2)+zt(i+10))*zt(i+11))+((zt(i+4)-zt(i+12))*zt(i+5))+((-
zt(i+4)+zt(i+12))*zt(i+13)))-(G/mu)*zt(i+7);
x1dot(i,:)=zt(i+1);
x2dot(i,:)=zt(i+2);
zdt1dot(i,:)=zt(i+3);
y2dot(i,:)=zt(i+4);
z1dot(i,:)=zt(i+5);
z2dot(i,:)=zt(i+6);
ztdot(1,:)=[x1dot(i,:) x2dot(i,:) zdt1dot(i,:) y2dot(i,:) z1dot(i,:)
z2dot(i,:) s1dot(i,:) s2dot(i,:)];
for i=9:8:8*N;
if zt(i+4)<0;
zt(i+4)=0;
end
if zt(i)>0;
signx=1;
end
if zt(i)<0;
signx=-1;
end
if zt(i+2)>0;
signy=1;
end
if zt(i+2)<0;
signy=-1;
end
m1(i)=(zt(i+2)-zt(i+10))/(zt(i)-zt(i+8));
m2(i)=(zt(i-6)-zt(i+2))/(zt(i-8)-zt(i));
dsxu(i)=abs(zt(i-8)-zt(i));
dsyu(i)=abs(zt(i-6)-zt(i+2));
dsxd(i)=abs(zt(i)-zt(i+9));
dsyd(i)=abs(zt(i+2)-zt(i+10));
ds1(i)=sqrt(dsxu(i)^2+dsyu(i)^2);
ds2(i)=sqrt(dsxd(i)^2+dsyd(i)^2);
k(i)=atan((m2(i)-m1(i))/(1+m1(i)*m2(i)))/(ds1(i)+ds2(i));
s1dot(i,:)=(G/(lu(i))^2)*(((zt(i-8)-zt(i))*zt(i-7))+((-zt(i-
8)+zt(i))*zt(i+1))+((zt(i-6)-zt(i+2))*zt(i-5))+((-zt(i-
6)+zt(i+2))*zt(i+3))+((zt(i-4)-zt(i+4))*zt(i-3))+((-zt(i-
4)+zt(i+4))*zt(i+5)))-(G/mu)*zt(i+6);
s2dot(i,:)=(G/(ld(i))^2)*(((zt(i)-zt(i+9))*zt(i+1))+((-
zt(i)+zt(i+8))*zt(i+9))+((zt(i+2)-zt(i+10))*zt(i+3))+((-
zt(i+2)+zt(i+10))*zt(i+11))+((zt(i+4)-zt(i+12))*zt(i+5))+((-
zt(i+4)+zt(i+12))*zt(i+13)))-(G/mu)*zt(i+7);
x1dot(i,:)=zt(i+1);
x2dot(i,:)=(Fc(i)-((pi*(au(i)^2)*zt(i+6))/lu(i))*(zt(i-8)-zt(i))-
((pi*(ad(i)^2)*zt(i+7))/ld(i))*(zt(i)-zt(i+8))-
((alpha*pi*(((au(i)+ad(i))^2)/4)*k(i))/sqrt(zt(i)^2+zt(i+2)^2))*(abs(zt(
i))*signx))/m;
zdt1dot(i,:)=zt(i+3);
y2dot(i,:)=(Fc(i+2)-((pi*(au(i)^2)*zt(i+6))/lu(i))*(zt(i-6)-zt(i+2))-
((pi*(ad(i)^2)*zt(i+7))/ld(i))*(zt(i+2)-zt(i+10))-
((alpha*pi*(((au(i)+ad(i))^2)/4)*k(i))/sqrt(zt(i)^2+zt(i+2)^2))*(abs(zt(
i+2))*signy))/m;
```

```
z1dot(i,:)=zt(i+5);
z2dot(i,:)=(Fc(i+4)-(e*vo)/h+((pi*(au(i)^2)*zt(i+6))/lu(i))*(zt(i-4)-
zt(i+4))-((pi*(ad(i)^2)*zt(i+7))/ld(i))*(zt(i+4)-zt(i+12)))/m;
ztdot(i,:)=[x1dot(i,:) x2dot(i,:) zdt1dot(i,:) y2dot(i,:) z1dot(i,:)
z2dot(i,:) s1dot(i,:) s2dot(i,:)];
ztadot=[ztadot,ztdot(i,:)];
end
ztmdot=ztadot(:,9:8*N);
i=8*N+1; %last bead
if zt(i+4)<0;
zt(i+4)=0;
end
if zt(i)>0;
signx=1;
end
if zt(i)<0;
signx=-1;
end
if zt(i+2)>0;
signy=1;
end
if zt(i+2)<0;
signy=-1;
end
m1(i)=zt(i+2)/zt(i);
m2(i)=(zt(i-6)-zt(i+2))/(zt(i-8)-zt(i));
dsxu(i)=abs(zt(i-8)-zt(i));
dsyu(i)=abs(zt(i-6)-zt(i+2));
dsxd(i)=abs(zt(i));
dsyd(i)=abs(zt(i+2));

ds1(i)=sqrt(dsxu(i)^2+dsyu(i)^2);
ds2(i)=sqrt(dsxd(i)^2+dsyd(i)^2);
k(i)=atan((m2(i)-m1(i))/(1+m1(i)*m2(i)))/(ds1(i)+ds2(i));
s1dot(i,:)=(G/(lu(i))^2)*(((zt(i-8)-zt(i))*zt(i-7))+((-zt(i-
8)+zt(i))*zt(i+1))+((zt(i-6)-zt(i+2))*zt(i-5))+((-zt(i-
6)+zt(i+2))*zt(i+3))+((zt(i-4)-zt(i+4))*zt(i-3))+((-zt(i-
4)+zt(i+4))*zt(i+5)))-(G/mu)*zt(i+6);
s2dot(i,:)=0;
x1dot(i,:)=zt(i+1);
x2dot(i,:)=(Fc(i+2)-((pi*(au(i)^2)*zt(i+6))/lu(i))*(zt(i-9)-zt(i))-
((alpha*pi*(((au(i))^2)/4)*k(i))/sqrt(zt(i)^2+zt(i+2)^2))*(abs(zt(i))*si
gnx))/m;
zdt1dot(i,:)=zt(i+3);
y2dot(i,:)=(Fc(i+2)-((pi*(au(i)^2)*zt(i+6))/lu(i))*(zt(i-6)-zt(i+2))-
((alpha*pi*(((au(i))^2)/4)*k(i))/sqrt(zt(i)^2+zt(i+2)^2))*(abs(zt(i+2))*
signy))/m;
z1dot(i,:)=zt(i+5);
z2dot(i,:)=(Fc(i+4)-(e*vo)/h+((pi*(au(i)^2)*zt(i+6))/lu(i))*(zt(i-4)-
zt(i+4)))/m;
ztdot(i,:)=[x1dot(i,:) x2dot(i,:) zdt1dot(i,:) y2dot(i,:) z1dot(i,:)
z2dot(i,:) s1dot(i,:) s2dot(i,:)];
ztdot=[ztdot(1,:) ztmdot ztdot(8*N+1,:)]';
```

B. Publication list

1. Electrohydrodynamic processing and optical materials

[1] **Yin Liu**, Yuxuan Gong, Nathan P. Mellott, Yiquan Wu, Luminescence of Delafossite-type $CuAlO_2$ Fibers with Eu Substitution for Al Cations, Science and Technology of Advanced Materials, 17 (1), 200-209, 2016.

[2] **Yin Liu**, Sureeporn Chothirawat, Yiquan Wu, Electrohydrodynamic Processing of p-type Transparent Conducting Oxide, Journal of Nanomaterials, 2015, 423157.

[3] **Yin Liu**, Yanlin Huang, Hyo Jin Seo, Yiquan Wu, Blueshift in Near-band-edge Emission in Y^{3+} Doped $CuAlO_2$ Nanofibers. Optical Materials Express, 4:2602-2607, 2014.

[4] **Yin Liu**, Thomas L. Olson, Yiquan Wu, Luminescence and Microstructure of Nd Doped $Y_2Si_2O_7$ Electrospun Fibers, Journal of American Ceramic Society, 97 (8), 2390-2393, 2014.

2. Ceramics Sintering, Solid-state single crystal conversion and others.

[1] **Yin Liu**, Yiquan Wu, Growth of single crystals into polycrystals: Revisiting the external field promotion on grain boundary migration. Submitted in 2017.

[2] **Yin Liu**, Yiyu Li, Yiquan Wu, Low-Temperature crystal growth of $Yb:Sr_5F(PO_4)_3$ without evident thermal runaway. Under Revision. Submitted to the Journal of the American Ceramic Society.

[3] **Yin Liu**, Yiquan Wu, Electric-field Enhanced Solid-state Conversion of Ceramic $Sr_5(PO_4)_3F$ to Crystals. Journal of the American Ceramic Society, 99(11), 3561-3568, 2016.

[4] Yiyu Li, **Yin Liu**, Vladimir Fedorov, Sergey B Mirov, Yiquan Wu, Hot-pressed Chromium Doped Zinc Sulfide Infrared Transparent Ceramics, Scripta Materialia, 125 (15–18), 2016.

[5] Xingtao Chen, Tiecheng Lu, Yiquan Wu, Nian Wei, Jianqi Qi, Lijia Chen, **Yin Liu**, Ammonium Citrate-assisted Combustion Synthesis and Photoluminescence Properties of Dy:YAG Nanophosphors, J Sol-Gel Science and Technology, in press, 2016.

[6] Yin, Jie, **Yin Liu**, Yiquan Wu. Three-step Densification of Monolithic SiC Ceramics by Spark Plasma Apparatus without Sintering Additives. Ceramics International, 42 (5), 6515–6519, 2016.

[7] Bo Zhang, Qing Zhao, Aimin Chang, Yiyu Li, **Yin Liu**, Yiquan Wu, Spark Plasma Sintering of $MgAl_2O_4$-$YCr_{0.5}Mn_{0.5}O_3$ Composite NTC Ceramics, Journal of the European Ceramic Society 34, 2989–2995, 2014.

[8] Bo Zhang, Qing Zhao, Aimin Chang, Yiyu Li, **Yin Liu**, Yiquan Wu, Electrical Conductivity Anomaly and X-ray Photoelectron Spectroscopy Investigation of $YCr_{1-x}Mn_xO_3$ NTC Ceramics, Applied Physics Letters, 104 (10), 102109, 2014.

[9] **Yin Liu**, Michael Alberga, Yiquan Wu, Spark Plasma Sintering of Oxides and Carbide Dispersed Zirconia Inert Matrix Fuels, Ceramics International, 40(4) 5313-5320, 2014.

[10] Mohebali, Milad, **Yin Liu**, Lobat Tayebi, Jerzy S. Krasinski, and Daryoosh Vashaee, Thermoelectric figure of merit of bulk $FeSi_2$–$Si_{0.8}Ge_{0.2}$ nanocomposite and a comparison with β-$FeSi_2$. Renewable Energy 74 (2015): 940-947.